

Materials Testing for Heatshield Applications during CubeSat

## Re-entry with Passive Demise

Claudio Vestini, Fizza Naqvi, Hani Moussa, Alex Berresford

April 21, 2025

## Contents

<b>1 Abstract</b>	<b>5</b>
<b>2 Introduction</b>	<b>5</b>
<b>3 Launch Provider</b>	<b>5</b>
<b>4 Trajectory</b>	<b>6</b>
4.1 Overview - Fizza Naqvi . . . . .	6
4.2 De-Orbit Burn for Controlled Re-entry - Fizza Naqvi . . . . .	7
4.3 Orbital Dynamics - Fizza Naqvi . . . . .	9
4.4 Atmospheric Model - Fizza Naqvi . . . . .	10
4.5 MATLAB Trajectory Model - Fizza Naqvi . . . . .	13
4.5.1 Input Parameters . . . . .	13
4.5.2 Simulation Process . . . . .	13
4.5.3 Outputs of the Simulation . . . . .	13
4.6 Results - Fizza Naqvi . . . . .	15
4.7 Verification - Fizza Naqvi . . . . .	16
4.8 Collision Analysis - Fizza Naqvi . . . . .	18
<b>5 Mechanical and Structural Design</b>	<b>21</b>
<b>6 Electronics - Hani Moussa</b>	<b>22</b>
6.1 Interfacing and Communications . . . . .	22
6.1.1 Data System Architecture . . . . .	22
6.1.2 OBC and Data Processing . . . . .	22
6.1.3 Communication Protocol . . . . .	24
6.1.4 Telemetry Strategy . . . . .	24
6.1.5 Link Budget . . . . .	32
6.1.6 Data Rate . . . . .	37
6.2 Electrical Systems and Power . . . . .	38
6.2.1 Orbital Shut-off Period . . . . .	38
6.2.2 Operation Power Budget . . . . .	40
6.2.3 Power Distribution and System Design . . . . .	41
<b>7 Instrumentation</b>	<b>42</b>
7.1 Ablation Sensing - Hani Moussa . . . . .	42
7.1.1 Temperature . . . . .	42
7.1.2 Pressure . . . . .	44

7.1.3	Recession . . . . .	45
7.2	Cold Gas Thrusters - Fizza Naqvi . . . . .	49
7.3	Altitude Tracking via Sensor Fusion - Fizza Naqvi . . . . .	49
7.3.1	Overview . . . . .	49
7.3.2	System Dynamics . . . . .	51
7.3.3	Instrumentation Models . . . . .	52
7.3.4	Kalman Filter . . . . .	53
7.3.5	Altitude Estimation . . . . .	54
7.4	Attitude Control System - Claudio Vestini . . . . .	55
7.5	Optical Spectroscopy Hardware - Fizza Naqvi . . . . .	55
7.5.1	Spectrometer . . . . .	55
7.5.2	Fibre Optic Cable . . . . .	56
7.5.3	Cosine Corrector . . . . .	56
7.6	Atmospheric Composition Analysis - Fizza Naqvi . . . . .	57
7.6.1	Overview . . . . .	57
7.6.2	Pre-flight calibration . . . . .	57
7.6.3	Post-mission data analysis . . . . .	58
7.6.4	Assumptions . . . . .	60
<b>8</b>	<b>Aerothermal Environment</b>	<b>61</b>
8.1	Introduction - Claudio Vestini . . . . .	61
8.2	Orbital Phase - Claudio Vestini . . . . .	62
8.2.1	Heat Equation and Geometry . . . . .	62
8.2.2	Flight Configuration and Assumptions . . . . .	62
8.2.3	Boundary Conditions . . . . .	65
8.2.4	IHCP Solver . . . . .	65
8.3	Re-Entry Phase - Claudio Vestini . . . . .	67
8.3.1	The Challenge of Hypersonic Flows - Claudio Vestini . . . . .	67
8.3.2	Flow Distributions for CubeSats - Claudio Vestini . . . . .	69
8.3.3	CFD Simulations - Claudio Vestini . . . . .	69
8.3.4	ANSYS Fluent Solver - Claudio Vestini . . . . .	71
8.3.5	Simulation Parameters - Claudio Vestini . . . . .	71
8.3.6	Adaptive Mesh Refinement - Claudio Vestini . . . . .	73
8.3.7	Wall Treatment - Claudio Vestini . . . . .	73
8.3.8	Boundary Conditions - Claudio Vestini . . . . .	74
8.3.9	Mesh - Claudio Vestini . . . . .	76
8.3.10	Results - Claudio Vestini . . . . .	77

8.4 Thermite for Demise (T4D) - Claudio Vestini . . . . .	81
<b>9 Costs</b>	<b>84</b>
<b>10 Project Risks</b>	<b>84</b>
<b>11 Conclusion</b>	<b>84</b>

**1 Abstract****2 Introduction****3 Launch Provider**

## 4 Trajectory

### 4.1 Overview - Fizza Naqvi

The satellite's mission begins with its launch into a circular Low Earth Orbit (LEO) at 400km, chosen for its advantages in terms of orbital dynamics and mission costs. LEO provides a natural environment for rapid orbital decay due to atmospheric drag, making it an ideal choice for missions involving controlled re-entry. The proximity of LEO to Earth's surface ensures a shorter orbital lifetime, which reduces the time and energy required to bring the CubeSat to the desired re-entry altitude for testing purposes. In addition, the cost of launching into LEO is lower compared to other orbital regimes, due to the reduced energy required for launch and the greater availability of launch vehicles capable of reaching these altitudes. Furthermore, LEO is less congested than higher altitudes, such as above 500 km, where spatial density increases and the risk of collision with other objects is greater.

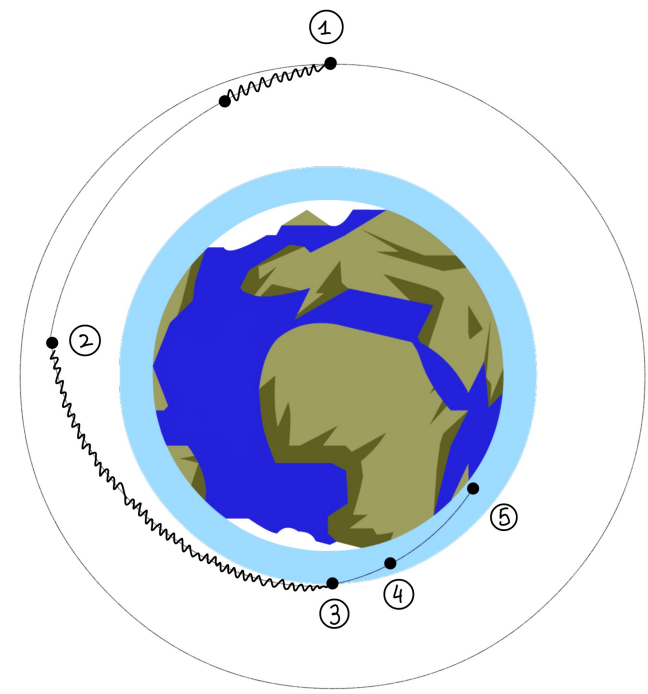


Figure 1: Trajectory Overview.

To facilitate re-entry, the satellite will perform a de-orbit burn maneuver, where the CubeSat's propulsion system will be used to slow it down, reducing its altitude and initiating atmospheric re-entry. This controlled de-orbit burn accelerates the satellite's descent, ensuring a faster re-entry timeline. Moreover, during the mission, reaction wheels will be employed to spin up the satellite, using Model Predictive Control (MPC) to maintain the desired spin rate. This spinning mechanism helps to evenly distribute heat across the satellite's surface during re-entry, promoting uniform heating to limit structural failure and allow for more accurate measurements for materials testing.

As the CubeSat descends through the atmosphere, it will undergo thermite breakup at an altitude of approximately 40 km. This ensures that the satellite burns up completely, leaving minimal debris and significantly

reducing the risk of reaching the Earth's surface.

While Low Earth Orbit (LEO) offers advantages like reduced launch costs and shorter re-entry times, it also introduces orbital perturbations that can influence the satellite's trajectory. However, this analysis assumes a two-body problem and neglects these perturbations due to the short mission duration. Effects such as Earth's oblateness (which causes the J2 effect), solar radiation pressure, and third-body gravitational influences from the Moon and Sun are considered negligible. Although the J2 effect can be significant in low orbits, it is assumed to have a minimal impact on the orbital decay rate over the short timescale considered [1]. Likewise, atmospheric winds and other small forces are not included in the model.

## 4.2 De-Orbit Burn for Controlled Re-entry - Fizza Naqvi

To ensure the CubeSat's controlled re-entry, a retrograde impulse burn is performed using cold gas thrusters, detailed in section 7.2. These thrusters play a critical role in performing the de-orbit burn, which is vital for the CubeSat's descent. The burn works in conjunction with the Model Predictive Control (MPC) system for attitude control, discussed in Section 7.4, ensuring that the CubeSat's attitude is maintained throughout the process. Proper attitude control is crucial to prevent misalignment during the burn, which could otherwise destabilise the descent and increase the risk of mission failure.

Without the de-orbit burn, the CubeSat would rely solely on atmospheric drag to gradually lower its altitude. At 400 km, drag is relatively weak, so orbital decay is slow, and it could take several months to reach the denser atmosphere needed for rapid re-entry. However, by performing the burn, the satellite transitions to an elliptical orbit with a perigee of 140 km. Instead of slowly spiralling down through multiple circular orbits, the CubeSat now descends directly to a region of high drag, dramatically accelerating the re-entry process.

The burn is modelled as an impulsive manoeuvre, occurring over a very short duration. As a result, the CubeSat's altitude during the burn remains nearly constant. The total burn time for the three MiPS (Micro Propulsion System) thrusters to achieve the required delta-v is 399 seconds, calculated using equation 1 [2]. This brief thrust period introduces only a minor altitude change, which is considered negligible in the MATLAB trajectory model (section 4.5). However, this small reduction in velocity translates into a change in the shape of the orbit, lowering the perigee to 140 km. At this altitude, the atmospheric density is high enough to induce rapid orbital decay, leading to re-entry within a much shorter timescale compared to passive drag-induced decay from 400 km.

$$T_b = \frac{m_{\text{propellant}}}{\dot{m}} = \frac{m_{\text{propellant}} \cdot I_{sp} \cdot g_0}{F_{\text{total}}} \quad (1)$$

where  $I_{sp}$  is the specific impulse in seconds,  $g_0$  represents the standard gravitational acceleration, taken as  $9.8 \text{ m/s}^2$ , and  $F_{\text{total}}$  is the total thrust produced by the thrusters.

The selection of 140 km as the perigee altitude reflects a deliberate balance between achieving timely re-entry

and preserving sufficient time for experimentation during descent, as outlined in Table 1. At this altitude, the satellite begins encountering significant atmospheric drag, which initiates a rapid but not immediate descent. This allows it to spend more time within the critical altitude range (approximately 150–40 km) where materials testing and data collection can be conducted effectively.

Perigee Altitude	Re-entry Behaviour	Impact on Experimentation
120–130 km	Very rapid descent due to strong atmospheric drag; altitude drops sharply in a short time.	Minimal time for data collection; limited opportunity for meaningful experimentation before burn-up.
140–150 km	Moderate descent rate with significant drag effects; more time spent in denser atmospheric layers.	Allows more detailed materials testing and environmental data collection before major deceleration.
Above 150 km	Slower descent through thinner atmosphere; prolonged orbital decay phase.	Extended testing window, but increased risk of incomplete burn-up, which may affect experimental outcomes.

Table 1: Trade-offs of Different Perigee Altitudes for CubeSat Re-entry

For the de-orbit burn to be effective, it must be executed precisely at the correct orbital position and with perfect alignment. The thrusters must fire exactly opposite to the satellite's velocity vector (retrograde direction) to ensure that the reduction in velocity translates purely into a decrease in perigee, rather than introducing unwanted inclination changes or perturbations. Any misalignment could result in an inefficient burn, an incorrect perigee altitude, or an unstable trajectory, potentially compromising the mission objectives.

To mitigate these risks, the CubeSat's MPC system ensures proper attitude control during the burn. Before firing the thrusters, the satellite undergoes a precise orientation maneuver to align itself with the desired retrograde direction. Real-time feedback from onboard sensors is used to verify and correct alignment errors before ignition.

The initial orbit is circular, therefore the velocity before the burn is determined by the orbital velocity equation:

$$v_{\text{initial}} = \sqrt{\frac{\mu}{r_{\text{orbit}}}} = 7.67 \text{ km/s} \quad (2)$$

Where  $\mu$  is the gravitational parameter for Earth ( $3.986 \times 10^5 \text{ km}^3/\text{s}^2$ ) and  $r_{\text{orbit}}$  is the orbital radius at 400 km altitude ( $r_{\text{orbit}} = 6778 \text{ km}$ ).

After the deorbit burn, the semi-major axis [3] of this orbit is calculated as:

$$a = \frac{r_{\text{orbit}} + r_{\text{perigee}}}{2} = 6648 \text{ km} \quad (3)$$

where  $r_{\text{perigee}} = 6518 \text{ km}$ .

Using this value, the final velocity at the apogee of the elliptical orbit is calculated to be:

$$v_{\text{final}} = \sqrt{\mu \left( \frac{2}{r_{\text{orbit}}} - \frac{1}{a} \right)} = 7.59 \text{ km/s} \quad (4)$$

The required delta-V for the deorbit burn is:

$$\Delta v = v_{\text{initial}} - v_{\text{final}} = 0.0767 \text{ km/s} \quad (5)$$

Thus, the CubeSat requires a delta-V of approximately 77 m/s to execute the deorbit burn and lower its perigee to 140 km. This maneuver places the satellite in an orbital regime where atmospheric drag increases significantly, leading to a rapid decrease in altitude and accelerating the re-entry process. This delta-V is within practical limits for the propulsion system selected for our CubeSat, detailed in section 7.2, and ensures a controlled descent into the denser layers of the atmosphere.

### 4.3 Orbital Dynamics - Fizza Naqvi

Simulating the trajectory of the CubeSat involves understanding how its altitude changes over time, while accounting for the influence of atmospheric drag. An equation for the rate of change in altitude is derived by considering the total mechanical energy of the satellite in orbit [4].

The total mechanical energy of a satellite in orbit is the sum of its gravitational potential energy and kinetic energy:

$$E = -\frac{\mu m}{r} + \frac{1}{2}mv^2. \quad (6)$$

The velocity for the orbit, after the de-orbit burn, is given by:

$$v = \sqrt{\mu \left( \frac{2}{r} - \frac{1}{a} \right)} \quad (7)$$

The eccentricity of an orbit is given by:

$$e = \frac{r_{\text{apogee}} - r_{\text{perigee}}}{r_{\text{apogee}} + r_{\text{perigee}}} \quad (8)$$

Equation 8 can be used to calculate the instantaneous radial distance in an elliptical orbit:

$$r = \frac{a(1 - e^2)}{1 + e \cos \theta} \quad (9)$$

The eccentricity for our target trajectory, calculated using equation 8, is very small ( $< 0.1$ ). Therefore, for simplicity in the simulation, equation 9 can be approximated as  $r \approx a$ .

After substituting equation 7 with the approximation into equation 9, we obtain:

$$E = -\frac{\mu m}{2r}. \quad (10)$$

In an LEO, atmospheric drag must be considered, as it leads to a continuous loss of mechanical energy over time, which results in a gradual decrease in altitude. The dissipated power due to drag can be expressed as:

$$P = \mathbf{F}_D \cdot \mathbf{v}, \quad (11)$$

where  $\mathbf{F}_D$  is the drag force acting on the satellite. Using equation 10, the time derivative of the satellite's mechanical energy can thus be written as:

$$\frac{d}{dt} \left( -\frac{\mu m}{2r} \right) = \mathbf{F}_D \cdot \mathbf{v}. \quad (12)$$

The drag force acting on a body with drag coefficient  $C_D$  and reference area A moving at a velocity v through an atmosphere of density  $\rho$  is:

$$F_D = \frac{1}{2} \rho C_D A v^2, \quad (13)$$

Substituting equation 13 into equation 12 gives the result:

$$\frac{\mu m}{2} \frac{\dot{r}}{r^2} = -\frac{1}{2} \rho(r) C_D A \left( \frac{\mu}{r} \right)^{\frac{3}{2}} \quad (14)$$

which simplifies to:

$$\dot{r} = -k \sqrt{r} \rho(r) \quad (15)$$

where:

$$k = \frac{C_D A \sqrt{\mu}}{m} \quad (16)$$

#### 4.4 Atmospheric Model - Fizza Naqvi

The atmospheric density model used in this study accounts for the influence of solar activity on the thermosphere and ionosphere, which significantly impacts the environmental conditions experienced by the CubeSat during re-entry. Solar radiation is a key factor in determining atmospheric density, as it interacts with atmospheric

particles, ionising them and increasing their energy. This leads to an expansion of the thermosphere, resulting in variations in density depending on the solar cycle.

The solar cycle follows an 11-year periodic variation in solar activity, with solar maximums characterised by heightened radiation, increased thermospheric temperature, and subsequent expansion. As a result, atmospheric density decreases at higher altitudes, reducing the drag force experienced by the satellite. However, despite the lower density, the increased temperature and energy of atmospheric particles lead to higher momentum transfer, effectively increasing drag. Conversely, during solar minimums, solar radiation is weaker, causing thermospheric contraction and an increase in atmospheric density, which leads to lower overall drag and a slower orbital decay rate. These fluctuations can have a significant impact on satellite orbits and re-entry trajectories.

To account for these effects, the model incorporates solar flux ( $F_{10.7}$ ) and geomagnetic activity ( $A_P$ ) indices. The solar flux at a 10.7 cm wavelength is a widely used proxy for total solar X-ray flux, which strongly influences atmospheric density. The expected value for the planned launch period in December 2026 is 125 SFU, based on the solar cycle radio flux progression data determined by the Space Weather Prediction Center [5], as shown in Figure 2. The ( $A_P$ ) geomagnetic index quantifies geomagnetic disturbances caused by interactions between solar wind and Earth's magnetosphere, particularly through the interplanetary magnetic field (IMF). Unlike the  $F_{10.7}$  index, which follows a smooth solar cycle, the  $A_P$  index is highly variable due to its sensitivity to unpredictable solar events, such as coronal mass ejections or solar flares. However, outside of these solar events, the  $A_P$  index shows limited variation. For this study, a predicted, averaged  $A_P$  value of 10.8 for 2024 [6] is used, providing a reasonable estimate of geomagnetic activity during this period.

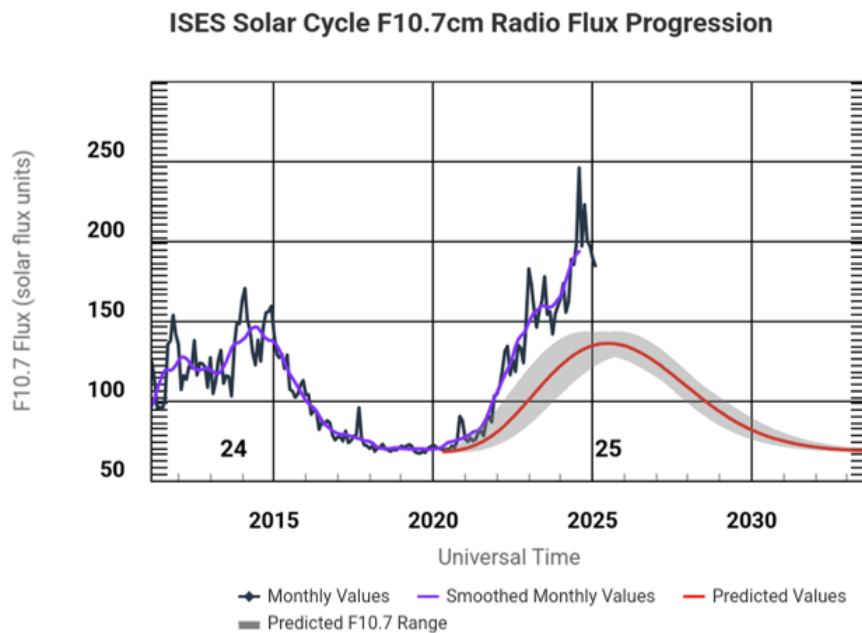


Figure 2: Solar cycle radio flux progression data determined by the Space Weather Prediction Center (SWPC) [5].

The primary atmospheric density model employed is the Australian Space Weather Agency (ASWA) model [7], which defines density using an exponential formulation with a variable scale height. The model equations are

as follows:

$$T = 900 + 2.5(F_{10.7} - 70) + 1.5Ap \quad (17)$$

$$m = 27 - 0.012(h - 200), \quad 180 < h < 500 \quad (18)$$

$$H = \frac{T}{m} \quad (19)$$

$$\rho = 6 \times 10^{-10} \exp\left(-\frac{h - 175}{H}\right) \quad (20)$$

where T is the temperature in Kelvin, m is the mass in kg, h is the altitude in km, H is the scale height<sup>1</sup> in km, and  $\rho$  is the atmospheric density with units kg/m<sup>3</sup>. This model is valid for altitudes between 180 km and 500 km. The ASWA model's molecular mass equation is not valid below 180km, as it does not correctly account for variations in atmospheric composition. Therefore, a piecewise model has been developed to ensure smooth transitions between different atmospheric layers while maintaining consistency in density predictions.

For altitudes below 180 km, the modified model utilises NASA's Earth Atmosphere Model [8] to incorporate temperature and mass variations in the stratosphere and troposphere. The equations are defined as:

For  $100 < h \leq 180$  km (lower stratosphere):

$$T = 216.69 \text{ K} \quad (21)$$

$$m = 28.96 - 0.0076 \cdot (h - 100) \quad (22)$$

$$\rho(h) = \rho_{180} \cdot \exp\left(-\frac{h - 180}{H}\right) \quad (23)$$

For  $h \leq 100$  km (troposphere):

$$T = 288.19 - 0.00649 \cdot h \quad (24)$$

$$m = 28.96 \quad (25)$$

$$\rho(h) = \rho_{100} \cdot \exp\left(-\frac{h - 100}{H}\right) \quad (26)$$

In these equations,  $\rho_{180}$  and  $\rho_{100}$  refer to the reference densities at 180 km and 100 km, respectively.

This piecewise approach ensures continuity between atmospheric layers and improves the accuracy of density estimations for the CubeSat's re-entry trajectory. While more complex models exist, the combined models from ASWA and NASA provide a practical balance between accuracy and computational efficiency: the piecewise model provides sufficient accuracy for the scope of the simulation, while being computationally less demanding than higher-order models. This makes it a practical choice for the analysis, where computational efficiency is important for handling the extensive calculations involved in simulating the CubeSat's re-entry trajectory.

---

<sup>1</sup>The scale height represents the altitude over which the atmospheric density decreases by a factor of e.

## 4.5 MATLAB Trajectory Model - Fizza Naqvi

### 4.5.1 Input Parameters

The simulation requires several input parameters, which are crucial for calculating the satellite's motion during atmospheric re-entry. These parameters are as follows:

- Altitude ( $h = 400$  km): The initial altitude of the CubeSat above Earth's surface, positioned in Low Earth Orbit (LEO).
- Satellite Mass ( $m = 12$  kg): The mass of the CubeSat, which influences the deceleration rate during re-entry.
- Reference Area ( $A = 0.06 \times 10^{-6}$  km $^2$ ): The averaged surface area of the CubeSat exposed to drag forces. This is not equivalent to the cross-sectional area of the 8U CubeSat.
- Drag Coefficient ( $C_D = 2.2$ ): An approximate value for the dimensionless number representing the aerodynamic drag experienced by the CubeSat, based on typical values for similar small satellites [9].
- Solar Flux Index ( $F_{107} = 125$ ): An average value representing solar activity for December 2026.
- Geomagnetic Index ( $A_p = 10.8$ ): An average value representing geomagnetic activity over the course of a year.

These input parameters are fed into the simulation function, where they are used to model the CubeSat's trajectory based on equation 15.

### 4.5.2 Simulation Process

The flowchart in Figure 3 visually illustrates the algorithm used to simulate the satellite's re-entry. The general process is outlined as follows:

1. **Initialisation:** The function begins by initialising the required variables and arrays, including those for storing altitude and time. Additionally, constants such as the Earth's radius and gravitational constant are defined, ensuring consistency throughout the simulation.
2. **Iteration:** In each iteration, the algorithm calculates the atmospheric density at the satellite's current altitude, solves equation 15 using Runge-Kutta 4<sup>2</sup>, and updates the altitude and time.
3. **Termination:** The simulation continues until the satellite reaches an altitude of 40 km, where thermite breakup is expected to occur, at which point the re-entry process is considered complete.

### 4.5.3 Outputs of the Simulation

The outputs of the simulation allow the CubeSat's descent to be tracked:

---

<sup>2</sup>The Runge-Kutta 4th order (RK4) method [10] is a numerical integration technique commonly used to solve ordinary differential equations. It provides a good balance between accuracy and computational efficiency by evaluating the derivative at four points within each time step.

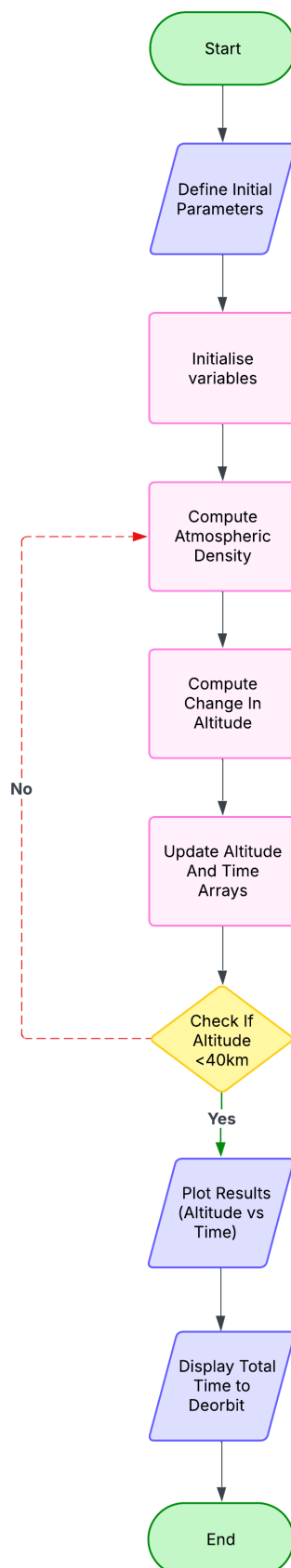


Figure 3: Algorithm flowchart for simulating the satellite re-entry trajectory.

- Altitude: This is an array containing the satellite's altitude (in kilometers) at each time step, showing the change in altitude as the satellite descends towards the Earth's surface.
- Time: This is an array containing the corresponding time (in hours) for each altitude step.

These outputs allow for detailed analysis of the satellite's re-entry profile, helping to understand its motion, and the effect of aerodynamic drag, solar flux, and geomagnetic activity on the descent. In addition to the numerical outputs, a plot of altitude versus time is generated, which provides a visual representation of the satellite's descent.

## 4.6 Results - Fizza Naqvi

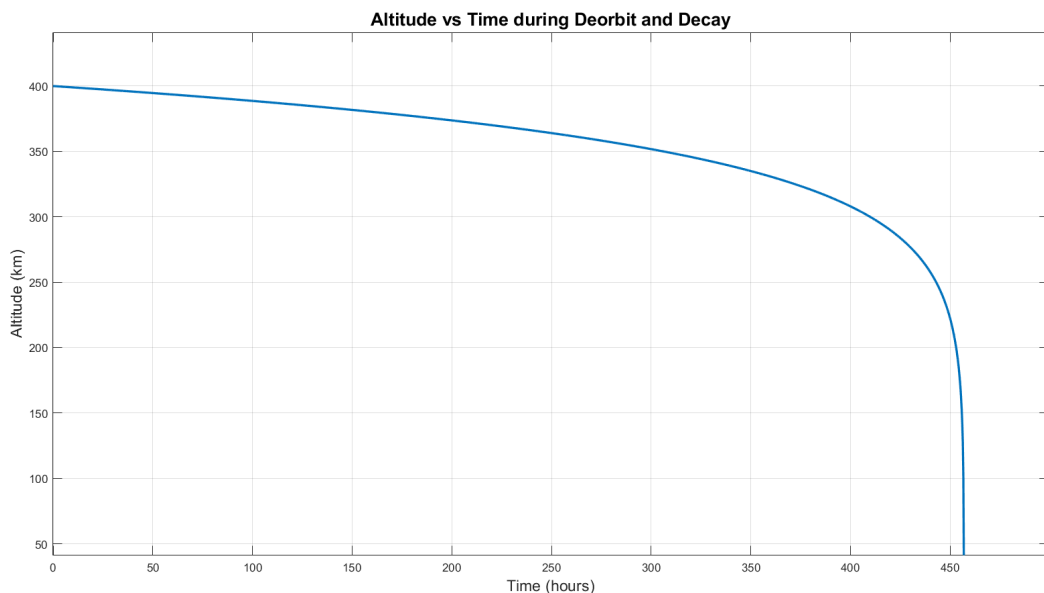


Figure 4: Altitude vs Time plot generated by the MATLAB trajectory simulation.

The simulation demonstrates the critical role of atmospheric drag in shaping the satellite's descent profile. At altitudes above approximately 250–300 km, the satellite undergoes a gradual decline due to the relatively thin atmosphere. As it descends into denser atmospheric layers below 250 km, the drag force increases substantially, resulting in a rapid decrease in altitude as drag becomes the dominant factor in orbital decay. This transition from gradual to steep descent is consistent with expectations from atmospheric drag models and is typical for satellites in low Earth orbit (LEO). To further illustrate this, the re-entry profile of ESA's ERS-2 satellite is shown in figure 5, demonstrating a similar observed descent pattern with a marked increase in decay rate after 250 km. This comparison confirms that the shape of the re-entry profile observed in the simulation aligns with established behaviour for re-entering satellites at these altitudes.

The simulation of the CubeSat's de-orbit trajectory predicts a total duration of 456.93 hours. This result provides insight into the timescale for re-entry, although the duration is highly dependent on several key parameters. One such parameter is  $F_{10.7}$ , which can exhibit significant variation throughout the year. While  $A_p$  is modelled as constant or averaged, the variability in  $F_{10.7}$  introduces a level of uncertainty in predicting the

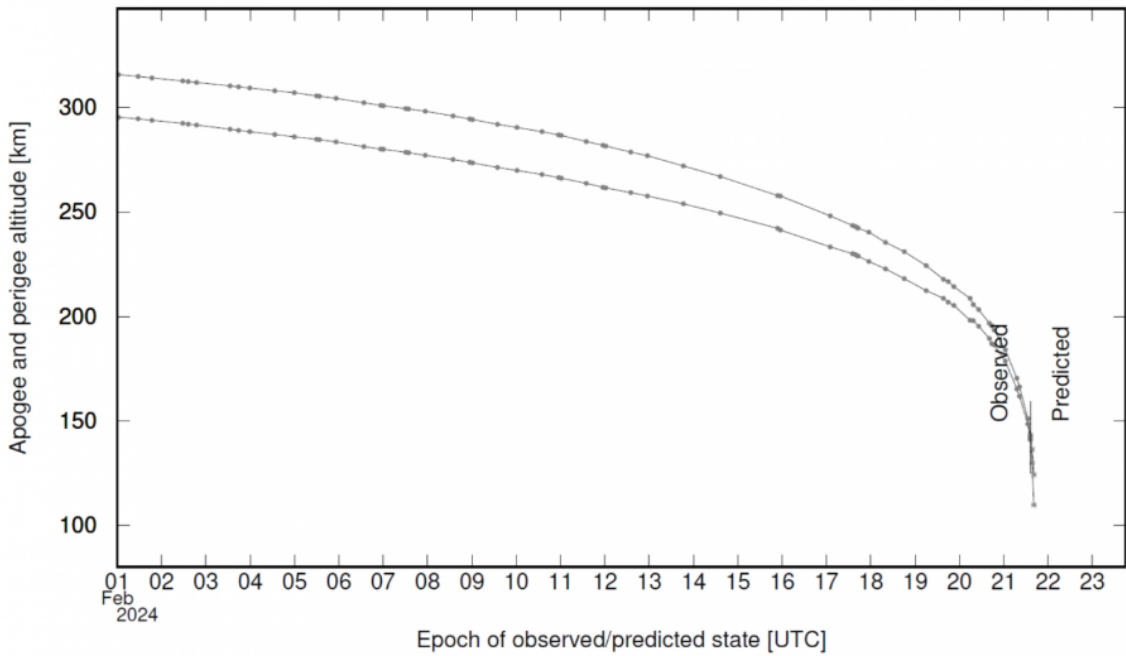


Figure 5: Re-entry profile of the ERS-2 satellite, showing high decay after 250 km [11].

exact de-orbit time. Therefore, the duration of the re-entry process can vary depending on the specific timing of the launch, as  $F_{10.7}$  fluctuates with solar activity.

The average value of  $F_{10.7}$  for December 2026 is forecasted to be 125, but the range of forecasted values for the month is  $116.3 \leq F_{10.7} \leq 134.8$ . Running the simulation for these values results in different de-orbit durations, as shown in Table 2:

Forecasted $F_{10.7}$	De-orbit Duration (hours)
116.3	500.26
125	456.93
134.8	414.59

Table 2: De-orbit duration for different forecasted  $F_{10.7}$  values.

This variation highlights the high sensitivity of the de-orbit duration to the solar flux index, with the predicted time varying by over 80 hours depending on the  $F_{10.7}$  value, suggesting that the re-entry duration could vary even more if a different month is chosen for the launch date.

#### 4.7 Verification - Fizza Naqvi

To verify the MATLAB trajectory model, a comparative simulation was conducted using NASA's General Mission Analysis Tool (GMAT) [12]. GMAT is an open-source, astrodynamics software widely used for mission design and trajectory analysis. It employs numerical integration techniques, including the Runge-Kutta 8(9) method, to propagate spacecraft motion under various force models, including atmospheric drag, gravity perturbations, and thrust events. By directly implementing the deorbit burn and subsequent atmospheric decay, GMAT provides a benchmark for assessing the accuracy of the MATLAB model. Comparing the results from MATLAB and GMAT allows for verification of the MATLAB model's accuracy and identification of any

discrepancies arising from differences in force modeling or numerical methods.

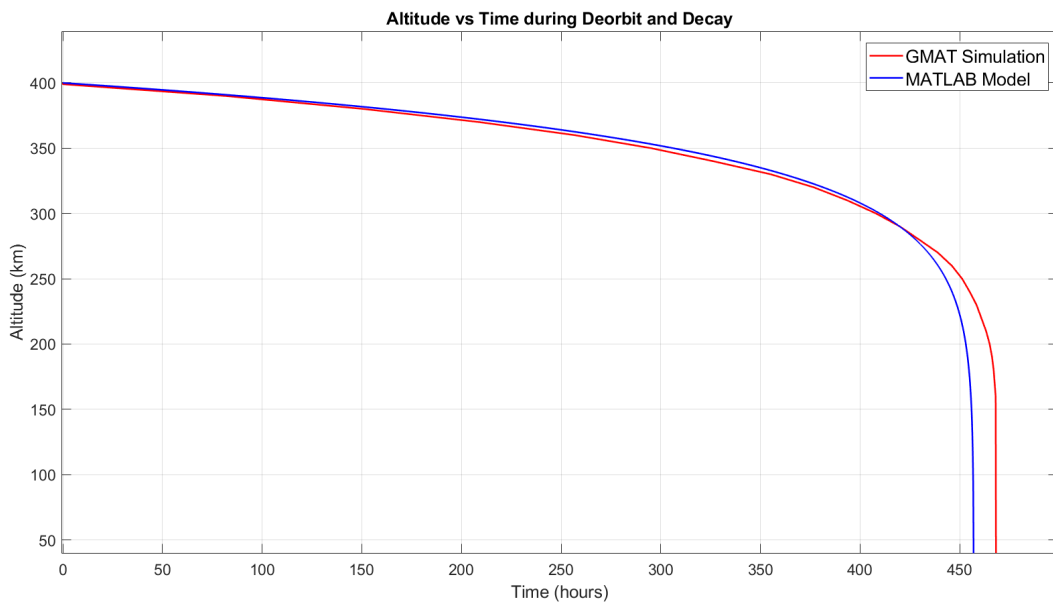


Figure 6: Comparison of MATLAB model and GMAT simulation.

As shown in Figure 6, the two predictions follow each other very closely, verifying the accuracy of the MATLAB model's implementation of the aerodynamic decay equation using the RK4 method. Overall, there is a 2.46% difference in the final time to reach an altitude of 40 km, which is in a reasonable margin.

The GMAT simulation confirms that the assumption of neglecting the altitude change during the deorbit burn in the MATLAB model is reasonable. In GMAT, a retrograde burn is applied, and the results clearly show that the altitude change at 400 km is negligible. However, the applied delta-V effectively lowers the perigee, enabling a moderately fast re-entry time. This validates the use of the deorbit burn and the assumptions made, as the simulation confirms that the intended trajectory is achieved while maintaining a controlled descent. Additionally, GMAT accounts for perturbations such as Earth's oblateness (J2 effect), third-body influences, and solar radiation pressure. In contrast, the MATLAB model primarily focuses on aerodynamic drag and gravity, and since these additional effects have minimal impact on objects in LEO, they have a negligible effect on the MATLAB simulation.

Minor differences above 300 km may arise from the iterative solution methods used in both simulations, where slight variations in numerical integration techniques can introduce small discrepancies. However, the greatest deviation between the two models occurs below 300 km, where the effects of drag become dominant. This discrepancy may arise from the MATLAB model's use of a simplified drag model, which becomes more noticeable at lower altitudes. This is because the MATLAB model assumes a constant, averaged drag coefficient, whereas GMAT calculates atmospheric drag using a built-in ballistic coefficient approach, which factors in the satellite's shape, mass, and atmospheric density model. Moreover, despite both simulations incorporating variations in atmospheric density based on solar and geomagnetic activity, GMAT uses the MSISE90 model which provides more detailed variations in density.

While more advanced and precise simulators, such as Systems Tool Kit (STK) [13], are available, they are often difficult to access due to restrictions or complexity. However, the level of fidelity in the MATLAB model is appropriate for the short mission duration and the key assumptions made in the model. Given that the satellite's orbital decay is primarily driven by atmospheric drag over a limited time, this simplified approach provides an effective and computationally efficient solution for the task at hand. More sophisticated models could be useful for longer-term simulations or for missions with more dynamic environmental conditions.

#### 4.8 Collision Analysis - Fizza Naqvi

As the number of satellites launched into space continues to rise, along with the increasing amount of orbital debris, collision analysis has become an essential aspect of satellite mission planning. With more objects in space, the risk of collisions grows, making it crucial to assess the potential for satellite impacts with other objects or debris. In particular, the growing population of space debris poses a significant challenge, as not all objects are tracked or catalogued. Table 3 shows the estimated space debris by numbers based on statistical models (MASTER-8), taken from ESA's annual environmental statistics report for 2024 [14]. The table shows a significant number of smaller objects that pose a greater collision risk despite their small size. These numbers highlight the importance of including collision analysis in satellite simulations to ensure mission safety. A limitation of the MATLAB trajectory model used in this study is its assumption that collision risks are negligible, which omits the potential for satellite collisions, especially in crowded regions of LEO. Including collision analysis will improve the realism and safety of future satellite operations.

Size Range	Estimated Number of Objects
Greater than 10 cm	40,500
1 cm to 10 cm	1,100,000
1 mm to 1 cm	130,000,000

Table 3: Estimated Number of Space Debris Objects in Orbit

One way to model the probability of collisions is through the Poisson probability distribution [15], which is commonly used in collision analysis in LEO to estimate the likelihood of events occurring in a given time or space. This model is based on a few key assumptions:

1. The probability of a collision occurring is independent of any prior events.
2. The rate of collisions is constant over time and space.
3. The probability of more than one collision occurring in a given time frame is negligible.

The Poisson probability distribution function is given by the following equation:

$$P(k) = \frac{\lambda^k e^{-\lambda}}{k!} \quad (27)$$

where  $P_k$  represents the probability of  $k$  events occurring,  $k$  is the number of events, and  $\lambda$  is the rate of occurrence parameter.

To determine the probability of no events occurring, we substitute  $k = 0$  into Equation 27, yielding the expression:

$$P(0) = e^{-\lambda} \quad (28)$$

The Poisson distribution is typically used when the probability of two or more events occurring simultaneously is extremely small. If we assume that the likelihood of more than one event occurring is negligible, the probability of exactly one event occurring can be represented as:

$$P(1) = 1 - P(0) = 1 - e^{-\lambda} \quad (29)$$

The rate of occurrence parameter is derived from the kinetic theory of gases and represents the number of collisions that occur between one molecule and others within a given volume over a specified duration. This parameter is influenced by factors such as the molecule's size, the density of the gas, the relative speed of the molecules, and the length of the time period considered. [16]

Applying this kinetic theory to orbital objects, the collision rate between a specified object and all others in a given volume can be determined. The rate of occurrence for orbital collisions is the product of the object's cross-sectional area, the spatial density of other objects (which is the number of objects per unit volume), the relative velocity between the object under consideration and other objects, and the time during which the object is exposed to the risk of collision (the time for de-orbit and decay) [17]. Substituting this analytic form of the rate of occurrence parameter into Equation 29, we obtain the probability of a collision occurring between a given object and any other object within a specified volume over a given time period:

$$P_C = 1 - e^{-A_C \cdot SPD \cdot V_R \cdot T} \quad (30)$$

where  $P_C$  represents the probability of a collision occurring during the time  $T$ ,  $A_C$  is the cross-sectional area of the object (in square kilometers),  $SPD$  is the spatial density of objects (in objects per cubic kilometer),  $V_R$  is the relative velocity between the object and other objects (in kilometers per second), and  $T$  is time (in seconds).

The cross-sectional area of the satellite is  $0.04 \text{ m}^2$ . The spatial density of debris (SPD) can be approximated using NASA's data on the current debris environment in Low Earth Orbit (LEO). This data is visually represented as a graph in Figure 7, providing a clearer depiction of how SPD varies with altitude. By averaging the SPD values over 100 km intervals, the resulting SPD value from 100 km to 400 km is  $2.06 \times 10^{-9} \text{ objects/km}^3$ . The relative velocity between objects in LEO can theoretically range from 0 m/s to twice the orbital velocity. For simplification, the average relative velocity is commonly estimated as  $\sqrt{2}$  times the orbital velocity, which approximates to 10 km/s [19]. This assumption is based on the expectation of an average relative angle of 90 degrees between objects. The time duration considered for the analysis is 456.9 hours, or 1,644,840 seconds, as detailed in section 4.6.

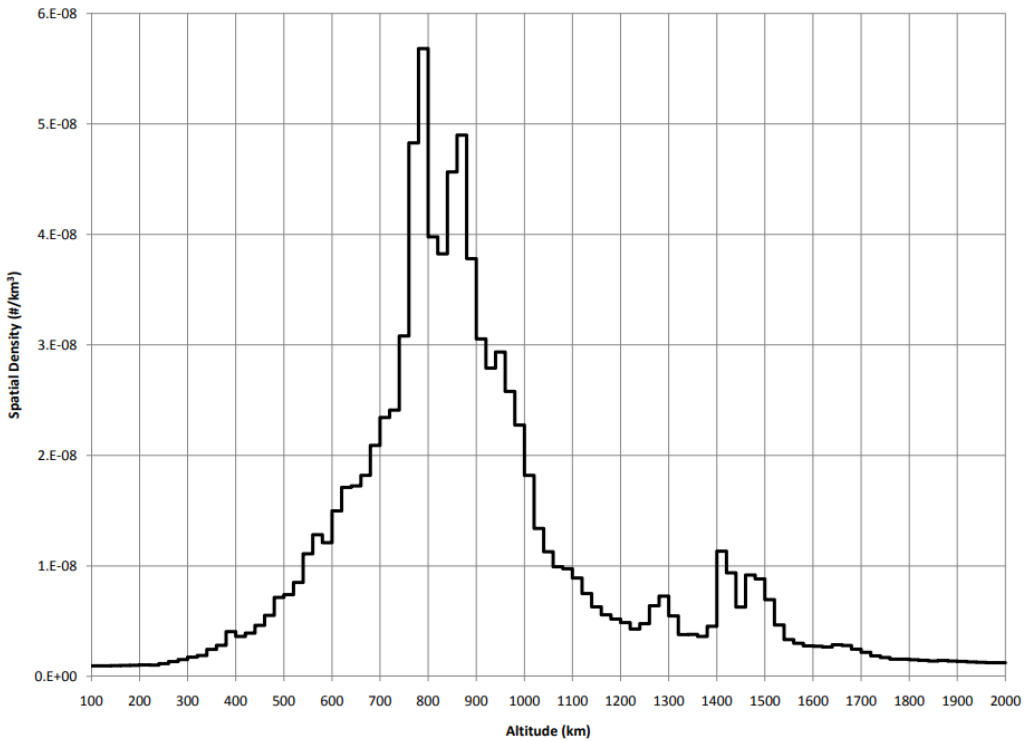


Figure 7: Spatial Density of Debris (SPD) in LEO [18].

Using Equation 30, the probability of collision is calculated to be 0.000657. This value is below NASA's threshold for collision risk in robotic spaceflight, which is set at 1 in 1000 [17], indicating that the likelihood of a collision is negligible. However, it's important to note that this calculation assumes a constant rate of collisions over time and space, which may not fully capture the dynamic nature of space debris. While this assumption is commonly used for simplicity, it may affect the accuracy of the collision probability, especially in regions of higher debris concentration. To further mitigate any potential risk, the CubeSat is equipped with cold gas thrusters and reaction wheels, which are used in conjunction with the MPC system. The cold gas thrusters provide an additional 11 m/s of delta-V (detailed further in section 7.2) allowing the CubeSat to adjust its orientation and maintain the correct attitude for the mission. While the CubeSat cannot perform large-scale collision avoidance maneuvers, the combination of the MPC system, reaction wheels, and cold gas thrusters ensures the CubeSat remains correctly oriented if a small-scale collision was to occur, enabling the mission to continue smoothly. These precautions, alongside the calculated low collision probability, minimise the risk to the mission while maintaining the ability to respond to unforeseen circumstances.

## 5 Mechanical and Structural Design

## 6 Electronics - Hani Moussa

### 6.1 Interfacing and Communications

A critical aspect of the mission's success is the CubeSat's ability to reliably transfer data from the sensor arrays to clients on the ground. To achieve this, the sensors are carefully selected to ensure integration with the onboard computer (OBC), while a reliable communications array is featured in the CubeSat design. The redundancy built into this data transmission process is crucial. Without the successful acquisition and transfer of this data to the ground, the mission would fail to yield results, eliminating the purpose of its investment.

#### 6.1.1 Data System Architecture

The CubeSat generates data through measurements taken by the sensor arrays, which include the thermocouple, pressure sensor, and recession sensor, as outlined in the instrumentation section. This sensor data is then relayed to the onboard computer (OBC), where it is processed, organised into data packets, and modulated for transmission through the communications array.

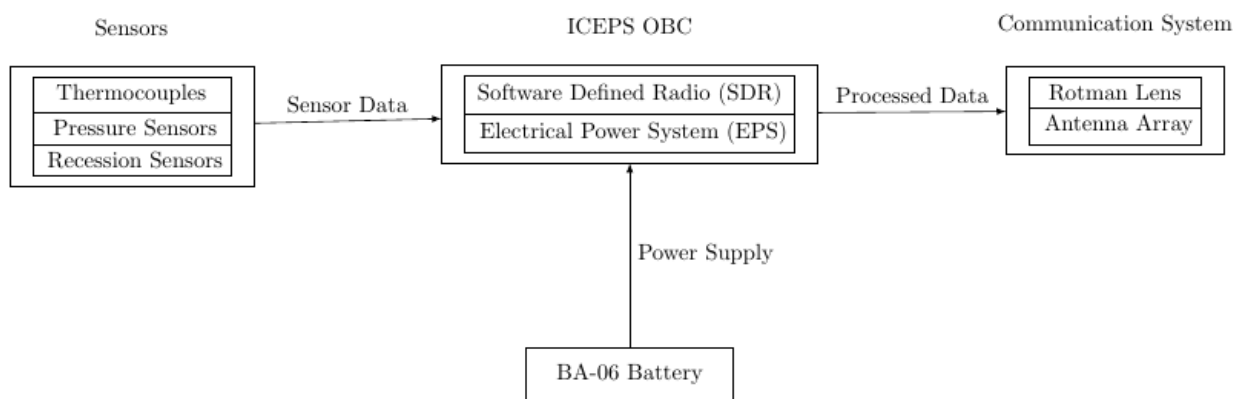


Figure 8: System architecture overview illustrating data flow [GET UPDATED PHOTO]

#### 6.1.2 OBC and Data Processing

One of the onboard computer's main purposes within the context of this mission is to collect, collate and dispatch data. The selected OBC is the Ecuadorian Space Agency's ICEPS Spacecraft System Core, which offers a selection of desirable features, simplifying the CubeSat's design and ensuring a smooth flow of data.



Figure 9: ICEPS Spacecraft System Core

The listed OBC features an Inter-Integrated Circuit ( $I^2C$ ) slave network, a serial communication protocol well-suited for compact embedded systems like in the CubeSat.  $I^2C$  operates on a simple two-wire interface: a Serial Data Line (SDA) and a Serial Clock Line (SCL). This allows multiple slave devices (in this case, the analogue-to-digital converters corresponding to each sensor) to communicate with a single master, the OBC. Each slave device is assigned a unique address, enabling the OBC to selectively query and receive data from individual components without the need for extensive wiring. This significantly reduces system complexity and volume (important considerations in a CubeSat) while ensuring synchronised data acquisition across the sensor arrays. This topology and the ease of its integration make  $I^2C$  an ideal choice for managing the CubeSat's internal communication efficiently.

[PUT  $I^2C$  DIAGRAM HERE]

Communication over  $I^2C$  begins when the OBC, acting as the master, sends the address of the component whose response is needed,. If a device on the bus recognizes its address, it responds with an acknowledgement bit (ACK), allowing the OBC to verify that a device is present before proceeding. Once acknowledged, the OBC can initiate data transfer from the sensor, one byte (8 bits) at a time. After each byte, the OBC sends an ACK to confirm successful reception of the byte. The  $I^2C$  protocol allows for sequential bytes to be sent in a single interaction, meaning that a device can return multiple bytes of data with consecutive messages and ACKs. This process ends when the master (OBC) ends the interaction and sends a new address. This approach makes  $I^2C$  highly scalable, allowing the OBC to poll each sensor for its data as required.

Additionally, ICEPS can be provided with a Software-Defined Radio (SDR), which plays an important part in

the CubeSat's communication system. The SDR is integrated within the OBC, enabling it to handle both the transmission and reception of data in a flexible, reconfigurable manner. Using software control, the SDR can be dynamically adjusted to work across different communication frequencies, modulation schemes, and protocols, making it adaptable for a variety of mission requirements. Once the OBC collects sensor data and processes it into packets, the SDR modulates the data for transmission over the L-Band.

ICEPS is designed for modularity, allowing adaptation to various mission requirements. The configuration options are as follows:

Option	Price (€)
FULL EPS ONLY (I <sup>2</sup> C INTERFACE) + 25W BATTERY	20,500
FULL EPS (USB/I <sup>2</sup> C) + OBC/SDR RADIO/32GB SSD	36,000
FULL EPS (USB/I <sup>2</sup> C) + OBC/SDR RADIO/256GB SSD + LASER COMMS	45,000
FULL EPS (USB/I <sup>2</sup> C) + OBC/SDR RADIO/256GB SSD + LASER COMMS + D/R CONTROL	50,000
FULL EPS (USB/I <sup>2</sup> C) + OBC/SDR RADIO/512GB SSD + LASER COMMS + D/R CONTROL + 25W BATTERY	55,000
FULL EPS (USB/I <sup>2</sup> C) + OBC/SDR RADIO/512GB SSD + LASER COMMS + D/R CONTROL + 50W BATTERY	58,000
FULL EPS (USB/I <sup>2</sup> C) + OBC/SDR RADIO/512GB SSD + LASER COMMS + D/R CONTROL + 100W BATTERY	66,000

The selected (second) configuration includes the SDR and EPS modules, with an external communications system implemented as detailed later in this report. This setup balances cost with system simplicity.

### 6.1.3 Communication Protocol

[DISCUSS PACKET ORGANISATION FOR IRIDIUM SBD + PAYLOAD DESC]

Preamble	Header	Payload	CRC
Sync Bits	Type, Length	Data	Checksum

**Figure:** Example structure of a CubeSat communication packet.

### 6.1.4 Telemetry Strategy

A vital component of the data return process is the communications system. The chosen strategy involves crosslinking mission data to the Iridium satellite constellation, which then relays the data to a ground-based station. This approach has been effective in previous missions, such as the QARMAN CubeSat developed by the Von Karman Institute, for the European Space Agency.

The Iridium constellation consists of 66 active low Earth orbit (LEO) satellites, providing global coverage for voice and data communications. Operating in the L-band, Iridium supports continuous, low-latency data transfer, suitable for this mission. Its global reach ensures reliable communication regardless of reentry location. Also, by transmitting signals upward and away from the CubeSat's trajectory, the system can help overcome communication blackout caused by the plasma sheath formed during atmospheric reentry.

In this period, the CubeSat travels at hypersonic speeds, heating surrounding air to very high temperatures. This ionises the gases around the satellite, forming a plasma sheath: a layer of charged particles. This sheath can interfere with or completely block radio frequency signals, particularly in the UHF ranges, a circumstance known as a communication blackout. Given the mission centres around the collection of data during reentry, and that the CubeSat will not survive the process, communication despite the blackout becomes necessary.

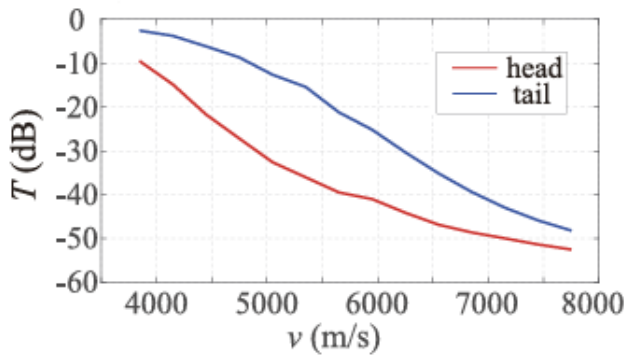


Figure 10: Transmission Coefficient through plasma sheath with velocity [20]

According to the study by Mao et al. (2023) [20], transmission through the plasma sheath becomes more difficult with higher spacecraft velocity or frequency of communications. The signals get absorbed and reflected to higher degrees in these conditions.

One-dimensional electromagnetic wave propagation can be described mathematically as

$$\mathbf{E}(x) = \mathbf{E}_0 e^{-(\alpha+j\beta)x} \quad (31)$$

where  $\mathbf{E}(x)$  is the electric field vector at distance  $x$  into the plasma,  $\mathbf{E}_0$  is the initial field,  $\alpha$  is the attenuation coefficient (causing decrease in amplitude), and  $\beta$  is the phase coefficient (causing phase shift).

The attenuation of an electromagnetic wave as it propagates through plasma can be determined by considering the wave's frequency ( $\omega$ ), the electron density ( $n_e$ ), the collision frequency ( $\nu$ ), and some physical constants [21].

Electron density in a re-entering satellite's wake is typically low enough to lead to a negligible attenuation of signals due to the plasma sheath; the TAIYO satellite's probe found electron densities in the wake of order  $10^5$  [22]. However, research conducted with the Japan Aerospace Exploration Agency (JAXA) involving a numerical simulation model has indicated possible irregularities [23]. Their model indicated a rise between the altitudes

of 80 - 60 km to around  $6.4 \times 10^{16} \text{e}^{-\text{m}}^{-3}$ .

While this was largely due to the ARD's design and the plasma flow past the vehicle shoulder (not present in the CubeSat due to its regular design), it highlights the necessity for anticipation of irregularities. A simulation of L-Band signals through plasma sheaths (based on NASA RAM-C data) was conducted and published in the MDPI's remote sensing journal [24], indicating reasonable possible transmission with electron densities up to  $3 \times 10^{16} \text{e}^{-\text{m}}^{-3}$ . This value, though highly unlikely in the wake region, both serves as a delimiter of extreme conditions and allows for a wider transmission cone from the back of the CubeSat.

The collision frequency in the wake region is quite well-defined. For a model of hypersonic flight with altitude around 50km, the collision frequency for the wake region has been seen not to exceed 0.1 GHz, a value taken as an upper bound for the purposes of the attenuation calculation.

The plasma frequency is the natural oscillation frequency of electrons in a plasma when displaced from their equilibrium positions, and is a relevant quantity to consider when assessing a signal's attenuation [21]. When wave frequency is smaller than plasma frequency, it is attenuated significantly and a larger difference means the signal is generally unable to propagate through it. Around this state, as these values become comparable, attenuation occurs to some degree. The plasma frequency is dependant on the electron density of the plasma:

$$\omega_p = \sqrt{\frac{n_e q_e^2}{\epsilon_0 m_e}} = \sqrt{\frac{(3 \times 10^{16}) \cdot (-1.6 \times 10^{-19})^2}{(8.85 \times 10^{-12}) \cdot (9.11 \times 10^{-31})}} \approx 9.76 \times 10^9 \text{ rad/s.} \quad (32)$$

where

- $n_e$  is the electron density ( $\text{m}^{-3}$ )
- $q_e$  is the charge of an electron ( $\approx -1.6 \times 10^{-19}$  Coulombs)
- $\epsilon_0$  is the permittivity of free space ( $\approx 8.85 \times 10^{-12} \text{Fm}^{-1}$ )
- $m_e$  is the mass of an electron ( $\approx 9.11 \times 10^{-31} \text{kg}$ )

To find the attenuation coefficients seen in Equation 31, the real and imaginary parts of the effective dielectric coefficient ( $\epsilon$ ) are calculated using

$$\epsilon_r = 1 - \frac{\omega_p^2}{\omega^2 + \nu^2} \approx 1.05 \times 10^{-4} \quad (33)$$

$$\epsilon_i = \frac{\omega_p^2 \nu}{\omega(\omega^2 + \nu^2)} \approx 2.21 \quad (34)$$

where

- $\omega$  is the wave frequency (rad/s)
- $\nu$  is the collision frequency ( = 0.1 GHz)

Finally, the plasma attenuation coefficient ( $\alpha_p$ ) and plasma phase coefficient ( $\beta_p$ ) can be derived from these values of permittivity.

$$\alpha_p = k_0 \sqrt{\frac{\sqrt{\epsilon_r^2 + \epsilon_i^2} - \epsilon_r}{2}} \approx 5.70 \quad (35)$$

$$\beta_p = k_0 \sqrt{\frac{\sqrt{\epsilon_r^2 + \epsilon_i^2} + \epsilon_r}{2}} \approx 5.70 \quad (36)$$

where  $k_0 = \frac{\omega}{c} \approx 5.42$  is the free space number ( $\text{m}^{-1}$ )

The attenuation coefficient is the pertinent variable to consider when aiming to calculate attenuation through plasma, but the calculated value does not directly represent the attenuation factor. When seen in the context of Equation 31, the attenuation is the negative exponential of the coefficient.

$$L_p = 20 \log_{10}(e^{-\alpha x}) \quad (37)$$

$$\frac{L_p}{x} = -20\alpha \log_{10}(e) = 49.5 \text{dB/m} \quad (38)$$

where

- $L_p$  is the attenuation due to the plasma (dB)
- $x$  is the distance through the plasma the signal travels (m)

This theoretically allows for up to 0.143m of propagation through high-adversity conditions when considering the link margin as seen in Section 6.1.5. Typically, the wake poses a negligible weakening to signals and has allowed past missions like QARMAN transmission to the iridium constellation [25]. However, it is reasonable to account for potential irregularities such as unexpected plasma electron density spikes. This preparation allows the communication link to remain effective even under a certain margin of unpredictable conditions, increasing the likelihood of successful data transmission.

To mitigate the possible attenuation of radio signals occurring during reentry, and to overcome adversities such as free space path loss (FSPL), a high-gain communication system can be considered to maintain signal strength whilst keeping within reasonable power requirements. However, high-gain antennae are impractical for this mission due to their size, not appropriate to the volume requirements for the CubeSat. Additionally, their narrow beamwidth makes them unsuitable due to the satellite's tumbling. This can result in signal transmission being directed into the high-density plasma toward the CubeSat's direction of travel, rather than toward the wake region where communication is more feasible.

One method of obtaining the high gain required for reliable data transmission while staying within the CubeSat's

size and power constraints is to use beamforming. Beamforming involves using an array of smaller antennae whose relative phases can be controlled to constructively interfere in a desired direction. This effectively steers the beam without the need for mechanical movement, allowing the system to achieve highly directional beams similar to those of a large high-gain antenna, but with significantly reduced physical size. In the context of a tumbling CubeSat, beamforming can also enable a dynamic transmission pattern, improving the likelihood of successful data delivery even despite the changing attitude of the satellite.

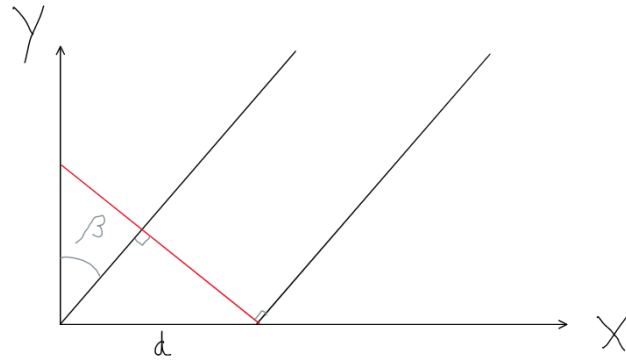


Figure 11: Diagram illustrating change in distance travelled between signals from different beamforming elements

Assume the case of a linear array of antennae. In the above diagram, the electromagnetic wave formed from the element on the left (of distance  $d$  from the right element) travels another  $d \sin(\beta)$ . Therefore, in an array of  $M$  elements, signals arriving from a direction  $\beta$  cause different time delays based on the angle of arrival. These delays are determined by:

$$\tau = \frac{d \sin(\beta)}{c} \quad (39)$$

where  $d$  is the spacing between elements, and  $c$  is the speed of light.

To compensate for these delays (and allow parallel signals to be congruent), a steering vector  $\mathbf{a}(\beta)$  is applied.

$$\mathbf{a}(\beta) = \left[ 1 \quad e^{-j\frac{2\pi d \sin(\beta)}{\lambda}} \quad \dots \quad e^{-j\frac{2\pi(M-1)d \sin(\beta)}{\lambda}} \right]^T, \quad (40)$$

where  $\lambda$  is the signal wavelength. Each term corresponds to each antenna's phase change, ensuring the difference in distance travelled is accounted for. This steering vector is used to generate weights with which to multiply the input signal, allowing every antenna to transmit its corresponding signal.

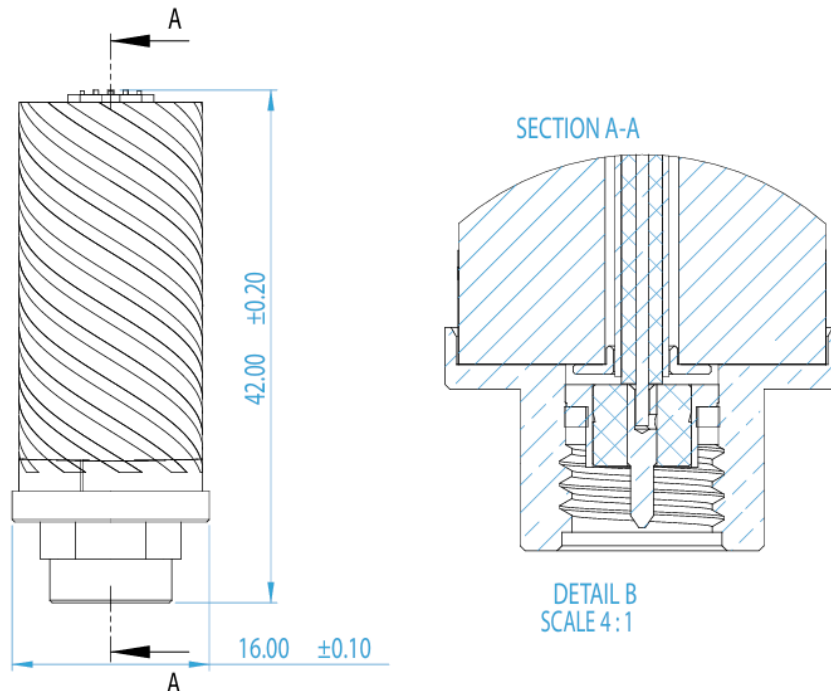


Figure 12: HXDC16010-SA02 Iridium Certus 9704 Antenna dimensions

The selected antenna is the HXDC16010-SA02 Iridium Certus 9704 model, designed for use with the Iridium satellite network. It operates within the required frequency band of 1616 to 1626 MHz and provides a peak gain of 2 dBi. Its compact size, measuring 42 millimeters in length and 16 millimeters in diameter, makes it suitable for arrangement into an array configuration, allowing multiple units to be mounted within the limited volume of the CubeSat. The antenna is also engineered for harsh environments and maintains its performance even when positioned near other antennas.

It is additionally chosen for its compatibility with Iridium's Certus 350 service. Compared to Iridium's Short Burst Data (SBD), which is limited to short messages with a maximum size of 340 bytes, Certus 350 provides a continuous connection with data rates up to 352 kbps. This allows more regular communication, which is suitable for a CubeSat performing continuous data collection. While the data payload requires only [INSERT VALUE HERE] kbps (as referenced in Section 6.1.6), Certus 350 offers plenty of overhead, supporting both standard telemetry and retransmission of corrupted data.

#### [CHOOSE IRIDIUM CERTUS 350 PLAN]

The ICEPS OBC consists partly of an Epik Z2, a combination of a linux computer and an RF transceiver. It provides two Rx and one Tx/Rx SMA connection, which leads to an issue for transmitting signals: only one output can be modulated and connected to an antenna with its given phase. Typically, these phase differences are instantiated through the use of a dedicated beamformer integrated circuit (IC), like the ADAR1000. However, these tools are generally designed for Ka-band inter-satellite communication and are unsuitable for the intended 1.625GHz signal.



Figure 13: Phase-shift control PCB design UPDATE

The phase-shifted outputs are therefore created through the use of a number of carefully selected components. First, the signal is split through the use of a Mini-Circuits ZX10-4A-19+ active splitter. Designed for antenna arrays and RF signals between 1425 - 1900 MHz, the splitter is an apt choice for creating four output paths with uniform phase and amplitude.

Four Phase-shift control printed circuit boards (PCBs), as seen in the design in Figure 13, are placed at the outputs of the splitter, with the intent to prepare each signal before transmission by antenna. One PCB consists of a PCB-mounted male SMA port connected to a standard  $50\Omega$  trace to allow for efficient power transfer. Once the signal has been successfully introduced into the PCB, it is then phase-shifted by a PSemi PE44820 Digital Phase Shifter. While this phase shifter is usually rated for above the desired frequency, it details an extended range of 1.1 – 3.0 GHz for narrow band applications, suitable for the single-frequency communications channel.

[INCLUDE HMC 1119? ALLOWS AMPLITUDE TOO]

Considerable attenuation occurs due to the insertion losses of the splitter and phase shifter, resolved through the use of an amplifier. One aim of beamforming is to achieve a high gain, allowing a strong signal relative to the power applied. This is still the case: an amplifier's output sources a majority of its power from the amplifier's DC source. The signal is amplified from a much smaller power (in this case, the attenuated signal from the phase shifter) to the intended power for a beamformer set-up. This means that an amplifier for an omni-directional antenna alternative consumes far more power to achieve the same dBm signal. It also, as seen in Section 6.2.2 with the CubeSat's communication system power requirement, surpasses the use of multiple software-defined radios, which would require around 2W of power per SDR.

The chosen amplifier is the Mini Circuits GVA-84+, a monolithic amplifier with a high frequency range and a possible gain of over 20dB. Placing the amplifier after the signal attenuation allows for preservation of signal integrity whilst removing the high power requirement necessary had the signal been amplified before losses. The amplified result is communicated to another edge-launch SMA output (connected to the corresponding antenna) through a Skyworks SKY13547-490LF switch.

The purpose of this switch is to allow bidirectional (half-duplex) communication. The amplifier does not function in reverse and would likely lead to unintended damage to the received signal. The switch is single-pole double-throw, which means it can reroute a received signal to an Analog Devices ADL8122 Low Noise Amplifier that boasts a lower noise figure (around 2dB) at the trade-off of only being to amplify weaker signals than the power amplifier used for transmission. Both amplifiers are connected to the phase shifter and, by extension, the splitter (combiner), which both function bidirectionally. The STM32L031C6T6 microcontroller is additionally used to control the PCB through available SPI and DAC pins, whilst receiving instruction from the OBC's I<sup>2</sup>C network.

MATLAB's Phased Array System Toolbox was used to simulate and visualise the radiation pattern of a uniform rectangular antenna array, designed to operate within the Iridium frequency band. A custom antenna element was defined using a cardioid-like magnitude pattern to model the chosen antenna. The element spacing was set to half the wavelength to minimise grating lobes but still maintain constructive interference. The toolbox was used to visualise the array geometry and compute beamforming weights using a steering vector corresponding to azimuth and elevation angles from user input. The resulting directional gain pattern was plotted in 3D, and the peak gain was provided to the user via output.

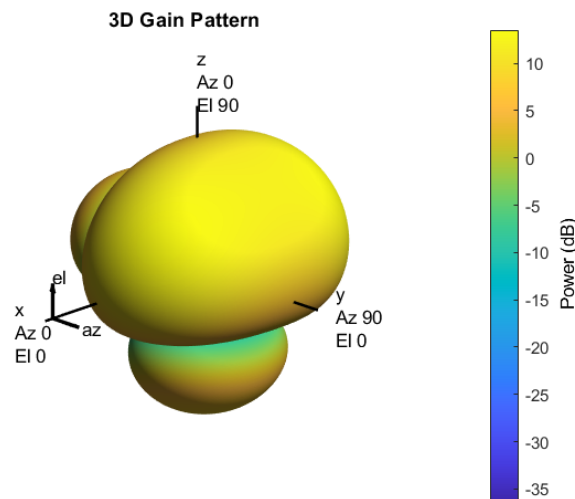


Figure 14: Radiation pattern with 2x2 arrangement (azimuth angle = elevation angle = 30 degrees)

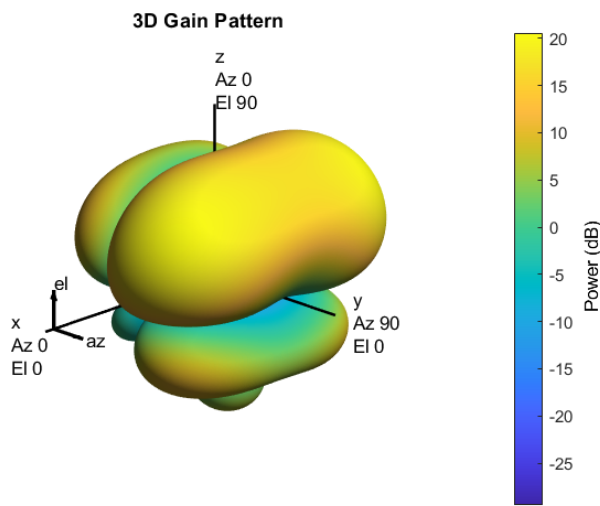


Figure 15: Radiation pattern with 3x3 arrangement (azimuth angle = elevation angle = 30 degrees)

The simulated radiation patterns for two antenna configurations are shown above. The first pattern corresponds to a 2x2 array, which achieves a peak gain of 13.52 dB, while the second pattern is for a 3x3 array, providing a peak gain of 20.56 dB. In both cases, the element spacing is set to 92 mm, which is half of the wavelength at the operating L-band frequency, as previously discussed. As a result, the 3x3 configuration requires a larger physical area but offers the advantage of a higher peak gain.

[EXPLAIN TRADE-OFF (2x2/3x3?)]

Beamforming provides the CubeSat a higher gain, but assumes knowledge of the direction of the plasma sheath's wake. The CubeSat uses its communications array periodically to read an incoming signal from the nearest iridium satellite. It does this by reading signals from [FINISH PARAGRAPH]

Once the direction of transmission is known, the communications array is once again used to transmit data. Until the next occurrence of the direction measuring process, the onboard computer's in-built IMU is used to make slight adjustments to the array's directionality, recalculating the phase shifts for each antenna at every time-step [HOW OFTEN UPDATE?]. This allows for a reliable system due to the relatively low tumbling frequency [HOW LOW?] and cardioid-based radiation pattern from the antennae, granting the CubeSat flexibility in the direction of transmission.

#### 6.1.5 Link Budget

Link budget analysis is an important element of communications systems design, allowing engineers to decide both the efficacy and performance of a particular set-up. It involves the consideration of several different factors affecting the gain or attenuation of a signal from transmission to reception. An equation of the following format is typically used for this analysis [26].

$$P_{rx} = P_{tx} + G_{tx} - L_{tx} - L_{fs} - L_{prop} + G_{rx} - L_{rx} \quad (41)$$

where

- $P_{rx}$  is the received power (dBm)
- $P_{tx}$  is the transmitter power amplifier output power (dBm)
- $G_{tx}$  is the transmitter antenna gain (dBi)
- $L_{tx}$  is the transmitter losses (dB)
- $L_{fs}$  is the free space path loss (dB)
- $L_{prop}$  is other propagation losses (dB)
- $G_{rx}$  is the receiver antenna gain (dBi)
- $L_{rx}$  is the receiver losses (dB)

This takes into account multiple aspects of the data link, from the more anticipated components like the free space path loss  $L_{fs}$ , to more inconspicuous elements like the losses due to components in the receiver  $L_{rx}$ . Another significant detail in this context is the transmitter gain,  $G_{tx}$ , being measured in units of dBi, or decibels relative to an isotropic (3-dimension omnidirectional) antenna. This means the high directionality produced by the beamforming technique (described in Section 6.1.4) is considered in the calculation.

Of additional interest is the Link Margin, a variable directly measuring the feasibility of a data link. It in effect, conveys how much stronger the received signal is than it must be to be secured by the receiver and is given by the following relatively simple equation:

$$LM = P_{rx} - RS \quad (42)$$

where

- $LM$  is the link margin (dB)
- $P_{rx}$ , as defined above, is the received power (dBm)
- $RS$  is the receiver sensitivity (dBm)

MATLAB's Link Budget Analyser application, part of the Satellite Communications toolbox, is used to appraise both data links: both directions between the CubeSat and Iridium satellites. This software poses several advantages when compared to by-hand calculation: it allows for a lower likelihood of errors, uses data from simulated models (as specified in ITU-R P.618) to model attenuation effects like the atmosphere and vastly

simplifies the process of recalculation for different altitudes. It requires several defined inputs to provide the user with useful outputs like the link margin.

The required energy per bit to noise power density ( $\frac{E_b}{N_0}$ ) is a relevant variable in this calculation, representing how much energy is needed for each bit of data to overcome the noise present in the system. The lower the ratio, the less energy is required to successfully transmit the bit. This value is derived from the bit error rate (BER) - for which a typical value chosen for a similar application is  $10^{-5}$  [27]. This leads to an  $\frac{E_b}{N_0} = 9.1\text{dB}$ .

Another pertinent value to define is the  $\frac{G}{T}$  of the Iridium receiver, describing its performance. Despite appearing to be a fraction by convention, it actually represents a logarithmic subtraction (due to the terms being in decibels). This term is defined by

$$\frac{G}{T} = G_r - 10 \log_{10}(T_{\text{sys}}). \quad (43)$$

Using Iridium's system noise temperature  $T_{\text{sys}} = 350\text{K}$  and receiver gain  $G_r = 24.9\text{dB}$  [27] gives a value of  $\frac{G}{T} = -0.54\text{dB/K}$ .

Tag	Name	L3
N1	Distance (km)	2.0620e+03
N2	Elevation (deg)	12.3353
N3	Tx EIRP (dBW)	10
N4	Polarization loss (dB)	3.0103
N5	FSPL (dB)	162.9506
N6	Rain attenuation (dB)	0
N7	Total atmospheric losses (dB)	0.4670
N8	Total propagation losses (dB)	163.4176
N9	Received isotropic power (dBW)	-156.4279
N10	C/No (dB-Hz)	71.6312
N11	C/N (dB)	-3.8094
N12	Received Eb/No (dB)	16.1658
N13	Margin (dB)	7.0658

Figure 16: Link Analysis results of CubeSat Tx to Iridium Rx crosslink as seen in MATLAB, altitude of CubeSat = 50km

These values were applied, and an example communications link was assembled in the Link Budget Analyser tool. As seen in Figure 16, this results in a link margin of about 7.07dB, a comfortable overhead allowing for adverse conditions such as those seen in plasma sheath irregularities described in Section 6.1.4.

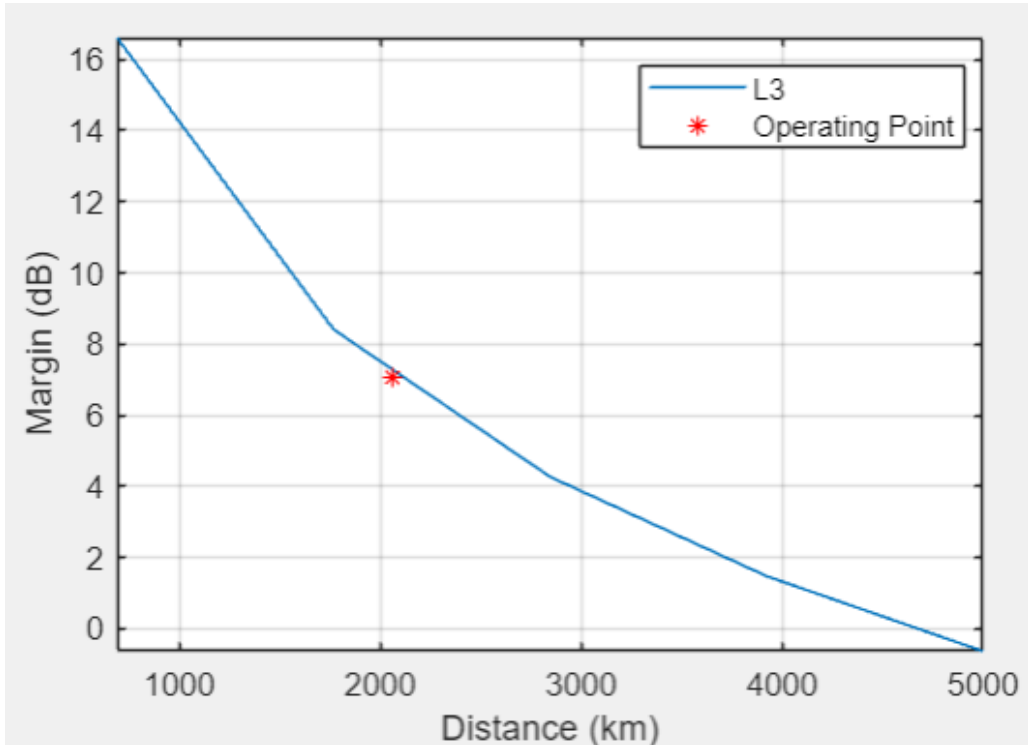


Figure 17: Effect of changing distance between the CubeSat and Iridium satellite on link margin

Two thousand kilometres is a typical value for such a crosslink with Iridium [27], but Figure 17 shows a positive margin (and therefore a successful transmission) to Iridium. Practically, the distance to the nearest Iridium satellite scarcely reaches 2000km [28]. Accounting for the difference in altitude, the distance does not exceed 4500km, confirming a positive link margin regardless of location.

The communications protocol and modulation are identical bidirectionally, and therefore the required bit to noise power density is unchanged when considering the Iridium satellite's transmission back to the CubeSat. The  $\frac{G}{T}$ , however, is specific to the receiver design. Equation 43 is used to measure the performance of the CubeSat receiver system. Due to the principle of reciprocity [29], the transmission radiation pattern of the beamforming array is the same as the receiver sensitivity. The noise temperature, however, is as of yet undefined for the CubeSat. System noise can be considered as a summation of the noise from multiple elements, described by the Friis formula for cascaded noise [30]:

$$T_{\text{sys}} = T_{\text{ant}} + T_{\text{LNA}} + \frac{T_{\text{phase}}}{G_{\text{LNA}}} + \frac{T_{\text{comb}}}{G_{\text{LNA}} \cdot G_{\text{phase}}} \quad (44)$$

where

- $T_{\text{LNA}}$  is the Low Noise Amplifier Noise Temperature (K)
- $G_{\text{LNA}}$  is the Low Noise Amplifier Gain (linear scale, not dB)
- $T_{\text{phase}}$  is the Phase Shifter Noise Temperature (K)
- $G_{\text{phase}}$  is the Phase Shifter Gain (linear scale, not dB)

- $T_{\text{comb}}$  is the combiner Noise Temperature (K)

The gains are simply referenced from the relevant datasheets:  $G_{\text{LNA}} = 39.8$  and  $G_{\text{phase}} = 0.251$ . The noise temperatures, however, are calculated from the noise figure of the devices using the following standard relation [31]:

$$NF = 10 \log_{10} \left( \frac{T_{\text{noise}}}{290} + 1 \right) \quad (45)$$

Once the result is again converted into decibels, the results are  $T_{\text{LNA}} = 138\text{K}$ ,  $T_{\text{phase}} = 871\text{K}$  and  $T_{\text{comb}} = 1070\text{K}$ . The antenna temperature noise is not as simple, varying on the contextual information of the CubeSat's telemetry.

MATLAB is used to estimate the antenna noise temperature based on the radiation pattern seen in Figure 14 and the integral of the noise temperature over the range of the array weighted by the radiation pattern [32]:

$$T_{\text{ant}} = \frac{1}{4\pi} \int_0^{2\pi} \int_0^{\pi} G(\theta, \phi) T(\theta, \phi) \sin \theta d\theta d\phi = 53.78\text{K} \quad (46)$$

Using Equation 44, the system temperature noise is given by  $T_{\text{sys}} = 220\text{K}$  and therefore the CubeSat's total  $\frac{G}{T} = -9.90$ . Though much lower than the performance of the high-budget Iridium satellite (designed to receive signals through the atmosphere), the power and gain is far higher than in the CubeSat's transmission.

Tag	Name	L3
N1	Distance (km)	1.8288e+03
N2	Elevation (deg)	-30.4348
N3	Tx EIRP (dBW)	30.8700
N4	Polarization loss (dB)	3.0103
N5	FSPL (dB)	161.9084
N6	Rain attenuation (dB)	-
N7	Total atmospheric losses (dB)	-
N8	Total propagation losses (dB)	161.9084
N9	Received isotropic power (dBW)	-134.0487
N10	C/No (dB-Hz)	84.6505
N11	C/N (dB)	9.2098
N12	Received Eb/No (dB)	29.1851
N13	Margin (dB)	20.0851

Figure 18: Link Analysis results of Iridium Tx to CubeSat Rx crosslink as seen in MATLAB, altitude of CubeSat = 50km

MATLAB's Link Budget Analyser tool was once again used to calculate the link margin of the back-transmission from the Iridium satellite to the CubeSat, with the result of approximately 20.1 dB shown in Figure 18. This is far higher than even the CubeSat transmission's link budget, assuring that the process of finding the Iridium satellite's direction (as described near the end of Section 6.1.4) is possible even with fluctuations in permittivity

or unintended attenuation in components.

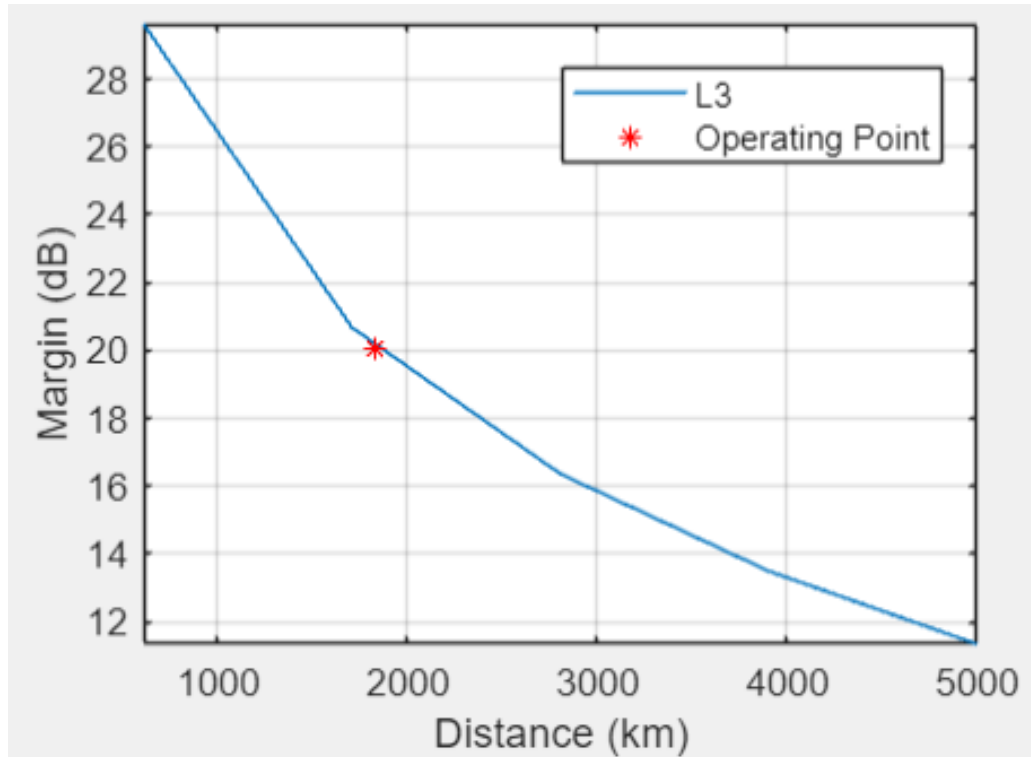


Figure 19: Effect of changing distance between the Iridium satellite and CubeSat on link margin

The plot in Figure 19 shows a similar outcome to that of Figure 17

#### 6.1.6 Data Rate

It is pertinent, when discussing a data collection and transmission process, to account data collection rates. This allows for acquisition and transmission design (including overhead), and accurate advertising to clients of the design's final deliverables. The total data rates can be deduced by reviewing the components listed in Sections 7.1 and 7.5.1, and has been surmised below in Table 4.

Sensor System	Data rate (bps)	Number of Sensors	Total Data Rate (bps)
Temperature	2880	6	17280
Pressure	13760	6	82560
Recession	13760	6	82560
Spectrometer			
<b>Total</b>			

Table 4: Data rates from various sources in the CubeSat

The ablation sensor data rates match those provided by the highest sample rates for each corresponding ADC, as seen in their datasheets. These easily fall into the range allowable by Iridium's Certus 350 service. The

spectrometer, however, uses 2048 pixels of 16 bit representation, and communicates this data via USB around 217 times a second. This equates to a data rate of around 7.1Mbps, far more than can be reasonably transmitted from the CubeSat.

Therefore, a compromise arises. An increased sample rate results in more valuable data, but also more power consumption and a higher data rate to accommodate.

## 6.2 Electrical Systems and Power

[DESCRIBE POWER RAILS ON OBC]

### 6.2.1 Orbital Shut-off Period

One of the primary challenges in designing the power system for this CubeSat is managing energy consumption during the long-duration orbital phase, which is expected to last approximately 19 days. During this period, the spacecraft is inactive until the start of atmospheric re-entry. Even if the onboard computer (OBC) alone were to remain powered throughout this duration, the energy demands would be extreme. It draws an average 4 watts of power, which would lead to an energy requirement exceeding 2,000 watt-hours over the shut-off period. Therefore, an alternative mechanism is required to reliably reactivate the satellite in time for reentry while ensuring it is not drained of its energy before the mission is complete.

One potential approach considered was the use of a barometric sensor to detect the increasing air pressure associated with re-entry. However, this was quickly ruled out due to the pressure of the upper atmosphere. According to NASA atmospheric models[REF HERE], air pressure becomes effectively negligible above 20 km in altitude. This would not trigger a meaningful warning according to the planned trajectory for reentry [REF TO TRAJECTORY SECTION]. This, then, was not a suitable approach.

Another approach involved using a GPS module to determine the altitude of the spacecraft. Various space-specific GPS receivers were considered. Although many of these modules would provide the required information, GPS modules demand significant power and volume. For example, the Hexagon OEM719 consumes 1.8W (translating to hundreds of watt-hours over the course of the mission) and is sized at 46 x 71 x 11 mm. Altitude, therefore, is measured through sensor fusion of a (small) magnetometer and the onboard computer's integrated IMU, as discussed in Section 7.3.

These components, however, still have a high power draw, especially when considering the IMU's integration into the OBC. A more viable solution emerges through the use of a low-power Real-Time Clock (RTC) module that remains active throughout the orbital period.

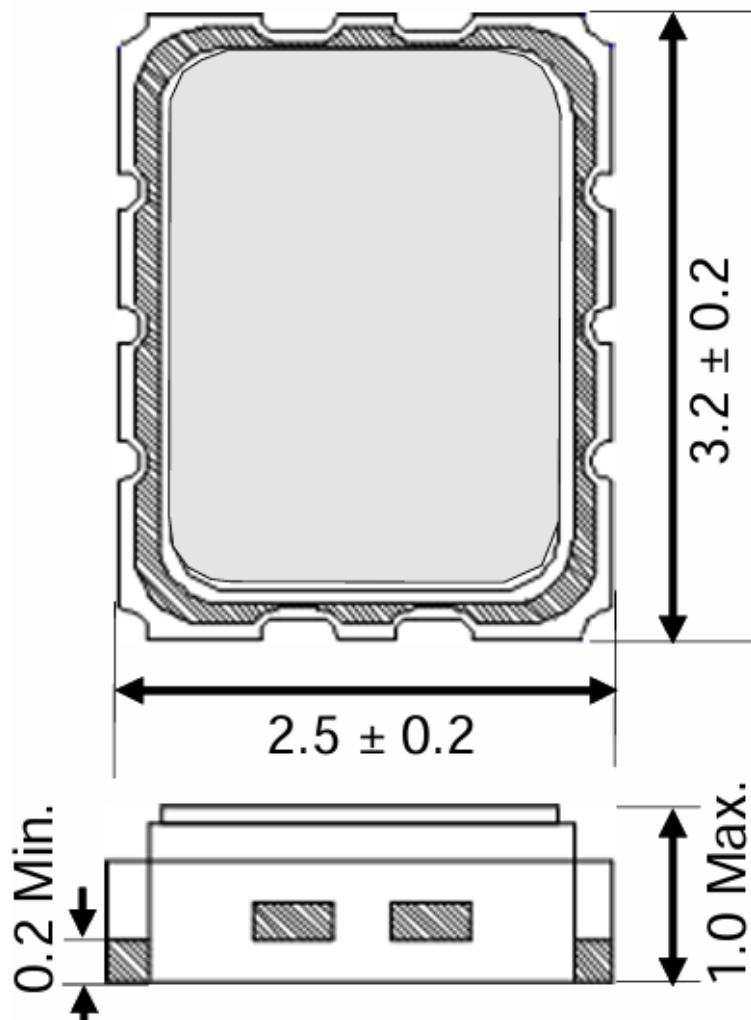


Figure 20: Seiko Epson RA8000CE Real Time Clock Module

The Seiko Epson RA8000CE is chosen for its high temperature range, low power draw, and alarm feature. The latter quality allows the user to provide a specified date and time at which a high digital signal is outputted from the device. It operates with a typical power consumption of  $1.8\mu\text{W}$ , resulting in a negligible energy requirement during the orbital shut-off period. This is a highly efficient solution for ensuring the CubeSat can reactivate prior to re-entry. The minimal energy requirement also grants room for redundancy.

Three RTC components are placed into a OR gate arrangement, lessening the capacity for a single-point failure in reactivation. Additionally, each is powered with a separate Sony CR2032 coin cell battery (theoretically capable of powering them for several years), simplifying and diversifying their power provisions.

Due to the OR gate, once one of the RTCs' alarms outputs a high signal, the onboard computer assesses the current altitude and acts accordingly:

Altitude	OBC Actions
> 200km	Compare position and velocity/acceleration to internal model, reschedule system to reactivate at 200km, and shut off again
200 - 150km	Verify connection to Iridium network, and start collecting and transmitting sensor data
< 150km	Error has occurred. Verify connection with Iridium network, communicate error state, and start collecting and transmitting sensor data

Additionally, the OBC undertakes a procedure to reassess the reliability of each RTC. Upon boot-up, the RTCs are queried over the I<sup>2</sup>C network for their current time and alarm status. According to the component's datasheet, the time variation is expected to be within 130 seconds per month. If any one RTC deviates beyond this threshold (allowing for a margin due to the shorter mission length) relative to the median, it is logged as likely faulty in the OBC's solid-state drive (SSD), and its alarm function is disabled. [WHAT HAPPENS WITH TWO DISAGREEING?]

### 6.2.2 Operation Power Budget

After reactivation, following the orbital shut-off period, the CubeSat's systems are powered and operational. The components are activated, and the process of data acquisition and transmission begins. The power budget for this operational phase of the mission is described below.

Subsystem	Average Power (W)	Peak Power (W)	Duty Cycle (%)	Avg. Power Usage (W)
OBC			%	
Temperature Sensors			%	
Pressure Sensors			%	
Recession Sensors			%	
Comms Array			%	
Spectrometer			%	
Thrusters			%	
<b>Total</b>				<b>0</b>

This section of the mission is planned to last for 1 hour [NOTE: UPDATE WHEN EXACT LENGTH IS KNOWN]. The total energy requirement for this phase is calculated as the sum of the energy consumed during the operational period and the energy required to support the system reactivation process after the shut-off period:

$$E_{\text{total}} = P_{\text{avg}} \times t_{\text{operation}} + E_{\text{reactivation}} \quad (47)$$

Where:

- $E_{\text{total}}$  is the total minimum energy capacity required (Wh)
- $P_{\text{avg}}$  is the average power consumption during operation (W)
- $t_{\text{operation}}$  is the duration of this phase (hrs)
- $E_{\text{reactivation}}$  is the energy required to restore system functionality after shut-off (Wh)

Substituting values in to find the energy requirement:

$$E_{\text{total}} = (X \text{ W}) \times (X \text{ hr}) + X \text{ Wh} = X \text{ Wh} \quad (48)$$

Therefore, the minimum energy capacity required is **X watt-hours**.

[INTRO BATTERY AND CONNECTION TO OBC]

### 6.2.3 Power Distribution and System Design

[SCHEMATIC GOES HERE]

## 7 Instrumentation

### 7.1 Ablation Sensing - Hani Moussa

The CubeSat is designed to test a different ablative material on each of its six exterior faces. To produce meaningful data for client use, each material sample will be equipped with its own dedicated sensor array. These arrays will measure temperature, pressure, and material recession through a combination of sensors and analogue-to-digital converters. All components are selected to be compatible with the I<sup>2</sup>C communication protocol, allowing for integration with the satellite's onboard computer.

#### 7.1.1 Temperature

Several methods exist for the evaluation of temperature.

Measurement Type	Advantages	Disadvantages
Infrared Camera	Provides a detailed view of temperature distribution over material surfaces	Expensive, difficult to position, and low frequency of measurement
Heat Flux Sensor	Directly measures heat transfer, suitable for use on ablative material surface	Limited temperature range, and do not measure temperature directly
Thermocouple	Can possess a wide temperature range, offer rapid response time, and is cost-effective	Only provides relative temperature difference (i.e. requires reference)

Given the above considerations, infrared cameras are non-ideal given their impracticality in a satellite context. Heat flux sensors, too, do not provide the data desired for this application. Thermocouples are commonly used in a space context, offer a high frequency of data acquisition and are relatively simplistic in their implementation. Thermocouples operate based on the Seebeck effect, which measures the temperature difference between two points and generates an analogue voltage output in response. Among the various types available, Type K thermocouples are the most suitable for this context due to their wide temperature range and proven reliability in aerospace environments. A selection of viable sensors is summarised in the table below:

Product	Temperature Range	Notes
Collins Aerospace 0118MF	-269°C to 400°C	
Sensirion STS21	-40°C to 125°C	Supply voltage 2.1 to 3.6V
TE Connectivity MEAS 410	-200°C to 1,250°C	Precision $\pm 2.2^\circ\text{C}$

Of the options, the TE Connectivity MEAS 410 Thermocouple stands out as the most appropriate choice. Its wide temperature range of -200°C to 1,250°C can more effectively cope with the expected thermal extremes

encountered in orbit. The device also offers acceptable precision and is well-suited for integration into satellite systems due to its straightforward electrical requirements and durability in harsh environments. As such, it represents a reliable solution for temperature monitoring with this application in mind.

This thermocouple requires an analogue-to-digital converter in order to be able to communicate its measurements. With standard type K thermocouple potential difference and temperature relations in mind [ref], the operating voltage for the chosen thermocouple is likely to range between  $-5891 \mu V$  and  $50644 \mu V$ , a fact that the ADC decision should rely on. Additionally, the thermocouple requires a cold junction (reference temperature) in order to measure the temperature of the test material. Many ADCs designed for use with thermocouples are made with CJC (Cold Junction Compensation). This feature creates a junction of known temperature for the thermocouple to use as a reference, simplifying the sensor array's design. The following are listed ADCs potentially usable with the MEAS 410 Thermocouple.

The selected thermocouple requires an analogue-to-digital converter (ADC) to transmit its measurements to the onboard system. Based on standard Type K thermocouple voltage–temperature characteristics [REF HERE], the expected output voltage range is approximately  $-5891 \mu V$  and  $50644 \mu V$ . This range is a factor in selecting a suitable ADC. Additionally, accurate thermocouple measurements depend on a cold junction reference. Many ADCs designed for thermocouple use include integrated Cold Junction Compensation (CJC), which establishes a known reference temperature at the junction point. This feature greatly simplifies the overall sensor array design. A selection of ADCs compatible with the MEAS 410 thermocouple with large temperature ranges is listed below.

<b>Product</b>	<b>Voltage Range</b>	<b>Operating Temperature</b>	<b>Resolution</b>	<b>Interface</b>	<b>CJC</b>
Texas Instruments ADS1118IDGST	0V to 4.096V	-40°C to 125°C	12 bit	I <sup>2</sup> C	No
ST Electronics RHFAD128	-0.3 V to 4.8 V	-55°C to 125 °C	12 bit	SPI	No
Maxim MAX31856	-0.3V to +4.0V	-55°C to 125°C	19 bit	SPI	Yes
Microchip MCP3421	-0.3V to 0.3V	-55°C to 125°C	18 bit	I <sup>2</sup> C	No
Texas Instruments ADS1115	-0.3V to 0.3V	-40°C to 125°C	16 bit	I <sup>2</sup> C	No

None of the listed ADCs offer a perfect match for the application. The MAX31856 stands out with its appropriate voltage range and integrated Cold Junction Compensation, making it well-suited for thermocouple use. However, it communicates via the SPI protocol, which is not available directly on the CubeSat's onboard computer. In contrast, the MCP3421 supports the I<sup>2</sup>C interface, aligning well with the CubeSat's existing communication protocol, and offers a compatible voltage range. Unfortunately, it lacks CJC.

Two potential solutions emerge to address the limitations of the ADC options. The first involves pairing the

MAX31856 with an SPI-to-I<sup>2</sup>C bridge, such as the SC18IS602B. While this approach enables communication with the CubeSat's onboard computer, it introduces trade-offs. These include a reduced operational temperature range and potential constraints on data throughput. The second solution involves externalising Cold Junction Compensation by incorporating a dedicated temperature sensor to monitor the reference junction. Texas Instruments outlines such an approach [REF HERE], which enables accurate compensation through post-processing of the thermocouple signal.

The TMP36 is selected for this purpose. With an operating temperature range of -40°C to 125°C and a history in thermocouple applications, it is a reliable choice for monitoring the cold junction temperature. By integrating the TMP36 alongside the MCP3421 ADC, Cold Junction Compensation can be implemented without relying on native ADC support.

### 7.1.2 Pressure

Pressure sensors used in aerospace applications can vary significantly in size. However, the constraints of CubeSat engineering demand care to volume and mass minimisation. With these limitations in mind, the following sensor options have been selected for their compact size and practicality for integration within a CubeSat:

<b>Product</b>	<b>Pressure Range</b>	<b>Temperature Range</b>	<b>Interface</b>
Honeywell MPR Series	60 mbar to 2.5 bar	0°C to 50°C	I <sup>2</sup> C/SPI
TE Connectivity EPB-25PS-C20004	0 - 1.5 bar	-40°C to 120°C	Requires ADC
Sensata PTE7300-14AM-1B010SN	0 - 10 bar	-40°C to 100°C	I <sup>2</sup> C

The pressure range offered by TE Connectivity's EPB-25PS-C20004 is suitable relative to the pressures considered in Section 8.3.8, and it functions in a wide temperature range. It does not, however, include an integrated ADC.

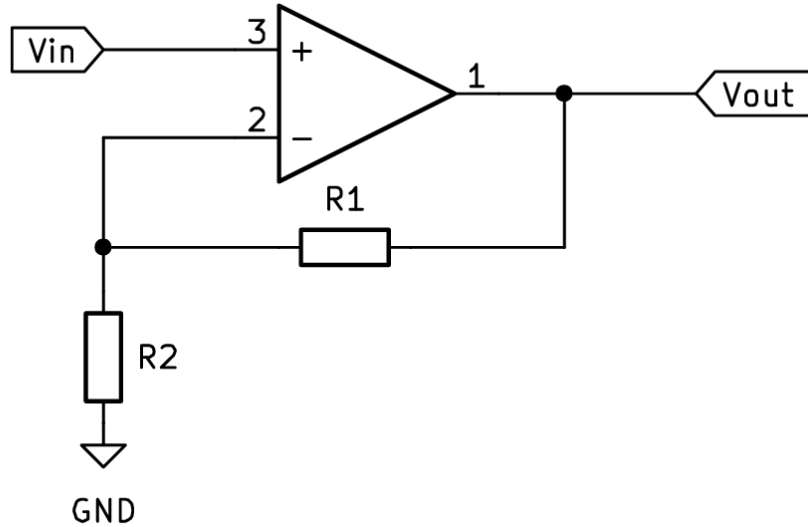


Figure 21: Non-inverting Operational Amplifier Layout

The component features a maximum analogue output of 50mV. This output is amplified through the use of a non-inverting operational amplifier. The Texas Instruments TLV9062 operational amplifier is used as seen in Figure 21, with an intended closed-loop gain for the circuit of 100. The true value, however, is governed by the ratio of the two resistances[33].

$$A = 1 + \frac{R_1}{R_2} \quad (49)$$

With standard resistor values  $R_1 = 1\text{k}\Omega$  and  $R_2 = 100\text{k}\Omega$ , a gain of 101 is achievable with minimal current draw. Coupled with the pressure transducer input, the result is a 5.05V maximum analogue signal. The Texas Instruments ADS1115 ADC is selected to quantify and communicate this value through the OBC's I<sup>2</sup>C network. Due to the limitation by the ADC's 5V supply from the ADC, it is unable to measure beyond this value. Therefore, the maximum pressure detectable decreases to 1.485bar, an acceptably small loss of range.

### 7.1.3 Recession

Recession sensors are critical for measuring the ablation that occurs when the CubeSat surface is exposed to extreme conditions during reentry. These sensors are designed to quantify the rate at which a material is eroded over time, providing valuable data on its durability and performance under thermal stress. In the context of the CubeSat mission, recession sensors will be integrated into each material and will comprise part of its sensor array. By tracking the changes in the material's thickness, the recession sensors will allow for a comprehensive understanding of the ablative properties of test materials.

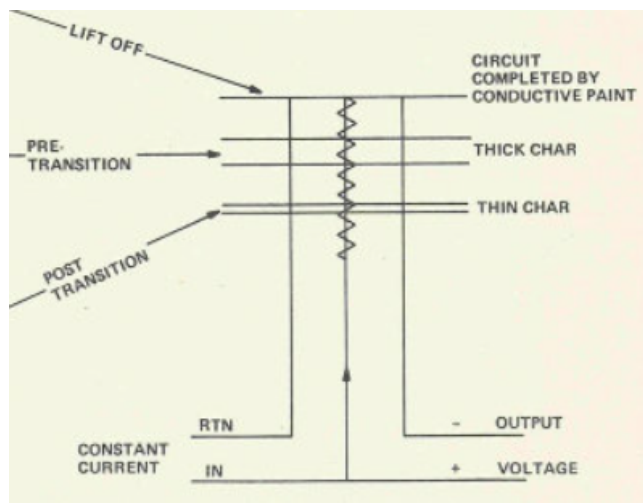


Figure 22: ARAD sensor electrical scheme [REF HERE]

Two main strategies exist to measure material recession. The first approach involves capacitive-based sensors, such as NASA's Ablation Recession and Damage (ARAD) sensor or High Efficiency Ablation Thermography (HEAT) sensor[REF HERE]. These sensors are embedded perpendicular to the direction of ablation, with layered capacitive elements typically a dielectric material sandwiched between conductive plates. As the ablative material erodes, so too do the layers of the capacitor. This physical degradation results in a measurable reduction in capacitance, which can be correlated to the depth of material that has receded. This method allows for real-time monitoring of remaining ablative material, offering a direct and quantifiable insight into material performance under high thermal loads.

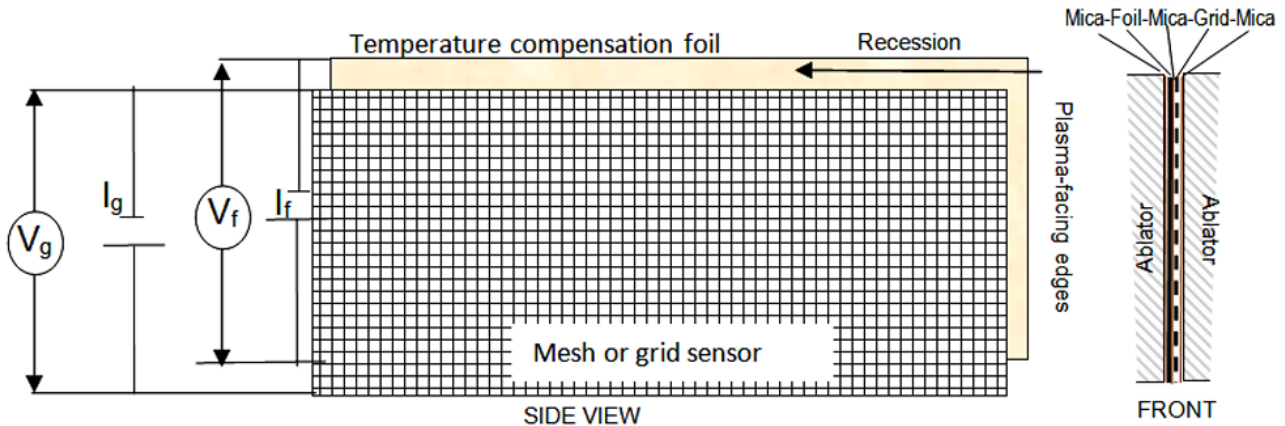


Figure 23: ReWiG Sensor as seen in ESA report [34]

The other strategy is employed by ESA's ReWiG sensor [34]. It includes a mesh of nickel wiring embedded into the ablative surface, positioned perpendicular to it. As the ablative material erodes during reentry, the mesh is similarly removed at an equal rate. This process allows the measurement of the sensor's resistance, which in turn can be used to calculate the remaining thickness of the ablative material. A key component of this system is the (also nickel) temperature compensation foil, which helps to account for temperature-induced changes in the resistance of the mesh. As the temperature fluctuates during reentry, both the mesh and the foil experience

changes in their resistance. By comparing the resistance of the foil to that of the mesh, the sensor can isolate and correct for any temperature-related effects on the nickel mesh's resistance. This ensures that the readings more accurately represent the erosion rate, accounting for thermal error to the resistance of the mesh.

The initial resistance of the Nickel foil can be calculated with the standard resistivity equation and the mesh dimensions provided in the ESA proposal[REF AGAIN]. For a sensor of width 3mm and length through the material 6mm,

$$R_{foil} = \frac{\rho_{Ni}L}{A} = 0.0011875\mu\Omega \text{ (3sf)} \quad (50)$$

where

- $\rho_{Ni} = 9.500 \times 10^{-8}\Omega\text{m}$  is the resistivity of Nickel 200 [35]
- L is the width of the sensor (as the length of the equivalent wire)
- A is the area of the equivalent wire

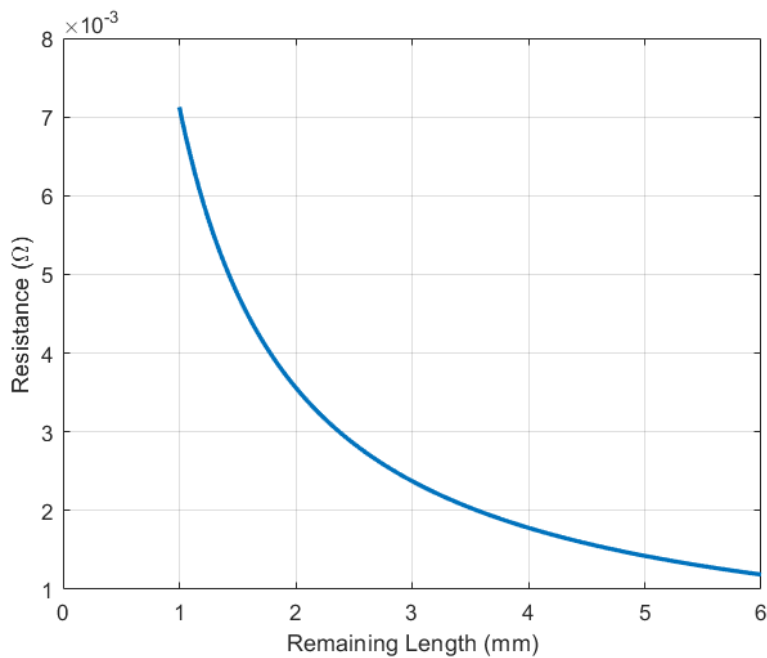


Figure 24: Recession sensor foil resistance change as the material ablates

The mesh can be shown though the use of a simplified model to have a comparable resistance (greater than that of the foil by a factor of 1.25). As the foil and grid erode, the resistance of each increases, allowing recession to be measured.

The desired current is decided by a compromise complicated due to the low resistance of the mesh and foil. A higher current results in a higher, more easily readable voltage, but also a higher power requirement and increased self-heating of the recession sensor. This self-heating may potentially disturb the temperature condition if of significant magnitude.

Current (A)	Initial Voltage (mV)	Final Voltage (mV)	Max Power (mW)
0.1	0.12	0.72	0.072
0.5	0.60	3.60	1.80
1.0	1.20	7.20	7.20
2.0	2.40	14.40	28.80
3.0	3.60	21.60	64.80
5.0	6.00	36.00	180.00

Table 6: Voltage drop and power consumption across recession sensor foil (1.2 - 7.2mΩ) at various currents

Each the mesh and the foil require the same current, and a recession sensor is placed on each of the CubeSat's six faces. This means the power requirement for only the main sections of the recession sensors is twelve times as high as seen in Table 6. 1A is chosen for its ability to produce initial voltages greater than one millivolt whilst keeping power usage low.

This current is provided with the ON Semiconductor CAT4101 Constant-Current LED Driver. Designed for the purpose of delivering a stable, constant current to a low resistance LED, the component would be remarkably suitable in the context of a CubeSat. It can output up to 1A of current and consumes approximately 42.6mW of power; this is high relative to the sensor but not for typical drivers that can reach a 1A output.

The potential difference considered, as detailed in the ReWiG design [34], is between the high potential sides of each the mesh and the foil. This allows for temperature compensation, as the resistive differences between the mesh and foil shapes are the significant factor in forming the varied voltage between the two, temperature affecting both equally. The potential difference spans between approximately 1.20 - 7.20 mV for the foil (described in Table 6), and 1.5 - 9 mV for the grid. The resulting potential difference is a range of 0.3 - 1.8 mV, far too low to be practically sensed by an analogue-to-digital converter.

This signal is therefore also amplified to function with the Texas Instruments ADS1115 ADC. This ADC's lowest upper bound on measurable voltage (with the highest resolution) is 256mV, and therefore the ideal gain for an amplifier would be 142. Using a similar design to Figure 21, the closest simple design (minimising the error caused by tolerances) would include values of  $R_1 = 1\text{k}\Omega$  and  $R_2 = 140\text{k}\Omega$  for a gain of 141. The latter resistor, while uncommon, is offered at a low tolerance of 1% by Yageo as the RC0603FR-07140KL model.

The range used (as in Figure 24) is 1mm to 6mm due to the operating limits of the recession sensor and to keep the system within safe electrical parameter ranges. As the ablative material erodes and the resistance of the sensor increases beyond the upper limit of 7.2mΩ, the voltage drop across the sensor increases too (proportionally given the constant current source and Ohm's law). If this voltage becomes too high, it can exceed the safe operating voltage or power dissipation limits of the LED driver, risking overheating or damage to the electrical system as a whole.

To prevent this, a comparator circuit is used to monitor the voltage across the sensor's amplifier. When this voltage exceeds 256mV (indicating 1mm of the recession sensor remaining), the comparator output triggers a shutdown mechanism. This can disable the current driver directly by opening a MOSFET in the sensor circuit. This safeguard avoids unnecessary power draw or potential component damage.

## 7.2 Cold Gas Thrusters - Fizza Naqvi

The CubeSat will use three of VACCO's CuSP Propulsion System [36] units to achieve the required attitude control and orbital manoeuvring. Each unit is based on a Cold Gas Micro Propulsion System (MiPS), specifically designed for small spacecraft such as CubeSats, providing precise thrust for orbital adjustments and de-orbit burns.

Each MiPS unit is approximately 0.3U in volume, keeping the propulsion system compact and space-efficient. The system uses four 25 mN cold gas thrusters per unit, and collectively, these thrusters generate a specific impulse ( $I_{sp}$ ), which is the ratio of impulse to the mass of propellant, of 69s.

Each propulsion system has an allowed propellant mass of 177g, providing the necessary fuel for the CubeSat to perform the required manoeuvres. The total delta-V of the CubeSat is calculated using the Tsiolkovsky rocket equation [37]:

$$\Delta v = I_{sp} \cdot g_0 \cdot \ln \left( \frac{m_i}{m_f} \right) \quad (51)$$

In the equation, the terms  $m_i$  and  $m_f$  correspond to the CubeSat's mass before and after the de-orbit burn respectively.

Since the required delta-V for the de-orbit burn is about 77 m/s (detailed further in section 4.2), three MiPS units are required to ensure that the CubeSat has sufficient propulsion power to achieve its mission objectives. For the three VACCO MiPS units, a delta-V of 88 m/s is achievable. Therefore, the CubeSat has an additional 11 m/s of delta-V available, allowing for flexibility in mission planning and manoeuvring if necessary.

## 7.3 Altitude Tracking via Sensor Fusion - Fizza Naqvi

### 7.3.1 Overview

Accurate altitude tracking is essential for the CubeSat re-entry experiment to correlate experimental data on material ablation with atmospheric conditions at various stages of re-entry. The hypersonic environment presents challenges such as sensor noise, bias, and drift [38], which can affect the accuracy of measurements. To address these issues, a Kalman filter with sensor fusion is implemented, combining data from an Inertial Measurement Unit (IMU) and a magnetometer. This method improves the reliability of altitude estimation and ensures precise attitude determination, which is critical for correctly orienting the retrograde burn, detailed in section 4.2, and maintaining the desired re-entry trajectory. The resulting improvements in altitude tracking

also allow for a more accurate analysis of ablative materials' demise and their potential environmental impact. Traditional altitude measurement techniques face significant challenges during hypersonic re-entry due to extreme aerodynamic forces, vibrations, and rapidly changing atmospheric conditions. Sensors experience high dynamic loads, resulting in signal distortions and noise. In this context, sensor fusion<sup>3</sup> becomes essential. Applying a Kalman filter to combine data from the IMU and magnetometer helps overcome these limitations. The IMU provides high-frequency acceleration and angular velocity data, which are essential for tracking rapid motion and attitude changes. The magnetometer helps correct for drift in the gyroscope data by providing a stable reference for the CubeSat's orientation, particularly aiding in the accurate estimation of yaw during dynamic motion. The overall sensor fusion algorithm is shown in figure 25.

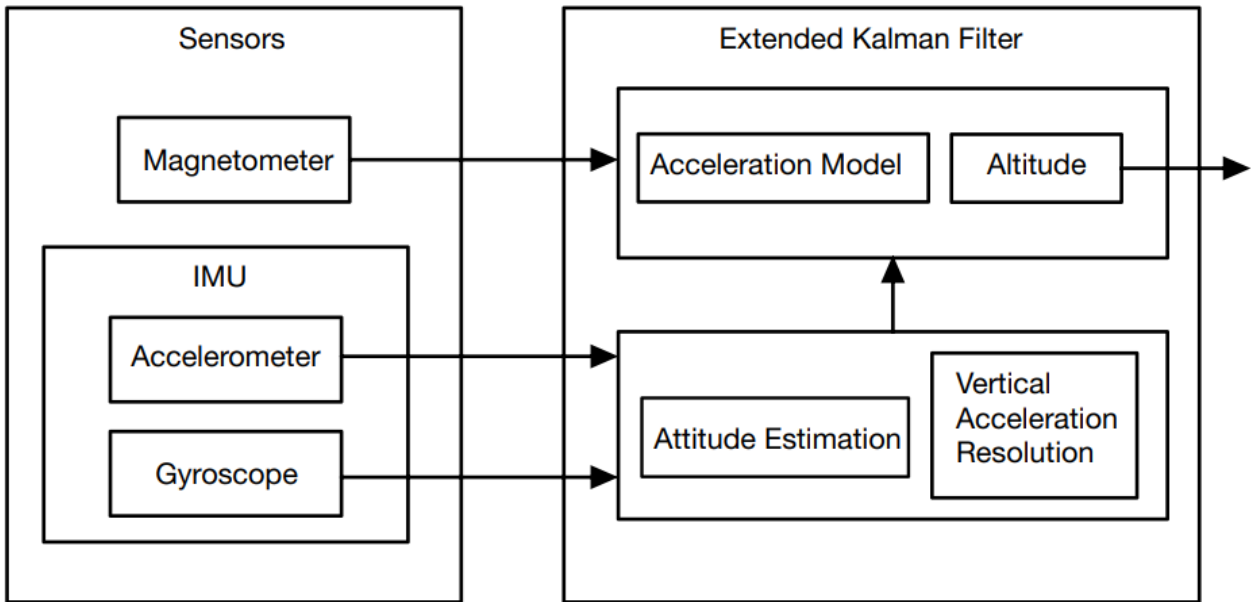


Figure 25: Sensor fusion algorithm to determine altitude.

An IMU consists of two primary components: a tri-axis accelerometer and a tri-axis gyroscope. The accelerometer measures linear acceleration components along three orthogonal axes, denoted as  $a_x, a_y, a_z$ , and detects changes in velocity due to external forces [40]. However, it cannot distinguish between acceleration caused by motion and acceleration due to gravity, introducing drift over time. The gyroscope measures angular velocity ( $\omega_x, \omega_y, \omega_z$ ) about three perpendicular axes (roll, pitch, and yaw) [41], providing information on the CubeSat's orientation. The magnetometer measures the CubeSat's magnetic field components  $m_x, m_y$ , and  $m_z$  relative to the Earth's magnetic field, providing a reference for the CubeSat's orientation. By combining the IMU and magnetometer data with the Kalman filter, altitude estimates are continuously updated, improving accuracy by correcting for drift, noise, and external disturbances.

<sup>3</sup>Sensor fusion integrates data from multiple sensors to provide a comprehensive and accurate understanding of the environment or system being monitored or controlled [39].

### 7.3.2 System Dynamics

The system dynamics are crucial because they define the physical model that the attitude estimation will be based on. By understanding how the attitude state evolves, we can better estimate the vehicle's orientation at any given time.

In discrete-time form, a causal linear time-invariant system in state-space form [42] is given by:

$$\bar{x}_{k+1} = A_d \bar{x}_k + B_d \bar{u}_k + \bar{w}_k, \quad (52)$$

$$\bar{y}_k = C_d \bar{x}_k + \bar{v}_k. \quad (53)$$

where  $\bar{w}_k \in \mathbb{R}$  and  $\bar{v}_k \in \mathbb{R}$  represent the process noise and measurement noise that enters the system at  $t = kT$  respectively.

Both sources of noise enter at the sample time. There is a reasonable assumption for the measurement noise since  $\bar{y}_k$  is sampled at  $t = kT$ , so each measurement is only affected by the noise at that time instant. However, the state equation is derived from the evolution of the state over the period  $t = kT$ , so  $\bar{w}_k$  represents the accumulation of the effect of the process noise over this interval.

It is assumed that the process and measurement noises are uncorrelated, zero-mean, white noise random processes with known covariance matrices:

$$E[\bar{w}_k \bar{w}_k^T] = Q, \quad E[\bar{v}_k \bar{v}_k^T] = R. \quad (54)$$

Additionally, we assume that there is no correlation between the two noise processes:

$$E[\bar{w}_k \bar{v}_k^T] = 0. \quad (55)$$

The state vector for the system [43] is given as:

$$\hat{\mathbf{x}}_k = \begin{bmatrix} \hat{\phi}_k \\ b_{\hat{\phi}_k} \\ \hat{\theta}_k \\ b_{\hat{\theta}_k} \end{bmatrix} \quad (56)$$

In this state vector,  $\hat{\phi}_k$  and  $\hat{\theta}_k$  represent the roll and pitch angles, respectively, at time  $k$ . The variables  $b_{\hat{\phi}_k}$  and  $b_{\hat{\theta}_k}$  denote the biases in the measurements of the roll and pitch angles, respectively, at time  $k$ .

The input vector is:

$$\mathbf{u}_k = \begin{bmatrix} \dot{\phi}_{Gk} \\ \dot{\theta}_{Gk} \end{bmatrix} \quad (57)$$

In this input vector,  $\dot{\phi}_{Gk}$  and  $\dot{\theta}_{Gk}$  represent the angular velocities of the CubeSat around the roll and pitch axes, respectively, at time  $k$ . These angular velocities are measured in the ground frame of reference,  $G$ , meaning they are referenced to the Earth's frame or an inertial frame.

The measurement vector is:

$$\mathbf{z}_k = \begin{bmatrix} \hat{\phi}_{Ak} \\ \hat{\theta}_{Ak} \end{bmatrix} \quad (58)$$

In this measurement vector,  $\hat{\phi}_{Ak}$  and  $\hat{\theta}_{Ak}$  represent the roll and pitch angles of the CubeSat at time  $k$ . These angles are measured in the acceleration frame of reference, denoted by  $A$ .

Varying gyroscope bias causes drift in angular position estimates. To eliminate this drift, the bias is estimated and subtracted from the gyroscope's measured angular rates. This correction provides an updated and more accurate estimate of the CubeSat's angular position [44].

The general state space form for the system [43] is:

$$\mathbf{x}_{k+1} = \begin{bmatrix} 1 & -\Delta t & 0 & 0 \\ 0 & 1 & 0 & 0 \\ 0 & 0 & 1 & -\Delta t \\ 0 & 0 & 0 & 1 \end{bmatrix} \mathbf{x}_k + \begin{bmatrix} \Delta t & 0 \\ 0 & 0 \\ 0 & \Delta t \\ 0 & 0 \end{bmatrix} \mathbf{u}_k + \mathbf{w}_k \quad (59)$$

$$\mathbf{y}_{k+1} = \begin{bmatrix} 1 & 0 & 0 & 0 \\ 0 & 0 & 1 & 0 \end{bmatrix} \mathbf{x}_{k+1} + \mathbf{v}_k \quad (60)$$

### 7.3.3 Instrumentation Models

**Gyroscope** Gyroscopes measure angular velocity in the body frame, but to obtain the time derivatives of the roll ( $\phi$ ), pitch ( $\theta$ ), and yaw ( $\psi$ ) angles in the inertial frame, a transformation is required. This transformation accounts for the non-linearity in Euler angle kinematics and ensures proper mapping between the measured angular rates and the actual rotational dynamics of the CubeSat.

The relationship between the time derivatives of Euler angles and the body-frame angular velocity components  $\boldsymbol{\omega}_b = (\omega_x, \omega_y, \omega_z)^T$  is given by [45]:

$$\begin{bmatrix} \dot{\phi} \\ \dot{\theta} \\ \dot{\psi} \end{bmatrix} = \begin{bmatrix} 1 & \sin \phi \tan \theta & \cos \phi \tan \theta \\ 0 & \cos \phi & -\sin \phi \\ 0 & \frac{\sin \phi}{\cos \theta} & \frac{\cos \phi}{\cos \theta} \end{bmatrix} \begin{bmatrix} \omega_x \\ \omega_y \\ \omega_z \end{bmatrix} \quad (61)$$

**Accelerometer** The accelerometer measures gravitational acceleration along the CubeSat's body axes. By resolving these measurements through trigonometric relationships, estimates of roll and pitch can be obtained. The orientation angles are derived as [46]:

$$\phi = \arctan \left( \frac{a_y}{\sqrt{a_x^2 + a_z^2}} \right) \quad (62)$$

$$\theta = \arctan \left( \frac{a_x}{\sqrt{a_y^2 + a_z^2}} \right) \quad (63)$$

In static or quasi-static conditions, this approach provides reliable roll and pitch angle estimates, assuming that the accelerometer predominantly measures gravitational acceleration. However, in dynamic scenarios, where external accelerations such as translational motion or thruster forces are present, the accelerometer readings become influenced by factors beyond gravity. Consequently, this can lead to inaccurate orientation estimates. To mitigate this, sensor fusion using a Kalman filter is implemented, allowing the separation of gravitational effects from external accelerations. This ensures more precise attitude tracking, even in highly dynamic conditions.

**Magnetometer** The magnetometer measures the Earth's magnetic field vector in the CubeSat's body frame. By combining this measurement with the estimated roll and pitch angles from the accelerometer, the yaw angle can be determined. This provides an absolute heading reference and corrects for gyroscopic drift over time. The tilt-compensated yaw angle is computed as [47]:

$$\psi = \arctan \left( \frac{m_x \cos \phi - m_y \sin \phi}{-m_x \sin \phi \sin \theta - m_y \cos \phi \sin \theta - m_z \cos \theta} \right) \quad (64)$$

### 7.3.4 Kalman Filter

The Kalman filter is widely regarded as an optimal linear estimator in terms of minimising estimation error. The most common approach consists of two steps: prediction and measurement update [42]. The state-space model used for the Kalman filter is based on the linearised system equations, which relate the current state to the next state.

By combining system dynamics with sensor models, the Kalman filter continuously updates the state vector, refining the estimate with each new measurement. Its ability to integrate both predictions from the model and real-time sensor data allows it to correct for drift and noise, making it highly effective for real-time attitude estimation. This adaptive correction process helps mitigate the impact of sensor noise and bias, contributing to more reliable and stable performance even when individual sensors are imperfect.

**Initialisation** The aim of the Kalman filter is to obtain an estimate of the state at the next time step  $\hat{x}_{k+1|k}$  based on all the measurements taken up to the  $(k+1)$ th sample. To initialise this recursion, an estimate of  $\hat{x}_{0|0}$

is required, which is taken to be:

$$\hat{x}_{0|0} = E[x_0]. \quad (65)$$

The covariance of the estimation error is:

$$P_{k|k} = E[(x_k - \hat{x}_{k|k})(x_k - \hat{x}_{k|k})^T], \quad (66)$$

which is initialised as:

$$P_{0|0} = E[(x_0 - \hat{x}_{0|0})(x_0 - \hat{x}_{0|0})^T]. \quad (67)$$

**Prediction Step** In the prediction step, the system's state is projected forward using the system dynamics.

$$\hat{x}_{k+1|k} = A_d \hat{x}_{k|k} + B_d u_k. \quad (68)$$

$$P_{k+1|k} = A_d P_{k|k} A_d^T + Q. \quad (69)$$

**Measurement Update Step** The update step incorporates new measurements from the sensors, adjusting the state estimate to account for noise and sensor errors. This process is repeated iteratively, allowing for continuous refinement of the altitude estimate.

$$L_{k+1} = P_{k|k-1} C_d^T (C_d P_{k|k-1} C_d^T + R)^{-1}. \quad (70)$$

$$\hat{x}_{k|k} = \hat{x}_{k|k-1} + L_{k+1} (y_k - C_d \hat{x}_{k|k-1}). \quad (71)$$

$$P_{k|k} = (I - L_{k+1} C_d) P_{k|k-1}. \quad (72)$$

Note that  $L_{k+1} \in \mathbb{R}^{n \times p}$  is the Kalman gain.

### 7.3.5 Altitude Estimation

Altitude estimation is carried out by integrating measurements from the IMU and magnetometer. The acceleration vector is resolved into its vertical component, which is then used to estimate the vertical velocity and subsequently the altitude of the CubeSat throughout re-entry.

The system is modelled using the following state vector [43]:

$$x_k = \begin{bmatrix} h_k \\ v_k \\ b_k \\ s_k \end{bmatrix}, \quad x_k \in \mathbb{R}^{4 \times 1} \quad (73)$$

Here,  $h_k$  is the altitude,  $v_k$  the vertical velocity,  $b_k$  the accelerometer bias, and  $s_k$  the scale factor that accounts for non-ideal accelerometer behaviour..

The accelerometer measurements are related to the true acceleration  $\alpha_k$  by [48]:

$$a_k = s_k \alpha_k + b_k + n_k \quad (74)$$

where  $a_k$  is the measured acceleration and  $n_k$  represents additive noise. This model allows the system to account for errors in the accelerometer due to scale and bias, though in this case we assume ideal conditions with  $b_k = 0$  and  $s_k = 1$ , i.e., no bias or scale error.

The system dynamics used to update the state are:

$$\dot{h}_k = v_k \quad (75)$$

$$\dot{v}_k = r_k \cdot g_k \quad (76)$$

In this formulation,  $\dot{h}_k$  gives the rate of change of altitude (i.e., velocity), while  $\dot{v}_k$  is the vertical acceleration. The term  $r_k$  denotes the third row of the rotation matrix that describes the CubeSat's orientation, and  $g_k$  is the gravitational acceleration vector.

The IMU and magnetometer alone cannot accurately create an altitude vs. time profile without some form of reference. A barometric sensor, which could provide this reference, is not suitable for altitudes above  $\sim 40$  km due to its limited resolution. As a result, boundary conditions are imposed, specifically at 40km, where the altitude measurement ends. This known final altitude serves as a reference, allowing the model to backtrack and generate an accurate altitude profile over time, even in the absence of a barometric sensor at higher altitudes.

In summary, the Kalman filter compensates for measurement noise and updates the estimates of altitude and velocity in real time. This integrated approach is critical for providing reliable positional data during re-entry, which in turn supports the evaluation of material behaviour and environmental impact at different altitudes.

## 7.4 Attitude Control System - Claudio Vestini

## 7.5 Optical Spectroscopy Hardware - Fizza Naqvi

### 7.5.1 Spectrometer

During re-entry, the spectrometer records the emission spectra of species undergoing transitions between energy states in the shock layer. The spectrometer used for this experiment is the AvaSpec-Mini2048CL [49], shown in 26(a), a compact and powerful spectrometer with a spectral resolution of 2 nm. This spectrometer operates within a temperature range of 0–55°C, so it will be placed inside the CubeSat, beneath the ablative materials, to ensure that its temperature remains within operational limits.

The detectable wavelength range of the AvaSpec-Mini2048CL is 200–1100 nm, making it suitable for capturing emissions from various material classes. Metals typically emit in the UV range (200–400 nm), silica-based materials emit in the UV and visible range (200–500 nm), and carbon-based composites exhibit emissions in the UV and visible regions, with some near-infrared (IR) signatures. Although some carbon-based materials may have emissions extending beyond 1100 nm, the majority of their emissions fall within the spectrometer's detection range, ensuring useful data collection for the study.

### 7.5.2 Fibre Optic Cable

To guide the light from the shock layer to the spectrometer, a multi-furcated fibre optic cable, the FC6-UVIR400-2 [50] from Avantes, shown in figure 26(b), was selected. This cable features six 400 $\mu$ m fibres and has a total length of 2 meters. The fibres are evenly split from a central point, significantly increasing light throughput compared to single-fibre setups. This configuration allows simultaneous collection of light from multiple locations around the shock layer, enhancing spatial coverage. The selection of the 400 $\mu$ m core diameter provides an effective compromise between light collection efficiency and spectral resolution, which is beneficial in the dynamic and high-temperature environment of hypersonic re-entry.

### 7.5.3 Cosine Corrector

To enhance the accuracy of the spectral intensity measurements, a cosine corrector is required. Without this component, optical fibres may preferentially collect light from certain angles, leading to biased intensity measurements. The cosine corrector ensures that the collected light intensity follows a Lambertian response [51], meaning it is proportional to the cosine of the incident angle. This improves radiometric accuracy, enabling more reliable spectral data collection from the re-entry plasma, which emits radiation in multiple directions.

The selected cosine corrector is the CC-UV/VIS/NIR-8MM from Avantes [52]. This corrector is compatible with the FC6-UVIR400-2 fibre optic cable and offers a 180° field of view (FOV), which is well-suited for collecting light over a broad area. The broader FOV complements the multiple fibres in the FC6-UVIR400-2 cable, ensuring that light is collected from multiple points around the shock layer during re-entry. This configuration will optimise the accuracy of the measurements and ensure that the spectrometer captures the full range of radiation emitted during the re-entry process.

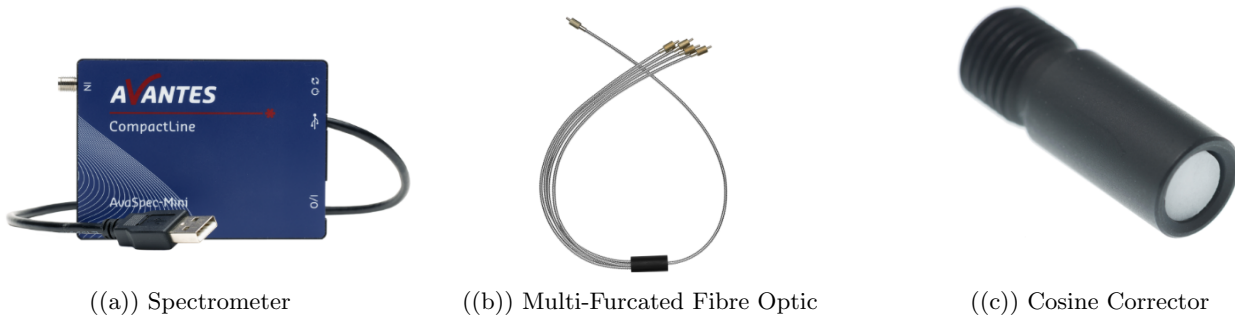


Figure 26: Main 3 components of the spectroscopy system.

## 7.6 Atmospheric Composition Analysis - Fizza Naqvi

### 7.6.1 Overview

This section provides a comprehensive analysis of the atmospheric composition during the re-entry of a CubeSat, focusing on the processes of emission spectroscopy, calibration, and post-mission data analysis. The core objective is to quantify the concentrations of various species in the shock layer, which is formed as the CubeSat interacts with the atmosphere during its re-entry phase. Spectroscopic data is crucial for identifying the species present in the shock layer, as well as understanding their emission characteristics and distribution.

While detailed studies on CubeSat re-entry and its environmental impact are limited, this analysis proposes a valuable framework for quantifying ablation products during satellite demise. The assumptions made in this analysis, while simplifying the complex nature of re-entry dynamics, are necessary for the feasibility of the study. While the exact outcomes cannot be determined due to uncertainties arising from the assumptions made, the approach still offers valuable insights into species concentrations and their potential environmental impact. This can serve as a foundation for further research, particularly in understanding and quantifying the environmental consequences of satellite demise in the upper atmosphere.

### 7.6.2 Pre-flight calibration

As light travels through a spectrometer, the optical properties of the components inside affect the raw data signal received by the spectrometer. Figure 27 displays the difference between the spectrum found in literature and the actual, distorted spectrometer output for a Tungsten halogen light bulb [53]. Based on the raw data, the intensity of the signal at 1000nm appears to be lower than the signal at 620nm. However, in reality, the intensity is about twice as high. Therefore, before launch, the spectrometer must be calibrated to correct for variations in instrument response, ensuring accurate in-flight measurements that may be affected by optical depth effects and local plasma conditions.

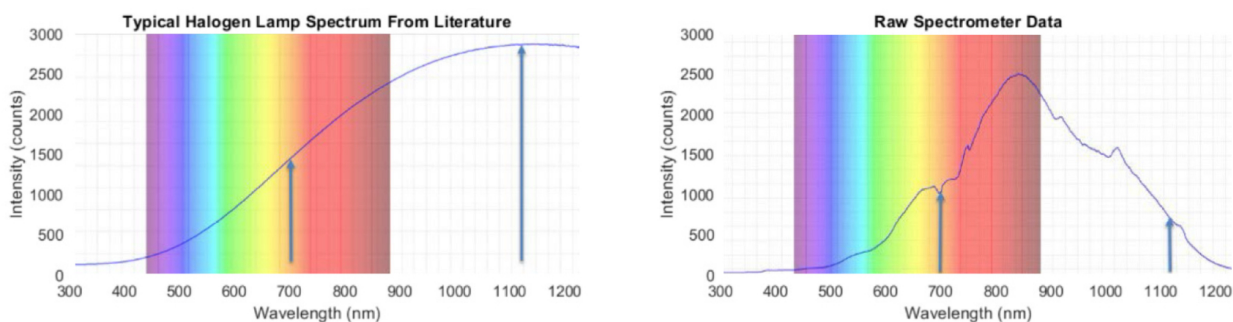


Figure 27: Left image shows the typical halogen spectrum. Right shows the raw data provided by the spectrometer [53].

Calibration is performed using an integrating sphere and standard calibration lamps [54] that emit light at well-characterised intensities and wavelengths. The spectrometer records light from a known calibration lamp under controlled conditions to set baseline spectral intensities and gain factors. The actual spectral intensity of the calibration lamp at each wavelength is known from the manufacturers data or reference bases. The measured

intensity is then used to compute a calibration factor using equation (77), which is applied to all subsequent in-flight data to ensure that the measured intensities accurately reflect the true emission intensities of species within the shock layer.

$$I_{ij} = I_{\text{corrected}}(\lambda) = c(\lambda) \cdot I_{\text{measured}}(\lambda) \quad (77)$$

### 7.6.3 Post-mission data analysis

The spectrometer records the emission spectra of species undergoing transitions between energy states in the shock layer during re-entry. Measurements will be limited to the shock layer, where particles are heated enough to excite species and generate measurable radiation. The spectrometer, positioned within the CubeSat, collects light from the shock layer through the optical fibre detailed in section 7.5.2, which is aligned with a small hole in the outer materials layer. The fibre is set back slightly from the edge of the hole to shield it from excessive heat exposure, reducing degradation and prolonging its operational lifespan. This design ensures that the spectrometer can reliably capture emission data while minimising thermal damage, which is essential for maintaining data continuity throughout re-entry. The optical fibre's acceptance angle defines a cone-shaped measurement region, shown in Figure 28 [55], limiting the spatial resolution but ensuring that light from a specific region of the shock layer is effectively captured. Key emission lines corresponding to species of interest from the ablation products can be identified using spectral databases like the NIST Atomic Spectra Database [56]. Each emission line's wavelength is measured and can be used to identify the specific energy transitions corresponding to the measured emission lines. The NIST Atomic Spectra Database can be used to find the energy levels  $E_j$  and  $E_i$  to calculate the difference between the excited and ground states for each species using equation (78).

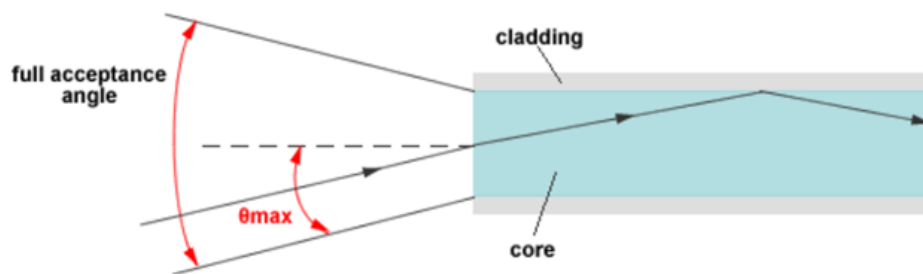


Figure 28: Cone-shaped measurement region for the optical fibre.

$$E_j - E_i = \frac{hc}{\lambda} \quad (78)$$

Where  $h$  is Planck's constant,  $c$  is the speed of light, and  $\lambda$  is the wavelength of the emission line.

Temperature variations during re-entry influence the population of species in excited states. A temperature sensor onboard the CubeSat provides direct measurements of the shock layer temperature. The temperature and particle densities vary between the free stream and the wake region. To account for this, onboard gyroscopes

will track the CubeSat's orientation and position, enabling the distinction between measurements taken in each region.

The relative concentration of species in excited states follows the Boltzmann distribution [57] (equation (79)), which describes how the fraction of atoms or molecules in a given energy state depends on temperature. Using this relationship, the population of different energy states can be estimated.

$$\frac{N_i}{N} = \frac{g_i e^{-E_i/k_B T}}{q} \quad (79)$$

Where  $N_i$  is the population in the  $i$ -th energy state,  $N$  is the total population,  $g_i$  is the degeneracy of the  $i$ -th energy state (the number of available quantum states for a given energy level  $i$ ; this can be found in atomic or molecular databases for the species in question),  $q$  is the partition function,  $E_i$  is the energy of the state,  $k_B$  is the Boltzmann constant ( $k_B = 1.380649 \times 10^{-23}$  J/K [58]), and  $T$  is the temperature at the current altitude.

The raw, measured intensity values need to be multiplied by the calibration factor using equation (77) to obtain the absolute intensity values. Equation (80) [59] relates the emission intensity at a given wavelength to the population difference between energy levels, using the Einstein coefficient  $A_{ji}$  for spontaneous emission. This can be solved simultaneously with a rearrangement of the Boltzmann equation in equation (81) to find  $N_j$  and  $N_i$ .  $A_{ji}$

$$N_j - N_i = \frac{I_{ji}}{A_{ji}} \quad (80)$$

$$\frac{N_i}{N_j} = \frac{g_i}{g_j} e^{-(E_i - E_j)/k_B T} \quad (81)$$

Determining the total number density allows for an estimate of the overall species abundance in the sampled region. Once numerical values for  $N_j$  and  $N_i$  have been obtained, equation (82) can be used to calculate the total number density of particles in all energy states within the cone-shaped volume shown in Figure 28. To extend this measurement beyond the local sampling region, an assumption about the total volume of the shock layer is required, specified later in section 7.6.4. By integrating the estimated number densities across the expected extent of the shock layer, a broader understanding of species distribution during re-entry can be developed.

$$n_{\text{total}} = \sum_i N_i + \sum_j N_j \quad (82)$$

Species concentrations are tracked throughout re-entry by timestamping the emission spectra and correlating the data with altitude information from the IMU and barometer, as detailed in section 7.3. This enables the creation of species concentration profiles, illustrating how the chemical composition of the shock layer evolves with altitude. Variations in species concentrations with altitude can indicate the onset of ablation, as different materials begin to vaporise and emit characteristic spectral lines.

The environmental impact is evaluated by integrating species concentration data over time and converting it to mass using conservation principles. Comparing this with baseline atmospheric models, such as the US Standard Atmosphere Model, highlights deviations due to CubeSat material ablation, offering a foundation for assessing long-term atmospheric effects amid growing small satellite deployments.

#### 7.6.4 Assumptions

Several assumptions are made in this analysis to simplify calculations while maintaining accuracy.

High-speed re-entry can cause a slight shift in emission wavelengths due to the Doppler effect. However, assuming a re-entry velocity of approximately 8 km/s and considering a characteristic emission line for SiO at 250 nm, the resulting Doppler shift is on the order of  $10^{-12}$  m, calculated by equation (83). Given that the resolution of the spectrometer detailed in section 7.5.1 is 2nm, this shift is negligible in the context of this study. Additionally, ablated species are assumed to be distributed around the CubeSat rather than being ejected in a single direction. This leads to a roughly symmetric emission pattern, where some emission sources experience a small positive Doppler shift and others a small negative shift, effectively cancelling out any overall effect.

$$\Delta\lambda = \lambda_0 \frac{v}{c} \quad (83)$$

Furthermore, at an ablation altitude of approximately 80 km, the flow field is rarefied, with a high Knudsen number (ratio of mean free path to characteristic length) indicating minimal molecular interactions. This means that in this regime ablation products are expected to expand isotropically rather than forming a strongly directional plume, as would occur at lower altitudes where continuum flow dominates [60]. This justifies the experimental design choice of placing a fibre-optic sensor on each face of the CubeSat, enabling omnidirectional detection of spectral emissions. By covering all orientations, the setup ensures that material dispersal can be accurately characterised regardless of direction, which is crucial in a regime where ablated particles spread spherically due to the rarefied nature of the atmosphere.

The plasma in the shock layer is considered to be optically thin, meaning that the emitted radiation escapes without significant reabsorption or scattering. This allows direct use of Einstein coefficients to relate emission intensity to population differences in equation (80).

The assumption of a homogeneous shock layer in temperature, density, and composition within the measurement cone is made for this experiment. This assumption is justified as long as the shock layer is thin relative to the spatial resolution of the spectrometer, which is suitable for the scale of the CubeSat's re-entry dynamics. The spectrometer's resolution is sufficient to smooth out any variations in the shock layer, allowing for this simplification in the analysis.

## 8 Aerothermal Environment

### 8.1 Introduction - Claudio Vestini

Since the first successful deployment of a human-made object into Earth's orbit with Sputnik in 1957, over 10,000 satellites have been placed in orbit around our planet [61]. Of these, over 84% are in low Earth orbit (LEO), of which only a relatively small percentage are still operational. This increasing accumulation of orbital space debris poses a significant threat to current and future space missions, which has led to a growing emphasis on effective end-of-life disposal strategies for spacecraft and ground impact mitigation techniques after their demise. To this scope, the European Space Agency (ESA) issued a report in 2014 [62] (later revised in 2023 [63]) that ordered the casualty risk for any re-entry event should be no greater than 1 in 10,000. Several other space agencies, including NASA, the Inter-Agency Space Debris Coordination Committee (IADC) [64] and the European Space Agency (ESA) [65], have since agreed with the prescription.

Accurately assessing casualty risk requires detailed understanding of fragmentation dynamics, surviving component geometries, impact locations, and geographical population density. One of the main sources of uncertainty in these assessments is the prediction of aerothermal heating during early re-entry stages. Unlike typical vehicles designed for re-entry, satellites often feature geometric discontinuities such as sharp edges and facets. This results in unique flow behaviours - particularly around corners - leading to increased local heat fluxes due to boundary layer thinning caused by strong expansions. This is a ripe field of research, as there is great concern associated with the Kessler syndrome [66]: in short, a scenario where the density of debris in Earth orbit is such that catastrophic collisions are inevitable. Existing demise prediction tools adopt various approaches in simulating these re-entry conditions: object-oriented tools like ORSAT and DRAMA use tumble-averaged heating rates for basic shapes [67, 68], while spacecraft-oriented models like SCARAB relate stagnation-point heating to a characteristic radius of curvature [69]. Newer tools such as FOSTRAD and PAMPERO employ local radius-of-curvature methods [70, 71]. None of these tools, however, relies on high-fidelity data for hypersonic aerothermal flow distributions around complex geometries, and a scarce number of studies are available on the topic in the literature.

The AeroThermal team's overarching goal is to ensure CubeSat's thermal environment allows for the correct functioning of all electronics, telemetry, and control systems throughout our mission's phases, and to reliably guarantee the (sufficiently) complete demise of the satellite. The focus in this section of the report is the study of thermal environments to iteratively design CubeSats for commercial materials' testing, with emphasis on high-fidelity computational simulations of the heat fluxes and temperature distributions around the CubeSat throughout our mission. Thermal simulations of this kind inherently carry several layers of complexity. We simplified the analysis by separating simulations into two mission sections: the orbital (8.2), and the re-entry (8.3) phase. The stark differences in aerothermal environment dictate this decision: in orbit, the dominant thermal loading is that of incoming radiation from the Sun, whereas, during re-entry, the thermal environment is dominated by the dissipation of the kinetic energy of the hypersonic flow of air around the CubeSat [72].

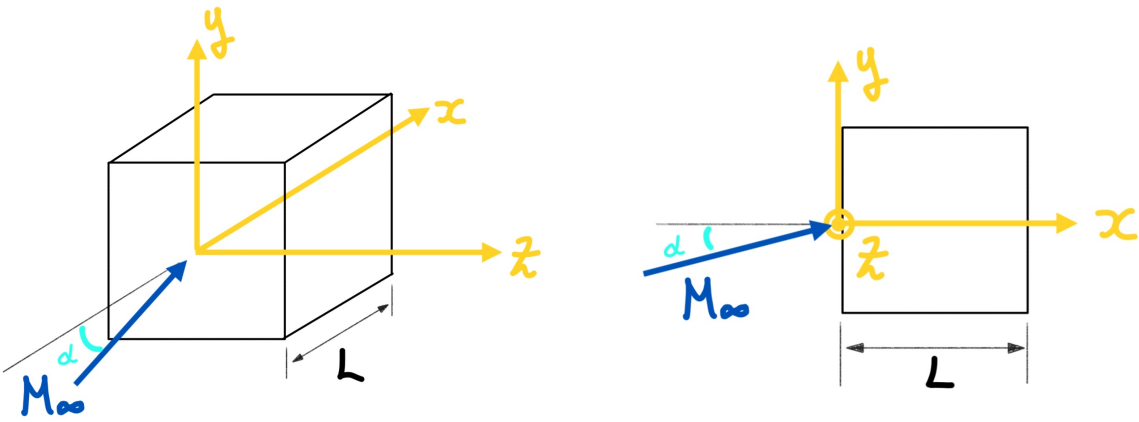


Figure 29: 3D (left) coordinate system for the CubeSat, where  $L = 0.2$  m (8U). A slice through the centre of the cube reveals the 2D ( $x, y$ ) coordinate system (right), where  $z$  is the depth variable into the walls.  $M_\infty := \frac{v_\infty}{a}$ , with  $a = \sqrt{\gamma R T_\infty}$  [ $\text{m s}^{-1}$ ], is the free-stream Mach number, and  $\alpha$  is the in-xy-plane incidence.

Finally, we discuss the demise plan we established for our CubeSat mission. Given the adoption of ablative materials, the passive demise altitude of the CubeSat cannot easily be predicted. To significantly lower the probability of ground impact, we adopted Thermites to ensure complete demise is achieved (section 8.4). Given the nature of our product (a commercial materials testing platform), the aerothermal analysis must be iterated for every choice of heatshield configuration, based on the customer's material choices.

## 8.2 Orbital Phase - Claudio Vestini

### 8.2.1 Heat Equation and Geometry

The three-dimensional, convection-less, unsteady heat equation with internal heat generation is given by:

$$\frac{1}{\alpha} \frac{\partial T}{\partial t} = \nabla^2 T + \frac{G}{k} \quad (84)$$

where:

- $T(\mathbf{x}, t)$  is the scalar temperature field over the CubeSat's walls, with units [K],
- $k$  is the material's thermal conductivity, with units [ $\text{W m}^{-1}$ ]
- $\alpha$  is the thermal diffusivity, given by  $\alpha = \frac{k}{\rho c_p}$ , where  $\rho$  is material density and  $c_p$  is specific heat capacity, and has units [ $\text{m}^2 \text{s}^{-1}$ ]
- $G(\mathbf{x}, t)$  is the volumetric rate of internal heat generation, with units [ $\text{W m}^{-3}$ ]

The reference coordinate system adopted for this analysis is shown in Figure 29.

### 8.2.2 Flight Configuration and Assumptions

A sketch of relevant aerothermal factors during the orbital phase of our mission is shown in Figure 30.

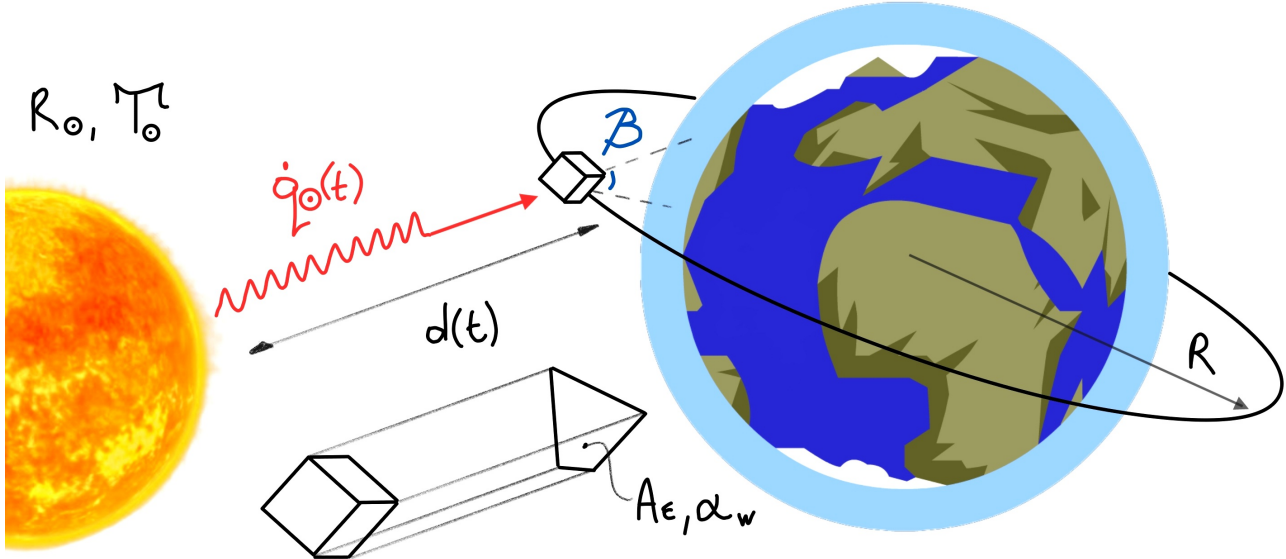


Figure 30: A sketch of CubeSat in orbit around the earth, with incoming radiation intensity  $\dot{q}_\odot(t)$  [W m<sup>-2</sup>] (at the CubeSat's surface).  $R_\odot$  and  $T_\odot$  are sun's radius [m] and surface temperature [K], respectively, whereas  $R$  is the orbital radius measured from the centre of the earth; that is:  $R = R_e + R_{orbit}$ . The sun-to-CubeSat distance is  $d(t)$  [m], and  $\beta$  is the angle between a satellite's orbital plane around Earth and the geocentric position of the Sun.  $A_E$  is the effective thermal area of the CubeSat (geometric property), and  $\alpha_w$  is the absorptivity of the outer walls (material property).

To estimate the surface temperature distribution  $T(x, y, z = 0, t)$ , we make the following assumptions:

- The orbital period can be divided into two sections: when CubeSat is wetted by incoming sunlight, and when CubeSat is behind Earth's shadow. The percentage of time spent in the shadow part of the orbit is given by illumination ratio  $f_e := \tau_{shadow}/\tau_{orbit}$ .
- The orbital period  $\tau_{orbit}$  is much greater than the time taken for the CubeSat to transition behind Earth's shadow. This is justified as the dimensions of the CubeSat are negligible compared to those of the Earth, and the CubeSat travels at high velocity.
- The surface temperature of the sun is constant<sup>4</sup> at  $T_\odot = 5772$  K, and its radius is  $R_\odot = 6.9634 \times 10^8$  m.
- The distance  $d$  can be assumed to be constant. This is because  $d(t) = d_0 + \delta d(t)$ , with  $d_0 = 1\text{AU}$ <sup>5</sup> and  $\max_t \delta d(t) = (R_e + R_{orbit}) / \cos \beta \ll d_0$  (the maximum variation in distance  $\delta d_{max}$  is <0.001% of  $d_0$ ).
- The effective thermal area  $A_E$  of the CubeSat is constant. It can be shown [73, 74] that, for any convex polyhedron illuminated by an infinitely-far-away light source, the average area of the shadow it casts on a two-dimensional plane is one-quarter of its surface area. Hence, for our CubeSat:  $A_E = \frac{1}{4} (A_w)$ .
- The effects of non-radiative heating factors (such as kinetic theory particle interactions) are negligible<sup>6</sup>.

With the above assumptions, the incoming radiation density  $\dot{q}_\odot(t)$  is found to be a square wave with "OFF"

<sup>4</sup>The Sun is considered a very stable star in terms of its energy output. Its total luminosity (total solar irradiance) varies by only about 0.1% throughout its 11-year solar activity cycle, justifying the assumption.

<sup>5</sup>1AU =  $1.495978707 \times 10^{11}$  m

<sup>6</sup>In practice, thermal loading of an orbiting satellite from sources other than the sun can represent 15 % of the total, with trapped particles in Earth's magnetosphere being the dominant contributor [75]. However, a comprehensive analysis to include these location-dependent effects was deemed beyond the scope of this design exercise.

period equal to  $f_e \tau_{orbit}$  and "ON" period  $(1 - f_e) \tau_{orbit}$ . The illumination ratio  $f_e$  is calculated [76] using:

$$f_e = \frac{1}{\pi} \cos^{-1} \left\{ \frac{\sqrt{R_{orbit}^2 + 2R_e R_{orbit}}}{(R_e + R_{orbit}) \cos \beta} \right\} \quad (85)$$

where  $R_{orbit} = 400$  km is our orbital altitude and  $R_e = 6371$  km is Earth's radius. Assuming  $\beta$  remains low for our orbit,  $\cos \beta \approx 1 \implies f_e = 0.3898 \simeq 40\%$ . The evolution of radiation intensity is plotted in Figure 31 (solid red line).

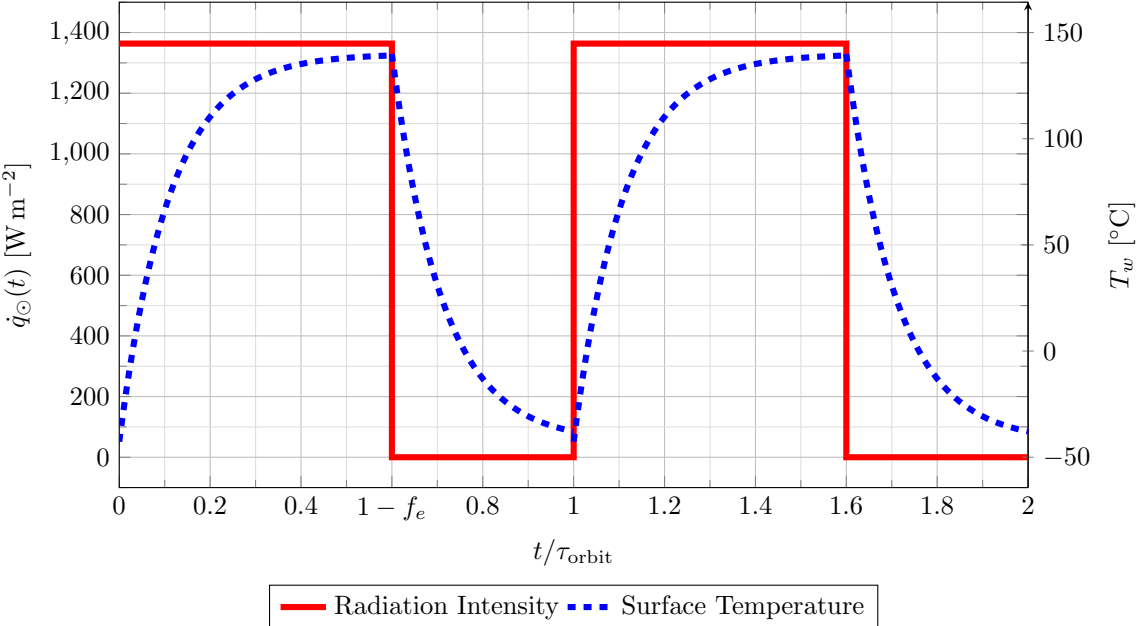


Figure 31: Plot of radiation intensity  $\dot{q}_\odot$  and surface temperature  $T_w$  evolution over dimensionless time.  $t/\tau_{orbit} \in [0, 1 - f_e]$  represents the "ON" period (when CubeSat is directly illuminated), whereas  $t/\tau_{orbit} \in (1 - f_e, 1]$  is the "OFF" period. The period Orbital period is  $\tau_{orbit} \simeq 92.5$  min (as discussed in Section cite-FIZZA), and max radiation intensity intensity is  $1363.6 \text{ W m}^{-2}$ . Surface temperature is found to oscillate between  $-42.7^\circ\text{C}$  and  $139.2^\circ\text{C}$  (see Section 8.2.4).

To compute a worst-case lower bound for the wall temperature, we further assume no heat conduction through the CubeSat's wall during the "ON" period. Wall temperature during the "ON" period will therefore be uniform and constant:  $T(x, y, z = 0, t) = T_w$ . We recall the Stefan-Boltzmann law:

$$\dot{q}_r = \epsilon_r \sigma T^4 \quad (86)$$

where  $\epsilon_r$  is the emissivity of the surface and  $\sigma$  is the Stefan-Boltzmann constant, with a value of  $5.670374419 \times 10^{-8} \text{ [W m}^{-2} \text{ K}^{-4}\text{]}$ .  $\epsilon_r$  can range from 0 to 1, where  $\epsilon_r = 1$  corresponds to a perfect black body (which we will assume for the sun). By Kirchhoff's law [77], emissivity  $\epsilon_r$  and absorptivity  $\alpha_r$  are equal for any thermal surface.

### 8.2.3 Boundary Conditions

The heat intensity at the satellite will depend on the view factor between the two bodies, given by  $\frac{R_\odot}{d}$ . Hence the incident heat intensity at the CubeSat's surface is given by  $\dot{q}_\odot = \alpha_w \left(\frac{R_\odot}{d}\right)^2 (\epsilon_\odot \sigma T_\odot^4) \simeq 1363.6 \text{ W m}^{-2}$  (with black body assumption). During the "ON" period, the heat absorbed by the CubeSat must equal the heat it radiates away if no conduction occurs. A simple heat balance yields:

$$\dot{Q}_\odot = A_E \alpha_w \left(\frac{R_\odot}{d}\right)^2 (\epsilon_\odot \sigma T_\odot^4) = \dot{Q}_w = A_w \epsilon_w \sigma T_w^4 \quad (87)$$

Hence, the steady-state surface temperature will be:

$$T(x, y, z = 0, t) = T_w = T_\odot \sqrt{\epsilon_\odot \left(\frac{A_E}{A_w}\right) \left(\frac{\alpha_w}{\epsilon_w}\right)} \sqrt{\frac{R_\odot}{d}} \approx \frac{T_\odot}{2\sqrt{2}} \sqrt{\frac{R_\odot}{d}} \simeq 139.2^\circ\text{C}$$

We use this as an initial condition to predict the transient conduction behaviour during the "OFF" period.

### 8.2.4 IHCP Solver

With this initial condition, we estimate the surface heat flux experienced by a CubeSat during its orbital heating phase by solving an inverse heat conduction problem (IHCP). The "inverse" nature of this problem stems from the backwards form of the computation: to solve the heat equation *forwards*, we require a priori knowledge of heat fluxes, then solve for temperature distributions. In our case, we know the temperature distribution (it suffices to know the inner and outer wall temperatures), and solve for the heat flux responsible for it. The IHCP is formulated and solved using a numerical finite difference scheme known as Forward-Time Central-Space (FTCS). The heat shield is modelled as a one-dimensional multilayered domain representing an ablative sandwich structure composed of distinct thermal protection layers, each with known thermal properties. It is discretised spatially into  $L$  total nodes across  $M$  material layers, each with thermal conductivity  $k_j$ , specific heat  $c_{p,j}$ , density  $\rho_j$ , and thickness  $L_j$ .

Numerical schemes approximate the field variable of interest  $\phi(x, t)$  as  $\phi(x_l, t_n) \simeq \phi_l^n$  (in higher dimensions, there can be several spatial variables) by discretising the spatial and temporal domains as *stencil* (88). Differences between one scheme and another lie in the choice of the interpolating functions used.

$$(x_l, t_n) = (l\Delta x, n\Delta t); \quad (l, n) \in [0, (M - 1)] \times [0, (N - 1)] \in \mathbb{Z} \quad (88)$$

with domain bounds  $(x_F, t_F)$ , where  $l$  and  $n$  are discrete spatial and temporal indices, respectively, and  $(\Delta x, \Delta t) = (x_F/(M - 1), t_F/(N - 1))$  are the domain step sizes. An important parameter to describe discretisation resolutions lies in the dimensionless Courant number  $C := c \frac{\Delta t}{\Delta x}$ , which represents the ratio between the distance travelled by a disturbance over a time step and the size of the grid spacing ( $c$  is the characteristic speed, equal to thermal diffusivity  $\alpha$  for our case). A choice of  $m$  neighbouring points considered to approximate

the differential operators gives rise to a  $(m - 1)^{th}$  order scheme [78]. This can be inferred from a direct comparison with the solution's Taylor series expansion. FTCS is a suitable choice for the IHCP due to its simplicity, modularity, efficiency, and explicit nature. It has second-order accuracy in space and first-order accuracy in time. In our case, the variable of interest  $\phi$  is scalar temperature  $T$ , and the governing equation (GE) is the unsteady, one-dimensional heat equation (84). Discretising the GE using the FTCS scheme yields:

$$\frac{T_l^{n+1} - T_l^n}{\Delta t} = \frac{1}{\rho_l c_{p,l} \Delta x_l} \left[ k_{l+\frac{1}{2}} \frac{T_{l+1}^n - T_l^n}{\Delta x_{l+\frac{1}{2}}} - k_{l-\frac{1}{2}} \frac{T_l^n - T_{l-1}^n}{\Delta x_{l-\frac{1}{2}}} \right]. \quad (89)$$

To ensure conditional stability of the explicit scheme, the time step must satisfy the FTCS criterion for the most diffusive layer (which is typically the insulating layer within the ablative sandwich structure):

$$\Delta t \leq \min_j \frac{\Delta x_j^2}{2 \alpha_j}, \quad \alpha_j = \frac{k_j}{\rho_j c_{p,j}} \quad (90)$$

Re-arranging equation (89), for interior nodes  $l = 1, \dots, M - 1$ , the multilayer FTCS update of the temperature field  $T$  is:

$$T_l^{n+1} = T_l^n + \frac{\Delta t}{\rho_l c_{p,l} \Delta x_l} \left[ k_{l+\frac{1}{2}} \frac{T_{l+1}^n - T_l^n}{\Delta x_{l+\frac{1}{2}}} - k_{l-\frac{1}{2}} \frac{T_l^n - T_{l-1}^n}{\Delta x_{l-\frac{1}{2}}} \right] \quad (91)$$

At the external surface node  $l = 0$ , the unknown inward heat flux  $q_0^n$  is imposed by

$$-k_{1/2} \frac{T_1^n - T_0^n}{\Delta x_{1/2}} = q_0^n \quad (92)$$

with  $T_0^0 = T_w$ , given above, while at the rear face  $l = M - 1$  we enforce  $T_{M-1}^n = T_{back}(t_n)$ , assuming an initial internal wall temperature of  $T_{back}(t_0) = 20^\circ\text{C}$ . This assumption is justified as the conditions just after orbit insertion are analogous to those right before launch, and we can assume the CubeSat will be thermally insulated by the launch vehicle until insertion.

This scheme was implemented in a Python 3.11 codebase. The forward-time problem is solved repeatedly via the FTCS update (91)–(92). At each step, the new internal and external wall temperatures are updated as new boundary conditions. Temperature evolution  $T_l^n$  is used to reconstruct the surface flux history  $\{q_0^n\}$ . We note that no ablation effects are considered in the scheme. This is justified as the wall temperatures during this mission phase will not be anywhere close to the ablation onset thresholds.

Results for a typical (arbitrary) selection of wall material properties are  $\max_n q_0^n = 433 \text{ W m}^{-2}$ . The temperature evolution over two orbital periods is plotted in Figure 31 (blue dashed line). It shows "capacitor charging" behaviour during the "ON" orbital period, and "discharging" over the "OFF" period. This matches intuition; however, these results will have to be subject to future experimental validation.

### 8.3 Re-Entry Phase - Claudio Vestini

### 8.3.1 The Challenge of Hypersonic Flows - Claudio Vestini

The aerothermal analysis for the re-entry phase is significantly more complex in nature. In general, very few simplifying assumptions can be made when analysing hypersonic flow regimes, and publicly available literature is limited to simple geometries such as spheres and flat-faced cylinders, which were extensively studied in the 1960s [79]. Often, aerodynamic and thermal correlations are taken from these geometries and adapted to more complicated flows, with fudge-factor corrections. In this analysis, we instead wish to directly predict the aerodynamic and thermal loadings of hypersonic flow regimes around a cube. Fluid simulation tools are standard in complex analyses like the one in question. However, these simulations are highly dependent on user choices of mesh geometries, solution formulations and methods, turbulence models, discretisation schemes, and boundary conditions. Poor engineering choices may result in inaccurate, yet precise and well-behaved predictions.

For hypersonic flow regimes, the challenge of obtaining accurate simulation predictions is enhanced: the presence of strong shocks resulting in thin shock layers, entropy layers which interact with viscous boundary layers, extreme flow temperatures behind normal shocks and the complex nonequilibrium thermochemical reactions [72, 80] are all complications that arise in continuum flow regimes. At high values of Knudsen number [81], defined as  $\text{Kn} := \frac{\lambda}{L}$ , where  $\lambda$  is molecular mean free path length and  $L$  is the characteristic physical length scale of the system (sidelength in this case), individual molecular kinetic interactions have to be considered, and the Continuum Model is no longer valid. In the limit of infinite Knudsen number, the regime is known as Free Molecular Flow (see Figure 32).

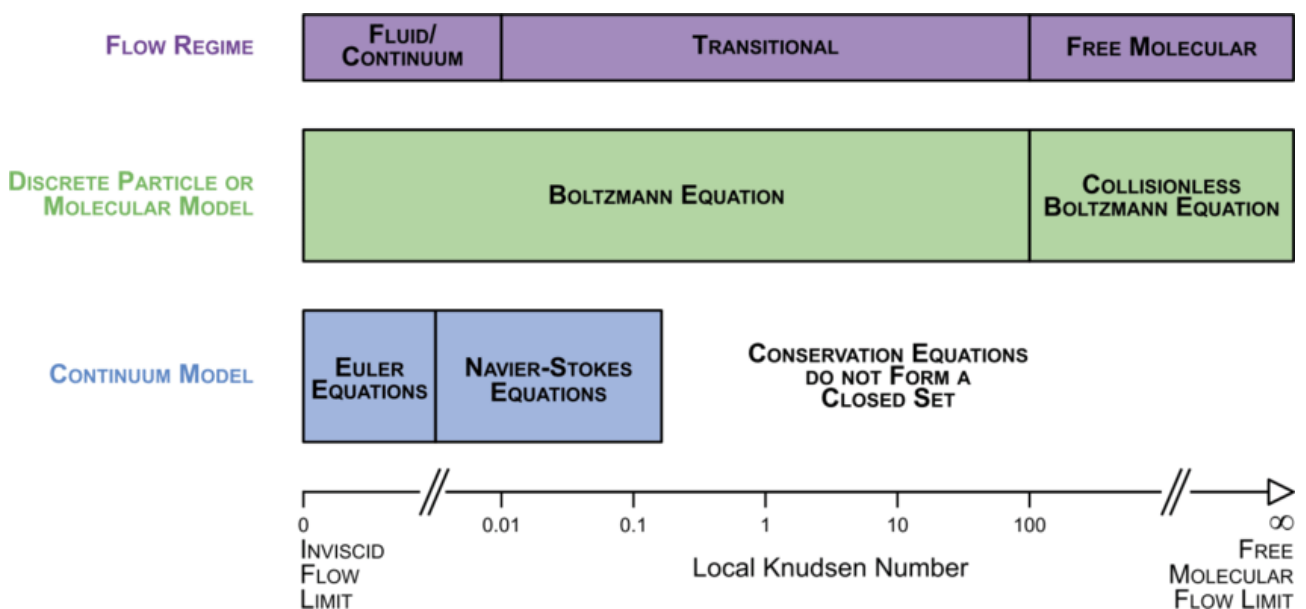


Figure 32: Illustration of flow regimes as a function of Knudsen number, as well as the intervals for which different models (continuum and discrete) are valid. Taken from Marschall et al. (2020), itself adapted from Bird (1994).

Hypersonic flow distinguishes itself from classical supersonic regimes chiefly due to the elevated temperatures reached in the shock layer behind strong shocks, which significantly alter the chemical composition of the gas. As the CubeSat re-enters through the atmosphere, stagnation temperatures can exceed 800 K, activating

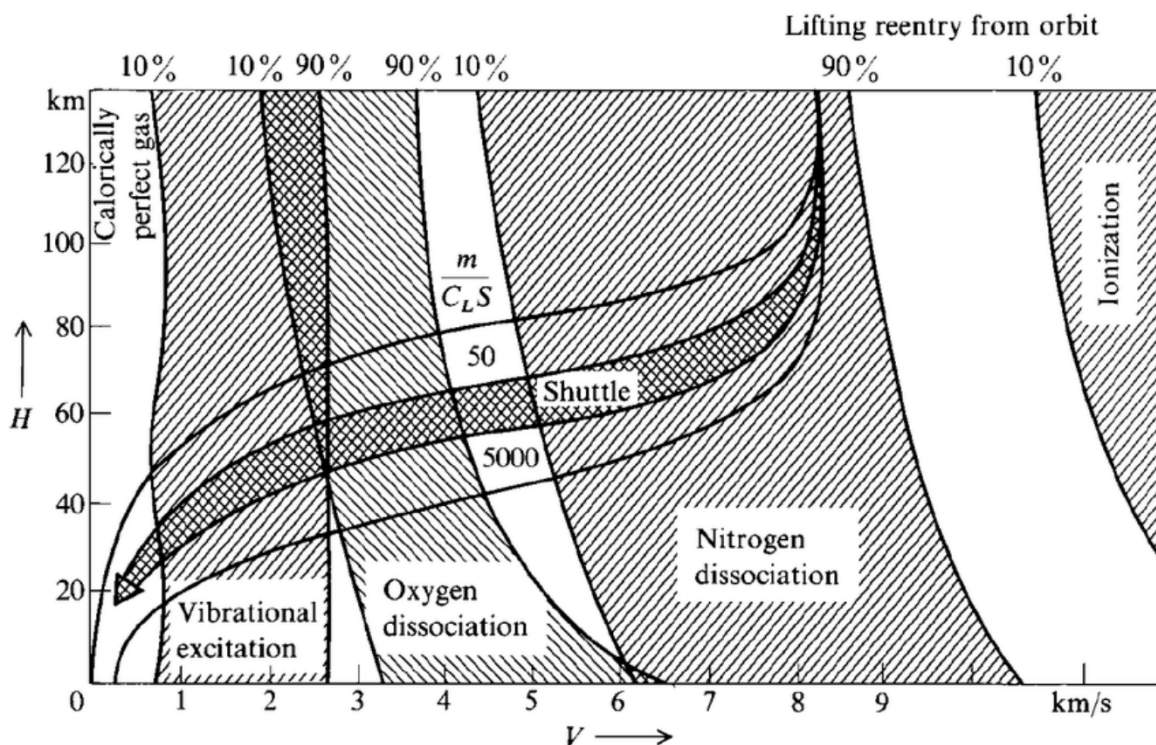


Figure 33: Thermochemical effects in hypersonic flow as a function of altitude and velocity during atmospheric re-entry. The diagram highlights the onset of vibrational excitation, oxygen and nitrogen dissociation, and ionisation, overlaid with typical re-entry trajectories such as that of the NASA Space Shuttle. Adopted from Anderson (2006).

vibrational modes in air molecules and leading to a temperature-dependent variation in specific heats [72]. At approximately 2000 K, these excitations become sufficiently energetic to dissociate molecular oxygen, and at 4000 K, the majority of O<sub>2</sub> has transitioned into its atomic form. These highly reactive atomic species initiate further thermochemical reactions, predominantly involving nitrogen and oxygen combinations. At even higher temperatures, nitrogen molecules (N<sub>2</sub>) begin to dissociate. Due to the strong triple bond in N<sub>2</sub>, this process requires more energy than the dissociation of oxygen and becomes significant above approximately 8000 K [72]. The resulting atomic nitrogen contributes to a dense set of reactions in the shock layer, forming additional species such as nitric oxide (NO) and further altering the thermal and chemical properties of the flow. These effects are especially relevant in the design of thermal protection systems, as the presence of atomic nitrogen increases the reactivity and overall energy content of the boundary layer (see Figure 33 for the full picture).

As temperatures continue to rise, ionisation processes become significant, producing free electrons and giving rise to plasma formation in the surrounding flow [72]. Concurrently, radiation effects from both the boundary and shock layers become non-negligible, with the capacity to cool the surrounding gas while heating the CubeSat's surface. These phenomena - along with the marked nonlinearity of thermodynamic properties at such temperatures - render classical ideal gas assumptions largely inadequate [72]. The pronounced thermal gradients near the front faces of the CubeSat introduce considerable entropy differences into the system, resulting in a significantly thickened boundary layer downstream. Additionally, in many hypersonic scenarios, the close proximity between the shock front and the body (thin shock layers) causes direct interactions between

the viscous boundary and the shock layers, further complicating both the physical structure of the flow and the associated thermochemical environments [72]. This is most relevant at angles of attack close to  $45^\circ$ , where the frontal shock is expected to be attached to the CubeSat's leading edge.

### 8.3.2 Flow Distributions for CubeSats - Claudio Vestini

Schlieren experimental results are available in the literature for critical hypersonic flow configurations around cube shapes. These inform qualitative simulation validation, and are shown in Figure 34.

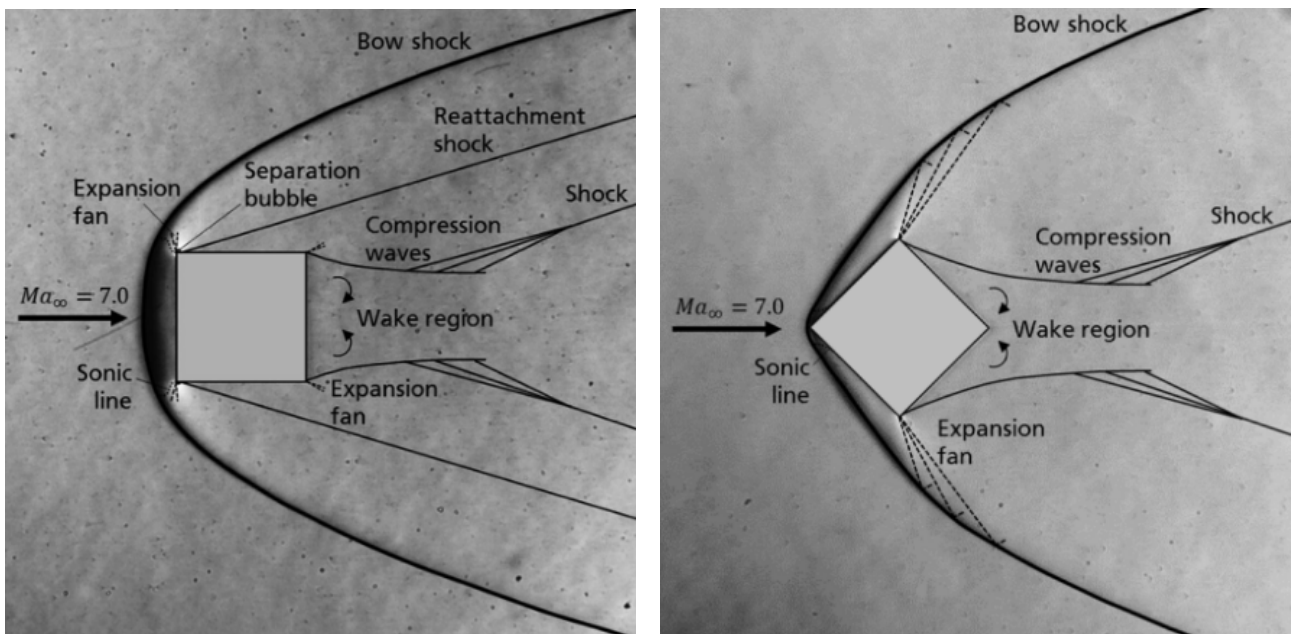


Figure 34: Critical flow configurations for a square in hypersonic flow, with  $\alpha = 0^\circ$  incidence (left) and  $\alpha = 45^\circ$  (right). Courtesy of Seltner, Willems, and Gühan (2019).

The flow patterns at zero incidence predictably show a detached bow shock forming ahead of the CubeSat. Behind this strong shock, an entropy layer wets the CubeSat's walls. The region just behind the shock will be subsonic, where temperatures are expected to reach their highest values. The flow then accelerates around the CubeSat's corners via strong Prandtl-Meyer expansions, forming a separation bubble. It was shown in [85] that the presence of the bubble is strongly dependent on Reynolds number but not Mach number, with separations forming for  $Re > 5 \times 10^4$ . The flow quickly reattaches to the top and bottom surfaces of the CubeSat through reattachment shocks. Not shown in 34 (left), a weak compression wave was found to form about halfway down the top edge of the CubeSat in [85]. Our simulations (see Section 8.3.3) also predict the existence of this Mach wave. The flow is then further expanded around the rear corners of the CubeSat, where a turbulent wake forms. At  $45^\circ$  incidence, the shock is attached to the stagnation corner of the CubeSat. With the absence of top-edge separations and reattachments, the rest of the flow field is similar in nature to the  $0^\circ$  incidence case.

### 8.3.3 CFD Simulations - Claudio Vestini

Computational Fluid Dynamics (CFD) has become an indispensable tool in the field of fluid mechanics, enabling engineers to perform preliminary studies of complex flow fields without the need for physical prototyping. CFD

refers to the numerical solution of the governing equations of fluid flow, namely the Navier-Stokes equations. These represent mass, momentum, and energy conservation over a defined control volume. They are non-linear and coupled, requiring discretisation methods such as Finite Volume, Finite Difference, or Finite Element for non-elementary flow solutions. They are given in equation (93).

$$\frac{\partial \rho}{\partial t} + \nabla \cdot (\rho \mathbf{V}) = 0 \quad (\text{Continuity}) \quad (93a)$$

$$\frac{\partial(\rho \mathbf{V})}{\partial t} + \nabla \cdot (\rho \mathbf{V} \mathbf{V}^T + p \mathbf{I}) = \nabla \cdot \boldsymbol{\tau} \quad (\text{Momentum}) \quad (93b)$$

$$\frac{\partial(\rho E)}{\partial t} + \nabla \cdot [(\rho E + p) \mathbf{V}] = \nabla \cdot (k \nabla T + \boldsymbol{\tau} \cdot \mathbf{V}) \quad (\text{Energy}) \quad (93c)$$

Here,  $\rho$  is the fluid density,  $\mathbf{V}$  is the velocity vector,  $p$  is pressure,  $E$  is the total energy per unit mass,  $\boldsymbol{\tau}$  is the viscous stress tensor, and  $k$  is thermal conductivity.

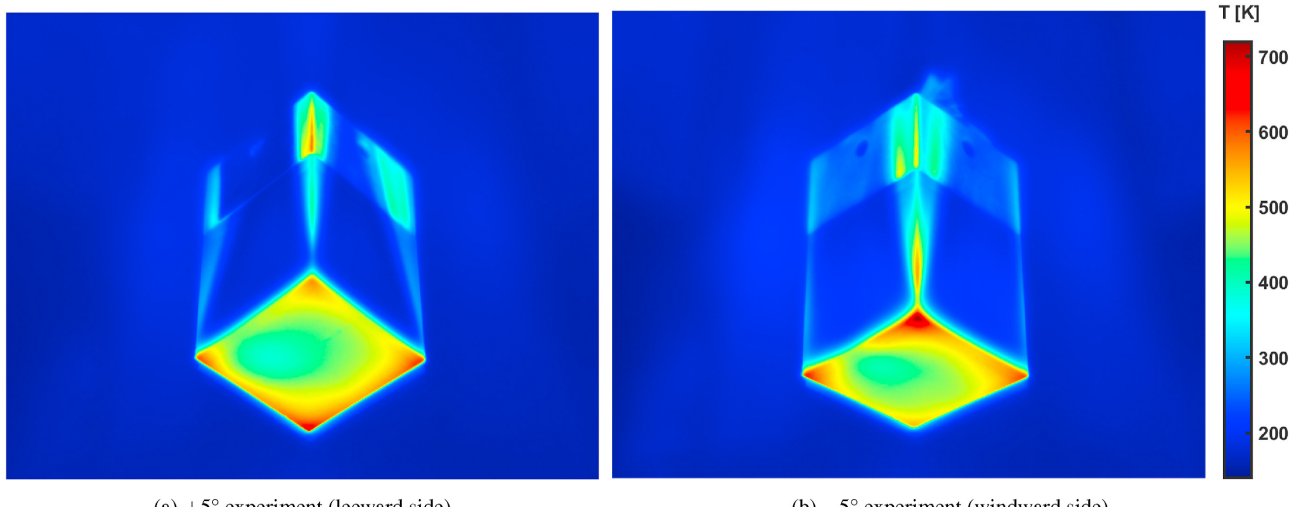


Figure 35: Experimental results of a Cube in Mach 5 flow at 5° incidence performed at the University of Manchester's High SuperSonic Tunnel (HSST). Experiment and figure by Rees et al. (2020). The authors found that incidence had little influence over the maximum static temperature obtained at the corners. The experimental results are used to validate our predictions.

CFD simulation workflows can typically be broken down into:

1. **Geometry creation:** Internal or external flows to be studied, and CAD models can be imported.
2. **Mesh generation:** Most of the effort goes into this step.
3. **Solution setup and calculation:** Assignment of physical and computational models. Steady-state or transient solutions using residual-based convergence criteria (typical of high-fidelity simulations) or fixed-iteration runs (industry).
4. **Post-processing:** Results are analysed and visualised through plots.
5. **Verification and validation:** CFD solutions are often referred to as "garbage in - garbage out".

Validation against experimental results is arguably the most crucial step of the workflow, and often dictates the available choices of simulation conditions. The workflow, therefore, does not always follow the linear path

described above. For hypersonic simulations of cubes, a limited number of research papers are available for validation. In particular, Rees analysed Stanton numbers for Mach 5 flows around a cube for small values of incidence in both 2D [85] and 3D [87] CFD simulations, which they validated against hypersonic wind tunnel experiments [86] (Figure 35). Seltner focused on aerodynamic coefficients and schlieren imaging of Mach 7 flows around a cube [84]. Our simulations were designed to reproduce the flow conditions of these two sets of experiments for validation.

#### 8.3.4 ANSYS Fluent Solver - Claudio Vestini

We adopted ANSYS Fluent, a popular, commercially available integrated CFD software package, for the presented simulations. Fluent solves the two- or three-dimensional compressible Navier-Stokes equations using two primary approaches:

- **Pressure-based solver:** Originally developed for incompressible flows, extended through coupled algorithms for compressible regimes [88].
- **Density-based solver:** Traditional choice for high-speed flows, now generalised with Roe flux-difference splitting for broader applications. Adopted here as it can achieve convergence faster and with less computational expense for supersonic simulations.

Fluent employs the Finite Volume Method (FVM), which is particularly advantageous because of its ability to process complex, unstructured meshes<sup>7</sup> [88].

The software offers a wide range of turbulence models, including RANS (Reynolds-Averaged Navier-Stokes) models such as Spalart–Allmaras,  $k-\varepsilon$  and  $k-\omega$  (BSL or SST), and hybrid RANS-LES (Large Eddy Simulation) approaches such as DES (Detached Eddy Simulation) and SAS (Scale-Adaptive Simulation). Additionally, Fluent supports boundary-layer transition models and is equipped with models for chemical reactions and thermal non-equilibrium, enabling complex simulations involving combustion and multiphase flows. Fluent provides various discretisation schemes for both spatial and temporal resolutions, including first- and second-order accurate methods. It offers both steady-state and transient solutions. The software also features a powerful built-in mesh adaptation module for mesh refinement (more in Section 8.3.6).

#### 8.3.5 Simulation Parameters - Claudio Vestini

In this report, two-dimensional, compressible Navier-Stokes results are presented. One of the three simulations (Run 3) considered reacting governing equations, with the other two running the non-reacting equations to match the conditions of [85, 87]. It is noted that, for the flow conditions of the validation papers, the maximum temperature recorded (behind the shock) did not exceed the 2000 K threshold for O<sub>2</sub> dissociation, which is a further justification for the choice of non-reacting physics. We adopted the  $k-\omega$  SST (Shear Stress Transport) turbulence model, the industry standard for high-speed flows around sharp geometries. A common challenge

---

<sup>7</sup>A mesh is said to be "unstructured" if its constituent polyhedra are not arranged in an orderly fashion.

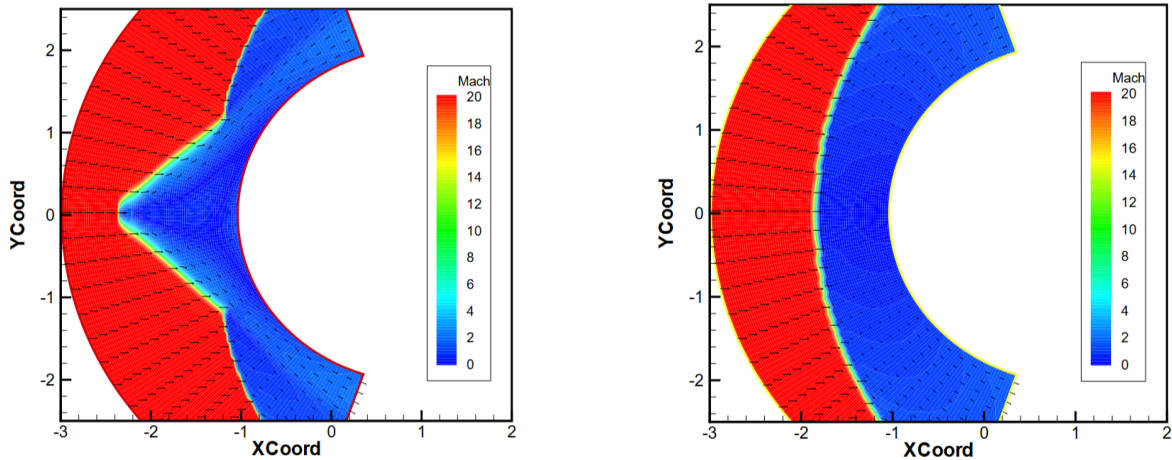


Figure 36: An illustration of the Carbuncle Phenomenon (left) compared to the stable solution for the same geometry (right). Figures from Ismail (2006).

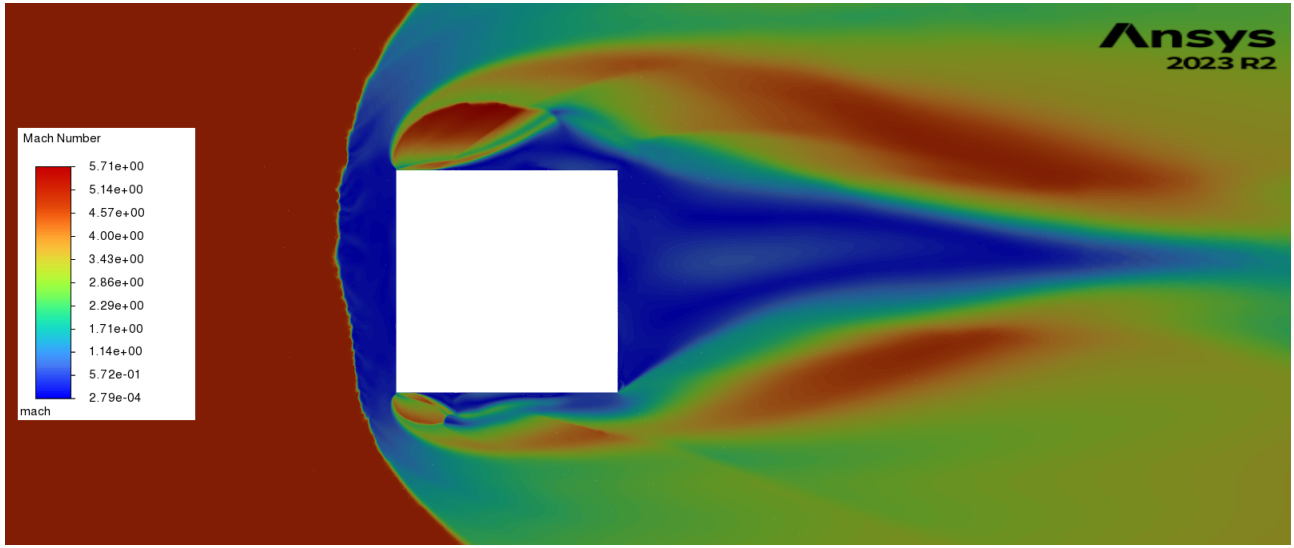


Figure 37: An instance of the carbuncle phenomenon. The plot shows contours of Mach number. It can be seen that the frontal shock behaves as if "punctured", and does not form a bow shape. It is also evident that this effect creates spurious asymmetries and nonphysical flow patterns after the shock.

for hypersonic simulations is the misalignment of the stencil with flow solutions. This effect can cause spurious vorticity and shock-wave deformations (a demonstration is shown in Figure 36, and an instance from our simulations is shown in Figure 37), and it is known as the Carbuncle Phenomenon [89]. The nature of this phenomenon is (notoriously) poorly understood, and several cures have been proposed [90, 91, 92]. We implemented the Advection Upstream Splitting Method (AUSM) implicit flux discretisation method with vector splitting and second-order spatial accuracy, which helps in preventing carbuncles. Gradients were computed following the Green-Gauss Cell-Based method. The simulations assume steady-state conditions (see 8.3.8). Convergence was judged on flow residuals falling below  $10^{-4}$  for  $\geq 50$  iterations, in addition to Mass Flow Imbalance ( $MFI := 100(\dot{m}_{in} - \dot{m}_{out})/\dot{m}_{in}$ ) falling below 2%. Future commercial simulations are to be run on a fixed-iteration basis.

### 8.3.6 Adaptive Mesh Refinement - Claudio Vestini

For our CubeSat simulation, we implement a simple square geometry of sidelength  $L = 0.2$  m into a large rectangular domain of dimensions  $5\text{ m} \times 10\text{ m}$ . The large domain size allows for the application of far-field boundary conditions, and the capturing of wake effects downstream of the CubeSat. We are, however, compromising for computational cost. For this reason, and as good general CFD practice, mesh cell sizes are adapted to be finer close to walls (and shock-waves, more in Section 8.3.9), and coarser in the far-field. In addition, the cell shape is adapted to capture the steep gradients of boundary layers: a prismatic inflation layer is adopted near the four walls, where prevalent gradients are aligned in the wall-normal direction; polyhedral (triangular for the 2D case) cells are chosen away from walls for the remaining bulk of the fluid domain (see Figure 39).

To capture the effect of shocks and expansions, the position of such flow features must be known *a priori*. The practice of Adaptive Mesh Refinement (AMR) consists of computing the rough position of high-gradient features using unrefined meshes at first, then increasing cell counts in those locations where the highest gradients are located. This is visually explained in Figure 38.

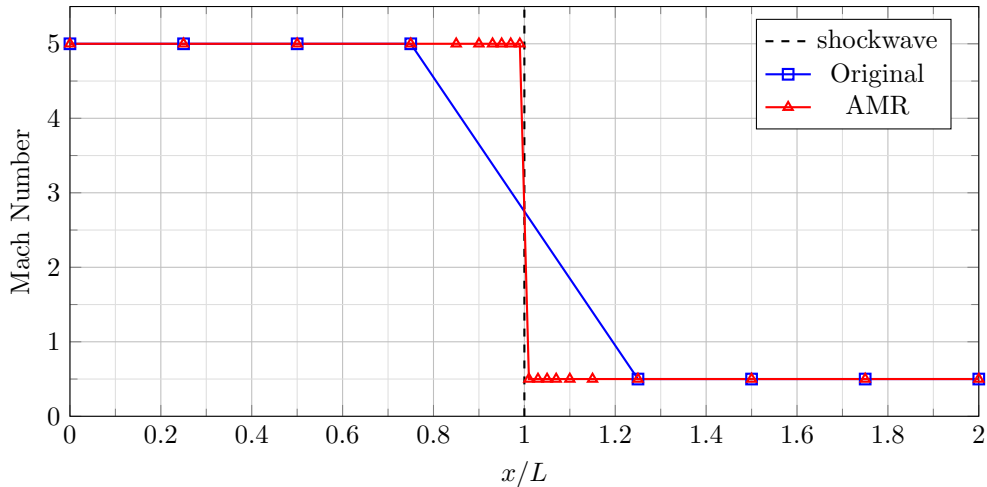


Figure 38: An idealised illustration of Adaptive Mesh Refinement for a normal shockwave at  $x/L = 1$ , with upstream Mach number of 5.0 and downstream Mach number of 0.5. The refined mesh (red line with triangle markers), with increased cell count near the high-gradient shock, provides a much better estimate of flow parameters.

### 8.3.7 Wall Treatment - Claudio Vestini

For high-speed external flows, turbulence modelling becomes critical due to the presence of shock–boundary layer interactions and laminar-to-turbulent transitions. In this study, particular attention was given to near-wall boundary layers, as their adequate resolution has a significant impact on temperature and heat flux distribution predictions. The dimensionless wall distance and velocity profile,  $y^+$  and  $u^+$ , respectively, are defined in terms of the friction velocity,  $u_\tau$ , as:

$$u_\tau := \sqrt{\frac{\tau_w}{\rho}}; \quad y^+ := \frac{\rho u_\tau y}{\mu}; \quad u^+ := \frac{u}{u_\tau} \quad (94)$$

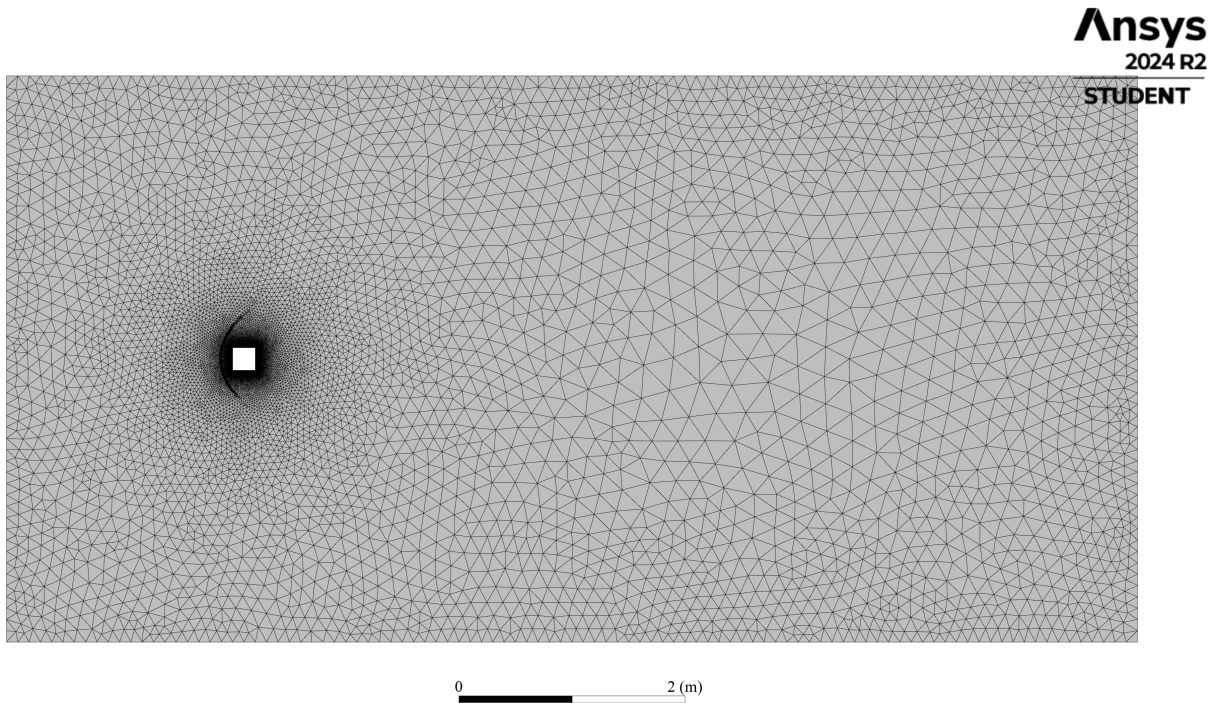


Figure 39: Domain Mesh for Run1. Fluid domain dimensions are  $5\text{ m} \times 10\text{ m}$ , and CubeSat dimensions are  $0.02\text{ m} \times 0.02\text{ m}$ . Mesh counts are  $6.08 \times 10^5$  cells,  $1.03 \times 10^6$  faces, and  $3.88 \times 10^5$  nodes. Simulations were run on an ANSYS Professional license, and plots were generated in Post through a Student license.

where  $y$  is the distance away from the wall,  $\mu$  is the dynamic viscosity,  $\rho$  is fluid density and  $\tau_w$  is the wall shear stress. In some CFD simulations involving turbulent boundary layers, it is a possible option to avoid simulating the boundary layer altogether. In this case, wall functions are used to bridge the near-wall region without fully resolving the viscous sublayer. For mesh designs relying on these standard wall functions, the first node should be placed within the logarithmic layer ( $30 < y^+ < 300$ ). On the other hand, enhanced wall treatment models<sup>8</sup> demand  $y^+ \lesssim 1$  to resolve the viscous sublayer [93]. This is the type of simulation we are running. Fluent automatically adjusts wall function applicability based on local  $y^+$  values and mesh density [88].

### 8.3.8 Boundary Conditions - Claudio Vestini

Given the nature of hypersonic atmospheric re-entry and our attitude control system, the CubeSat is expected to tumble throughout the mission at rates of  $\Omega \approx 1\text{ RPM}$  [**FIZZA**]. Since free-stream flow Mach numbers will be hypersonic for the entirety of the mission, the Strouhal number, defined as  $\text{St}_r := \frac{\Omega L}{U_\infty}$  will remain very low:  $\text{St} \lesssim 10^{-5}$ . Hence, we can assume the flow field to always be fully developed in a quasi-steady state<sup>9</sup>. Transients can, therefore, be neglected, and the flow can be studied for a specific value of Mach and incidence. Throughout our CubeSat mission, far-field air density and composition, Mach and Reynolds numbers, flow incidence, pressure, and temperature will all vary continuously. There is, consequently, a vast spectrum of boundary conditions to be considered for testing. For commercial missions, the critical conditions (i.e. those that give the greatest aerothermal loadings) often receive the highest level of scrutiny.

<sup>8</sup>Where the boundary layer is fully simulated

<sup>9</sup>Note that this assumption is very common for hypersonic re-entry simulations, as tumble rates are generally low compared to re-entry flow velocities.

The results presented in this report consider three sets of simulation conditions: Run 1, Run 2 and Run 3. Run 1 was designed to match the conditions of the Rees papers [85, 86, 87] at Mach 5 and zero incidence for validation purposes. The thermal wall boundary condition is a non-slip, isothermal wall condition with a uniform temperature of  $T_w = 300$  K. It is important to note that this condition is not physically realistic and does not accurately represent a realistic re-entry scenario. In practice, the flow is transient, and the wall temperature increases over time, approaching the adiabatic wall temperature. Additionally, the temperature distribution across the surface will not be uniform due to elevated heat flux at the corners. These discrepancies are typically addressed by reporting heat fluxes using the Stanton number, defined as  $\text{St} := \frac{q_w}{\rho U_\infty c_p (T_w - T_\infty)}$ . However, this approach fails to account for thermal conduction through the geometry, particularly near the corners and edges. To properly simulate this phenomenon, we would require an unsteady CFD simulation coupled with a material thermal response model, where, at each step, heat flux from the CFD solver is input into the thermal solver, which updates the wall temperature for the subsequent CFD time step. The level of complexity in this kind of simulation is beyond the scope of this 3YP report<sup>10</sup>. With this in mind, we note that the same non-slip isothermal boundary condition was also used by Rees, so the validation process remains unaffected.

Run 2 has the same conditions as Run 1, but at 45° incidence. Run 3 is aimed at simulating typical re-entry conditions at 50 km altitude [94], which is predicted to be the rough location of maximum aerothermal loading. This is common for re-entry capsules, such as SpaceX's Dragon [95]. For this run, the Mach number, pressure and temperature boundary conditions were chosen as  $M_\infty = 17$ ,  $P_\infty = 30\,000$  Pa and  $T_\infty = 250$  K [94]. The Fluent models were altered to include reacting Navier-Stokes equations (with 5-species air: N<sub>2</sub>, O<sub>2</sub>, NO, N, O), and temperature-dependent viscosity  $\mu$ . Wall boundary condition is constant heat flux, informed by the Stanton number results of Run 1 (see Section 8.3.10). Note that no validation data was available for cube geometries at these conditions, so the results presented for this run are to be considered with caution, and should be interpreted as indicative rather than definitive predictions. Future work should focus on populating a phase space of Mach versus  $\alpha$  to provide flow distributions for Mach values ranging from 25 to 5 and incidence angles ranging from 0° to 45°. The simulation conditions have been summarised in Table 7.

Parameter	Variable Name	Run 1	Run 2	Run 3
Mach Number	$M_\infty$	5	5	17
Velocity (m s <sup>-1</sup> )	$U_\infty$	1177	1177	5388
Angle of Attack (°)	$\alpha$	0	45	0
Static Pressure (Pa)	$P_\infty$	1584	1584	30000
Temperature (K)	$T_\infty$	138	1338	250
Reynolds Number	$Re_\infty$	72,581	72,581	25,170,985
Wall Thermal Condition	—	isothermal	isothermal	specified heat flux

Table 7: Summary of Boundary Conditions.

For a perfect gas, the relationship between the Mach number, Reynolds number, and Knudsen number is given

<sup>10</sup>This could be an interesting extension of the project into a 4YP. Since an inverse 1D heat conduction solver has already been developed (see Section 8.2.4), this would require the extension of the FTCS solver to two dimensions and a forward version of the heat equation (given the heat fluxes, compute the temperatures), as well as the coupling computational infrastructure required to merge the Python solver with the Fluent CFD simulation.

by equation (95):

$$\text{Kn} = \frac{M}{Re} \sqrt{\frac{\gamma\pi}{2}} \quad (95)$$

The regime of our simulations is therefore on the order of  $\text{Kn} \sim 10^{-4}$  for Runs 1 and 2, and  $\text{Kn} \sim 10^{-6}$  for Run 3, which lies within the range of the Continuum Model.

### 8.3.9 Mesh - Claudio Vestini

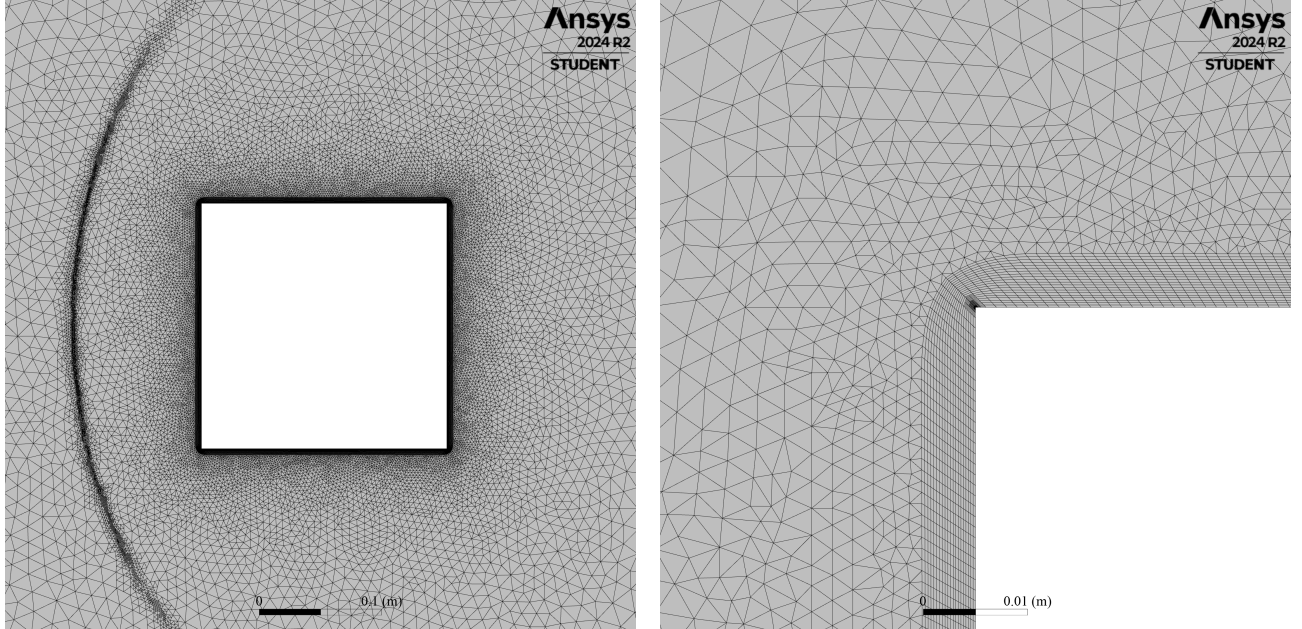


Figure 40: Detailed views of the CubeSat mesh for Run 1: Zoomed view (left) and corner detail (right).

The meshes for Runs 1, 2 and 3 were generated using the ANSYS Workbench Meshing program, with geometry imported from ANSYS Discovery. In all three cases, a prismatic inflation layer was created with  $\Delta y_{min} = 10^{-4}\text{m}$  for a total of 20 cells, and a moderate growth rate of 1.07 was selected (the boundary layer was entirely contained within this inflation layer). As a result, for all three runs, the value of  $y^+$  remained below 1 within all four viscous sublayers. Additionally, the maximum value of the first cell Reynolds number, defined as:

$$Re_c = \frac{\rho_c a_c \Delta z}{\mu_c} \quad (96)$$

where  $\rho_c, a_c, \mu_c$  are the local density, speed of sound, and viscosity of the fluid in the first cell, and  $\Delta z$  is the characteristic length scale of the cell (taken as the longest spatial dimension for structured meshes, or the cube root of cell volume for unstructured meshes), was recorded as 8.44. The first-cell Reynolds number serves as a standard criterion to ensure accurate prediction of surface heat flux, guaranteeing that flow gradients within the viscous boundary layer near the wall are properly resolved. Values of  $Re_c$  on the order of unity can reliably simulate heat transfer rates to the wall [96].

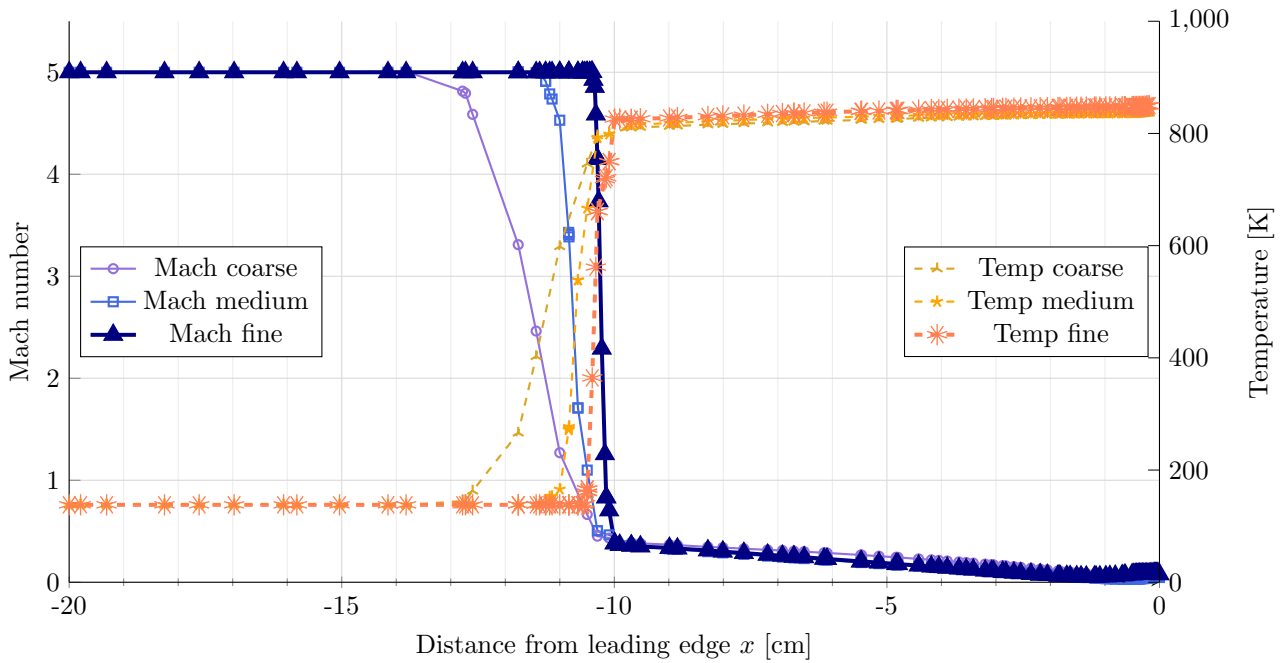


Figure 41: Mach number and static temperature profiles across the frontal bow shock on the stagnation streamline for different grid refinements. The final mesh refinement (fine) is shown with a thicker line width.

The meshes were also refined around the bow shock and expansions using an AMR routine with 4 meshes (coarse, medium, fine, and extra-fine) based on a Grid Convergence Index (GCI) defined as:

$$GCI_{ij} = \frac{S_F |\varepsilon_{ij}|}{r^p - 1}, \quad \varepsilon_{ij} = \phi_j - \phi_i, \quad i \in 1 : 3, \quad j = i + 1 \quad (97)$$

where the variable of interest  $\phi_i$  was selected as Mach number on the stagnation streamline just ahead of the bow shock,  $r = \Delta x_{coarse}/\Delta x_{fine} = 2$  is the refinement ratio,  $p$  is computed as  $p = \ln(\varepsilon_{jk}/\varepsilon_{ij})/\ln r$  (with  $k = j + 1$ ), and  $S_F = 1.25$  is a safety factor. A GCI of 0.037 was obtained beyond the second refinement (comparing an eight-fold versus sixteen-fold finer mesh), confirming mesh independence across the bow shock for  $i \geq 3$ . The refinement study for Run 1 is illustrated in Figure 41, and the finalised mesh is shown in Figures 39, 40. We note that a similar refinement process was implemented for Runs 2 and 3.

### 8.3.10 Results - Claudio Vestini

Numerical schlieren results for Runs 1 and 2 are shown in Figure 42, and relevant flow structures are labelled in Figure 43. These results show good agreement with the flow patterns described in Section 8.3.2. A bow shock (left) and a strong attached shock (right), as well as strong Prandtl-Meyer corner expansions, are clearly visible in Figure 42. As previously discussed, a weak compression wave appears in Run 1, which is also observed in [85]. This can be seen in Figure 42 (left). Upon close inspection, the reattachment shock is also visible in this figure on the left side of the top and bottom edges.

Owing to the presence of shocks, expansions, separations, and strong heat fluxes, the boundary layer around the square requires careful definition. Here, the boundary layer height  $\delta$  is taken as the point where the total

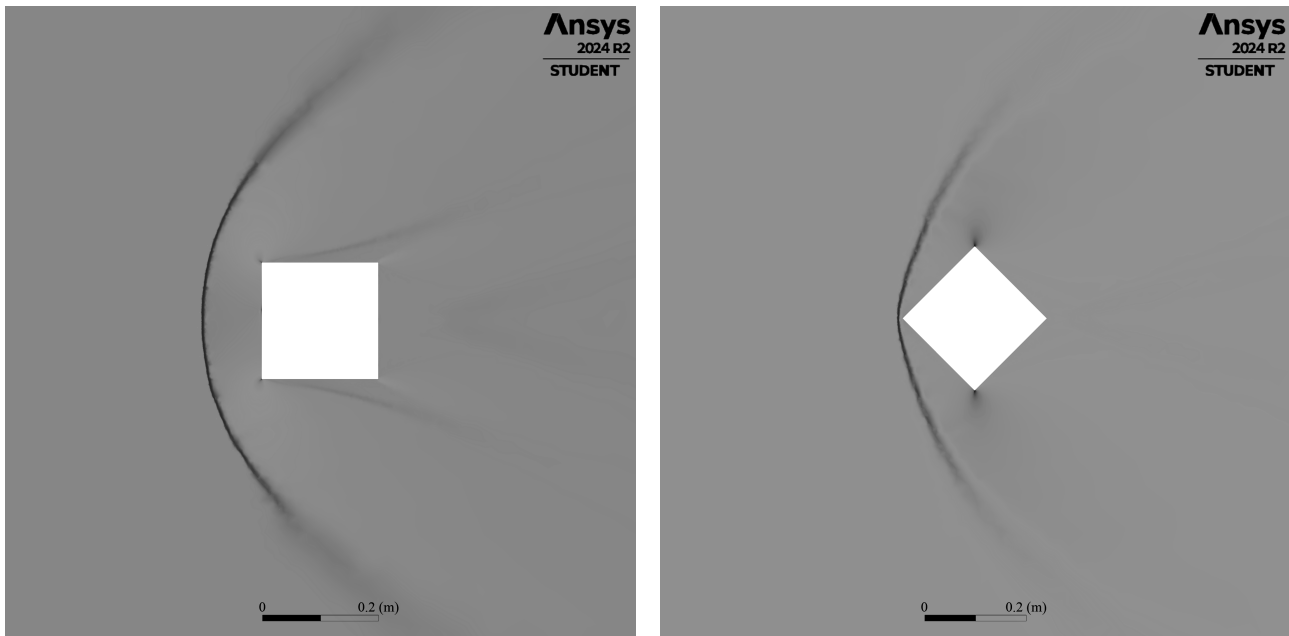


Figure 42: Schlieren (numerical) contours for Run 1 (left) and Run 2 (right). These flow distributions are a good qualitative match to Figure 34.

enthalpy  $H_0 = h + \frac{1}{2}|\mathbf{u}|^2$  recovers to the free-stream value  $H_{0,\infty}$ , thus capturing both thermal and kinetic viscous effects. The boundary layer thinning effect caused by the strong corner expansion is visible in Figure 43, and is consistent with [85]. This effect is what causes the sharp rises in heat flux to the wall, and consequently static temperature, which was shown experimentally in [87] and reported in Figure 35.

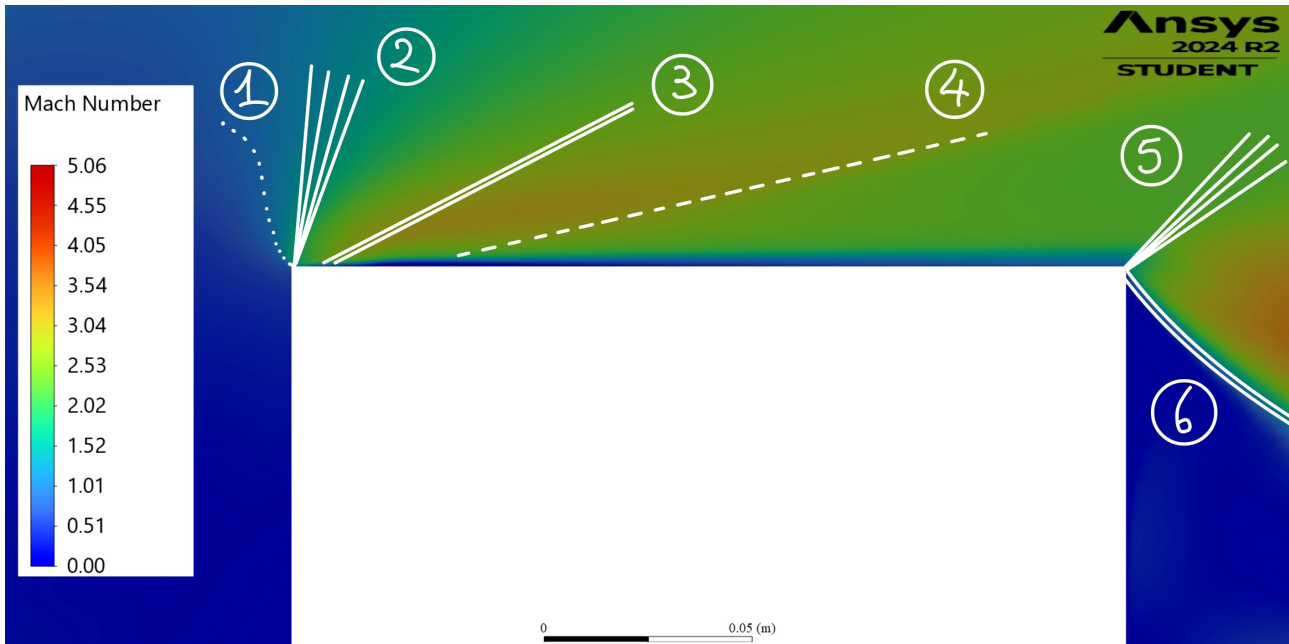


Figure 43: Detail of Mach number contours around the top half of the leading edge, top edge and top half of the leeward edge. Flow structures show the presence of: ① Sonic Line, ② Leading-Edge Expansion Fan, ③ Re-Attachment Shock, ④ Weak Compression Wave, ⑤ Trailing-Edge Expansion Fan, ⑥ Wake Shock. These are consistent with the results of *Seltner, Willemse, and Gühan (2019)* of Figure 34 (left).

Results for Mach number (with literature comparison for validation), static pressure and static temperature distribution contours for Run 1 are shown in Figures 44 and 45, respectively. A bow shock is found to form at

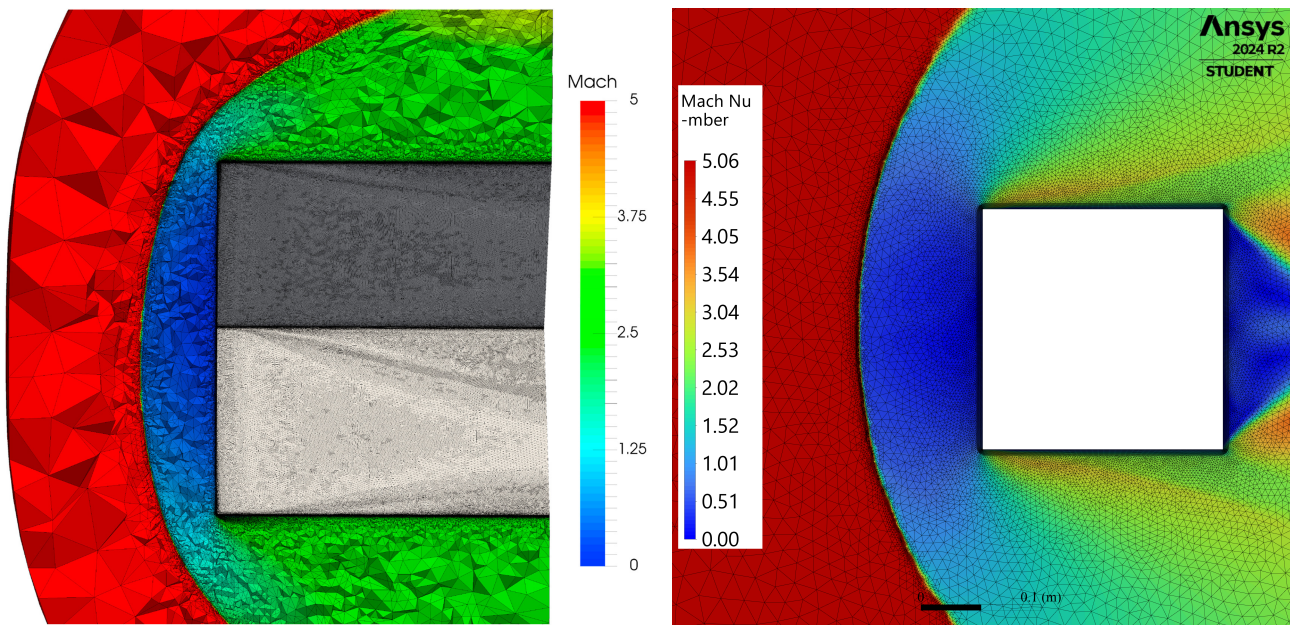


Figure 44: Comparison of Mach number contours between *Rees et al. (2021)* (left) and our Fluent Run 1 simulation (right). The results show good quantitative agreement.

10.6 cm ahead of the leading edge. The standoff distance for the bow shock in our simulation is greater than that of Rees, which is consistent with the Fluent simulation running at a higher Reynolds number.

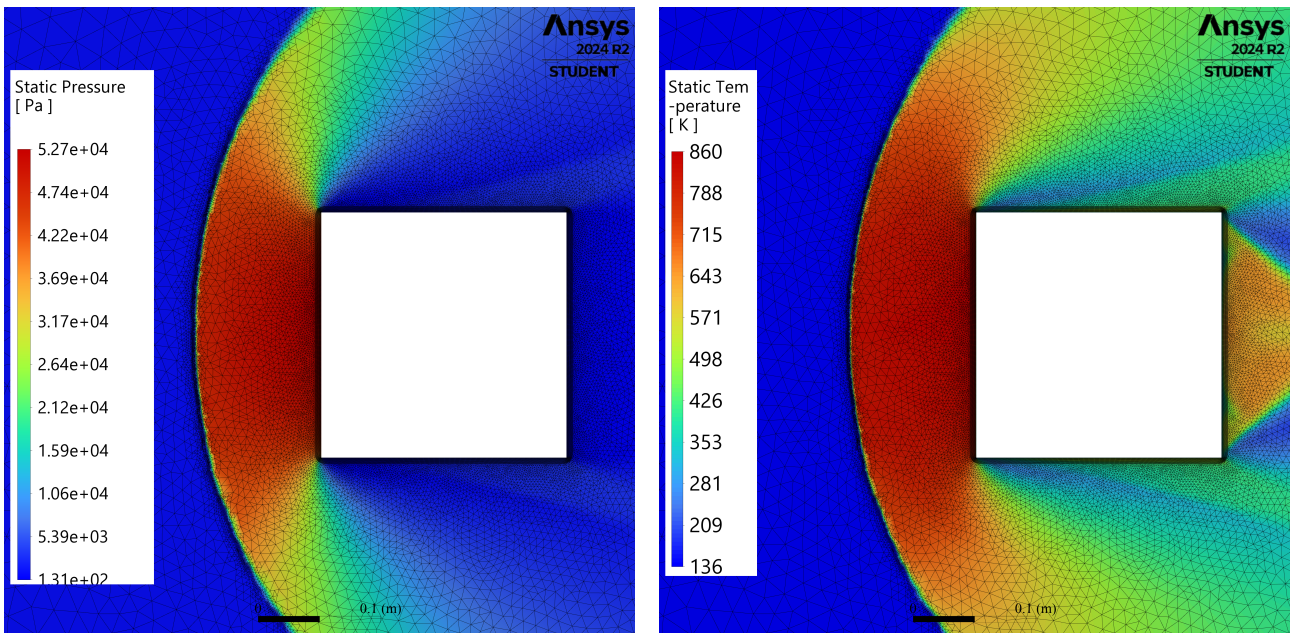


Figure 45: Run 1: static Pressure (left) and Temperature (right) distributions outputs of the CubeSat CFD simulation as contours of interpolated nodal values.

As shown in Figure 45 (left), in Run 1, static temperature is found to sharply rise above the far-field value behind the bow shock, resulting in temperatures of upwards of 860.41 K (this occurs near the corner expansion, which is consistent with the experimental data<sup>11</sup>). Flow static temperature rises to values of about 550 K in the wake, as shown in Figure 45 (right). We note that no analysis of the wake flow properties was provided in [85];

<sup>11</sup>Note that the isothermal nature of Run 1 means the walls are at 300 K, so this peak value a few cells away from the walls.

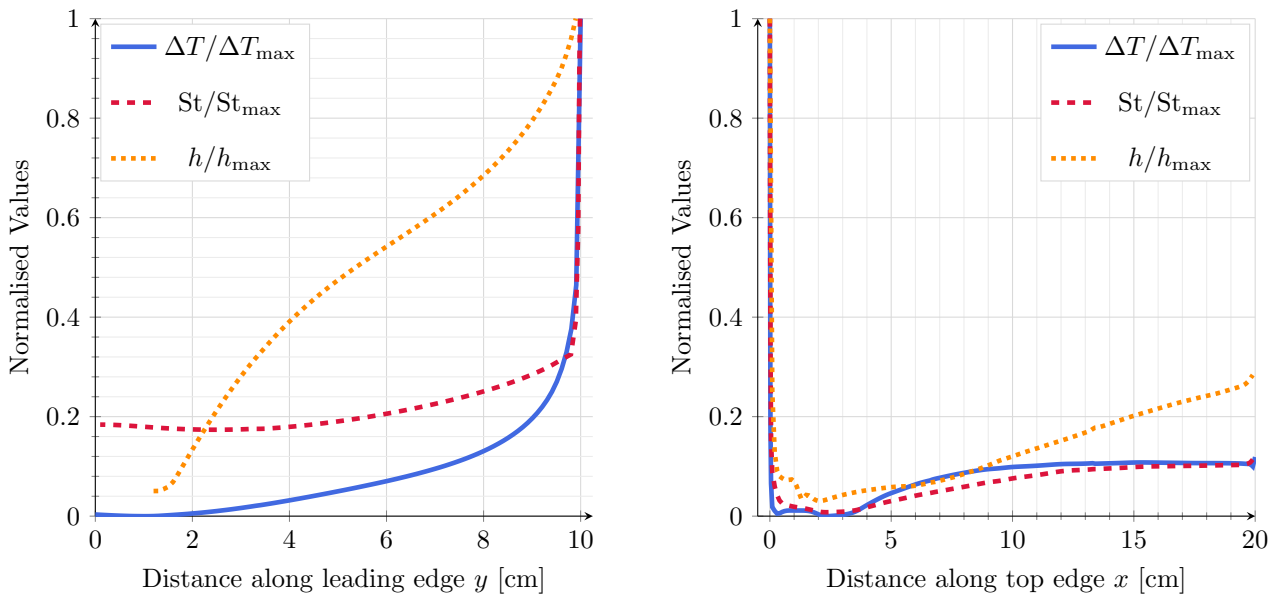


Figure 46: Normalised temperature increase above stagnation point temperature  $\Delta T$  (Run 3), normalised Stanton number  $St$  (Run 1), and normalised  $y^+$ -based heat transfer coefficient  $h$  (Run 1) along the top half of the leading edge (left); Normalised static temperature increase above minimum top-edge static temperature  $\Delta T$  (Run 3), normalised Stanton number  $St$  (Run 1), and normalised  $y^+$ -based heat transfer coefficient  $h$  (Run 1) along the top edge (right).

additionally, the wake was not included in the simulation of [87] (this can be seen in Figure 44 (left), where the picture displays the entire flow domain simulated). Due to this, the above analysis of wake distributions is tentative and kept brief. No further discussion of the wake is made within the rest of the report.

Concurrently, static pressure rises behind the shock, with a maximum value of 52.68 kPa at the stagnation point. A detailed examination reveals that pressure values drastically drop behind the first set of strong Prandtl-Meyer corner expansions to a value of 0.21 kPa. As the flow is processed by the re-attachment shock and compression wave, pressure rises to 2.36 kPa. As the flow recompresses, an adverse pressure gradient forms behind re-attachment location (pressure reaches 3.73 kPa just before the trailing edge), which is consistent with the findings of [85] section IV-C, in which it is stated: "the flow passes through the recompression wave and continues to compress until it expands over the top side of the square. The results suggest that the boundary layer has not recovered to its zero pressure gradient profile before expanding over the leeward surface of the square". Wake effects on pressure can be seen very faintly at the trailing edge in Figure 45 (left). The effects of the weak Mach wave on Mach number, static temperature and pressure can be seen clearly in Figure 44 (left) and 45 (left and right), respectively.

Figure 46 shows distributions of static temperature increase, Stanton number and heat transfer coefficients along the leading and top edges, respectively. The temperature increases  $\Delta T$  were obtained from Run 3 (with non-isothermal wall conditions), where static temperature at the stagnation point was found to be 4800 K. Compare this to an estimate from the ideal gas equation  $T_0 = T_\infty \left(1 + \frac{\gamma-1}{2} M_\infty^2\right)$ , which gives  $T_0 = 14700$  K for the conditions of Run 3. As described in Section 8.3.1, this is expected, as real gas phenomena such as O<sub>2</sub> molecular dissociation and temperature-dependent  $\gamma$  will result in much lower temperatures behind the bow

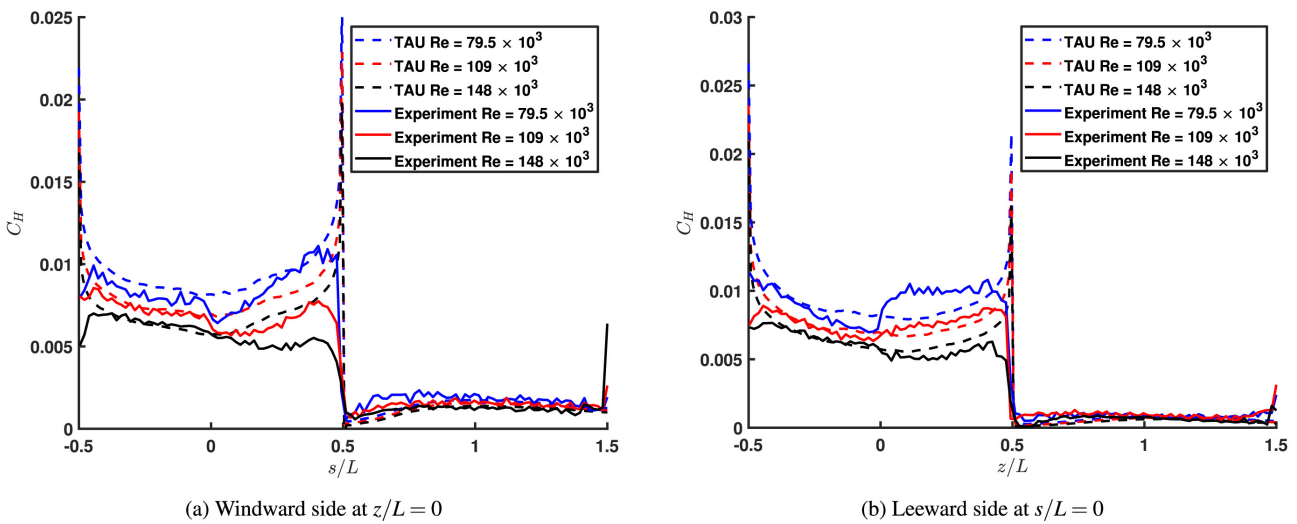


Figure 47: Stanton number distribution along the central cross section on the windward side (a) and leeward side (b) from both experimental and numerical sources. Experiments, simulations and figures by Rees et al. (2021).

shock. Verification through NASA's LAURA code (version 5.6) gave a much more likely estimate of 5100 K at stagnation. The maximum temperature increase (at the leading-edge corners) was found as  $\Delta T_{\max} = 850$  K (this is used as the normalisation value for both the (left) and (right) plots of Figure 46). The minimum static temperature value on the top edge, just before reattachment, was found to be 440 K.

For the Run 1 parameters, heat transfer coefficients were obtained as first cell,  $y^+$ -based values, and Stanton numbers were computed using the heat flux across the CubeSat's wall, and definition given in Section 8.3.8. The latter can be directly compared to the experimental and numerical results of [86, 87], shown in Figure 47<sup>12</sup>. The Stanton number distributions show good agreement with the Rees data, with stagnation-point values constituting about 20 % of the maximum, with a sharp increase near the corners. Stanton number drops across the strong corner expansions to a minimum of less than 1 % of the maximum, slowly increasing along the top edge to about 10 % near the leeward edge.

Figure 48 shows the wall-normal temperature distribution within the boundary layer along the top edge. These profiles closely follow the typical hypersonic boundary layer distribution, where static temperature rises above wall temperature, then decays to its free-stream value (see [72] chapter 1.3-C). The maximum temperature within the boundary layer is found to occur at  $x = 3$  cm away from the leading edge.

These results informed the design of an ablative heat shield to ensure survival through the upper atmosphere, as well as sufficient internal heating to ignite the thermite masses (discussed further in Section 8.4).

#### 8.4 Thermite for Demise (T4D) - Claudio Vestini

Design-for-Demise (D4D) is a rapidly emerging field of study within aerospace engineering, which focuses on intentionally designing spacecraft to minimise the chance of ground impact through atmospheric re-entry. Within

<sup>12</sup>Although the numerical and experimental results for these papers were run at 5 ° incidence, the authors reported that the small angle of attack had little effect on the results (and no other data was found as of the writing of these results).

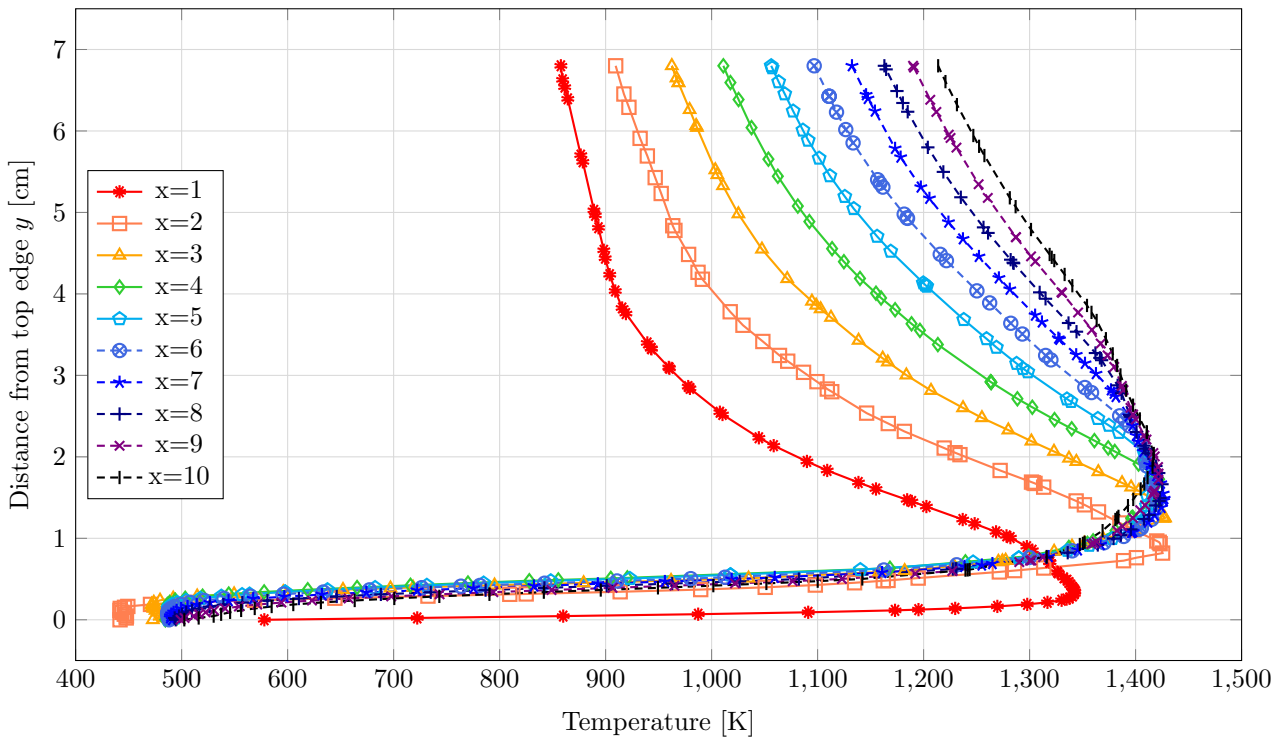


Figure 48: Run 3: temperature profiles within the viscous boundary layer at different streamwise positions ( $x$ -values, in cm) along the first half of the top edge of the CubeSat. Surface temperature is found to lie between 400 K and 600 K, with the highest surface temperature just after the frontal corner Prantl-Meyer expansion.

the spectrum of D4D methodologies, one particularly innovative approach is Thermite-for-Demise (T4D), which has been the subject of recent investigations at the *Politecnico di Milano* [97]. This strategy involves incorporating an additional source of enthalpy on board the spacecraft in the form of a thermite pyrotechnic charge, which is designed to passively ignite during the re-entry process. Thermites are a subset of energetic materials, typically composed of a metal and a metal oxide in powder form, which undergo an exothermic oxidation-reduction reaction upon ignition, releasing a significant amount of heat. These materials are attractive for space applications due to their high energy density and relative stability, as well as the possibility of selecting formulations that are relatively insensitive to external stimuli and non-toxic. Furthermore, the ignition temperature of thermites can be altered through formulation and processing techniques such as mechanical activation [98], where the powder is milled to alter its shape, granulometry, and surface finishing, resulting in tailored and predictable ignition characteristics. The additional heat released by the ignited thermite can aid the spacecraft in completing its demise by promoting ablation of robust components that might otherwise survive re-entry. This extra heat source can be strategically placed in the structural voids of particularly resilient components to specifically target their demise. Furthermore, the action of thermites can be employed to induce controlled fragmentation of the spacecraft, weakening structural joints and thereby increasing the overall surface area exposed to the intense aerothermal heating encountered during re-entry.

The Politecnico team conducted experiments to quantify the heat transfer efficiency between an ignited thermite powder and its confining vessel. In [99], an Al+Fe<sub>2</sub>O<sub>3</sub> thermite mixture was confined in a cylindrical steel vessel and heated externally. The average heat transfer efficiency was found to be around 60% of the theoretical

heat release. This efficiency was found to be significantly influenced by the geometry of the vessel: confined configurations eliminated convective and radiative losses, leading to higher efficiency compared to unconfined setups. The team also developed a numerical model called TRANSIT (TRANsatmosferic SImulation Tool), to simulate the re-entry process with the inclusion of a thermite charge [97]. TRANSIT is an object-oriented tool that considers flight dynamics, aerothermodynamics, and heat transfer processes. It has been verified [97] against commercial software packages like SAM and SCARAB. TRANSIT allows for the preliminary sizing of the thermite charge by considering factors such as the mass ratio between the thermite and the spacecraft, the material reactivity, the heat release profile, and the total enthalpy release. Genetic algorithms are employed to optimise these parameters to ensure complete demise while minimising the required thermite mass [97].

For our project, the CubeSat undergoes atmospheric re-entry to evaluate the performance of ablative materials for heat shield purposes. The presence of an ablative heat shield, while crucial for protecting the payload and enabling quantitative testing, will delay the complete disintegration of the CubeSat structure during the uncontrolled re-entry, thereby increasing the ground casualty risk. Consequently, the implementation of T4D presents a compelling strategy to ensure complete demise upon re-entry for our mission. To minimise the probability of ground impact, we integrate a T4D system within the existing assembly to provide a localised and intense internal heat source that works in conjunction with the external aerothermal heating. No electronics are required for ignition, as the heat loads are expected to be sufficient to activate the charges. Thermite charges are embedded within the most robust internal components, such as the electronics mounting structures, the three reaction wheel motors, and other dense mechanical elements expected to withstand the initial re-entry heating. Upon activation, these charges deliver intense, localised heating directly to the core of these components, promoting rapid melting and structural failure. Additionally, thermite charges are positioned at key structural joints within the CubeSat frame. This arrangement is designed to induce targeted weakening and controlled fragmentation of the structure during re-entry, thereby increasing the surface area-to-mass ratio of the debris and enhancing the likelihood of complete ablation in the upper atmosphere. To address the risk of residual protection from the ablative layer, the remaining thermite charges are located adjacent to the inner surface of the heat shield. These charges are configured to activate during the later stages of re-entry, breaching any remaining ablative material and exposing the underlying structure to direct aerothermal heating. This comprehensive T4D implementation ensures that the CubeSat does not survive re-entry in large fragments, thereby reducing the risk of ground casualties and fully aligning with current best practice in space debris mitigation.

## 9 Costs

## 10 Project Risks

## 11 Conclusion

## References

- [1] Lorenzo Casalino and Andrea Forestieri. “Approximate optimal LEO transfers with J2 perturbation and dragsail”. In: *Acta Astronautica* 192 (Mar. 2022), pp. 379–389. ISSN: 0094-5765. DOI: 10.1016/J.ACTAAstro.2021.12.006.
- [2] George P. Sutton and Oscar Biblarz. *Rocket Propulsion Elements*. 7th. Hoboken, NJ: Wiley, 2017.
- [3] *Orbits: the elliptical orbit — Rip’s Applied Mathematics Blog*. URL: <https://rip94550.wordpress.com/2010/06/14/orbits-the-elliptical-orbit/>.
- [4] Miguel C N Fiolhais et al. “Orbital decay in the classroom Orbital decay in the classroom Orbital decay in the classroom”. In: (). URL: <https://academicworks.cuny.edu>.
- [5] *Solar Cycle Progression — NOAA / NWS Space Weather Prediction Center*. URL: <https://www.swpc.noaa.gov/products/solar-cycle-progression>.
- [6] *Geomagnetic Indices — National Centers for Environmental Information (NCEI)*. URL: <https://www.ncei.noaa.gov/products/geomagnetic-indices>.
- [7] Australian Space Weather Agency. “Satellite Orbital and Decay Calculations”. In: (). URL: [www.ips.gov.au](http://www.ips.gov.au).
- [8] *Earth Atmosphere Model - Metric Units*. URL: <https://www.grc.nasa.gov/www/k-12/airplane/atmosmet.html>.
- [9] David A. Vallado and David Finkleman. “A Critical Assessment of Satellite Drag and Atmospheric Density Modeling”. In: *AIAA/AAS Astrodynamics Specialist Conference and Exhibit*. AIAA, 2008.
- [10] L. Zheng and X. Zhang. “Numerical Methods”. In: *Modeling and Analysis of Modern Fluid Problems* (2017), pp. 361–455. DOI: 10.1016/B978-0-12-811753-8.00008-6. URL: <https://linkinghub.elsevier.com/retrieve/pii/B9780128117538000086>.
- [11] *ERS-2 reentry – live updates – Rocket Science*. URL: <https://blogs.esa.int/rocketscience/2024/02/05/ers-2-reentry-live-updates/>.
- [12] *General Mission Analysis Tool (GMAT) v.R2016a(GSC-17177-1) — NASA Software Catalog*. URL: <https://software.nasa.gov/software/GSC-17177-1>.
- [13] *Ansys STK — Digital Mission Engineering Software*. URL: <https://www.ansys.com/en-gb/products/missions/ansys-stk>.

- [14] *Space Environment Statistics · Space Debris User Portal*. URL: <https://sdup.esoc.esa.int/dicosweb/statistics>.
- [15] Newcastle University. “The Poisson Distribution 37.3”. In: ().
- [16] Kaman Sciences Corporation. “On-Orbit Collision Hazard Analysis in Low Earth Orbit Using the Poisson Probability Distribution (Version 1.0)”. In: (Aug. 1992). DOI: 10.21949/1402715. URL: <https://rosap.nt1.bts.gov/view/dot/12528>.
- [17] “Orbital Debris Management Risk Mitigation”. In: (). URL: [www.nasa.gov](http://www.nasa.gov).
- [18] “Orbital Debris Quarterly News A publication of The NASA Orbital Debris Program Office”. In: (2009). URL: [www.orbitaldebris.jsc.nasa.gov](http://www.orbitaldebris.jsc.nasa.gov).
- [19] *Collision Velocity in LEO*. URL: <https://www.spaceacademy.net.au/watch/debris/collvel.htm>.
- [20] Mingyang Mao et al. “The propagation characteristics of low frequency radio waves in magnetized hypersonic plasma sheaths”. In: *AIP Advances* 13.095019 (2023). Published Online: 20 September 2023. DOI: 10.1063/5.0163507. URL: <https://doi.org/10.1063/5.0163507>.
- [21] Ryan P. Starkey, Mark J. Lewis, and Charles H. Jones. “Plasma Sheath Characterization for Telemetry in Hypersonic Flight”. In: *International Telemetering Conference Proceedings*. International Foundation for Telemetering, 2003. URL: <http://hdl.handle.net/10150/606733>.
- [22] Tadatoshi Takahashi and Hiroshi Oya. “Satellite Wake Structure Probe Observed Installed on TAIYO”. In: *Science Reports of the Tohoku University, Series 5 (Geophysics)* 27.3-4 (1981). Received January 24, 1981, pp. 111–123.
- [23] Yusuke Takahashi, Kazuhiko Yamada, and Takashi Abe. “Prediction Performance of Blackout and Plasma Attenuation in Atmospheric Reentry Demonstrator Mission”. In: *Journal of Spacecraft and Rockets* (2014). DOI: 10.2514/1.A32880.
- [24] Wei Guo et al. “Polarization Characteristics Distortion for L-Band Fully Polarimetric Radar Subject to Magnetized Plasma Sheath”. In: *Remote Sensing* (2024). DOI: 10.3390/rs16122061.
- [25] Isil Sakraker et al. “QARMAN: An Atmospheric Entry Experiment on CubeSat Platform”. In: *8th European Symposium on Aerothermodynamics for Space Vehicles*. 2015.
- [26] MathWorks. *Link Budget*. 2025. URL: <https://uk.mathworks.com/discovery/link-budget.html>.
- [27] Vincent J. Riot, Lance M. Simms, and Darrell Carter. “Lessons Learned Using Iridium to Communicate with a CubeSat in Low Earth Orbit”. In: *Journal of Small Satellites (JoSS)* 10.1 (2021). Peer-reviewed article, pp. 995–1006. URL: [www.jossonline.com](http://www.jossonline.com).
- [28] Julien’s Lab. *Iridium Satellites Live Map*. 2025. URL: <https://www.iridiumwhere.com/>.

- [29] Peter Delos, Bob Broughton, and Jon Kraft. "Phased Array Antenna Patterns—Part 1: Linear Array Beam Characteristics and Array Factor". In: *Analog Dialogue* (2020). URL: <https://www.analog.com/media/en/analog-dialogue/volume-54/number-2/phased-array-antenna-patterns-part-1-linear-array-beam-characteristics-and-array-factor.pdf>.
- [30] Kirt Blattenberger. *Cascaded Noise Figure & Noise Temperature Calculation Equation Formula*. 2025. URL: <https://www.rfcafe.com/references/electrical/noise-figure.htm>.
- [31] All About Circuits. *Noise Figure and Noise Temperature Calculator*. <https://www.allaboutcircuits.com/tools/noise-figure-noise-temperature-calculator/>. 2025.
- [32] Thomas A. Milligan. *Modern Antenna Design*. 2nd Edition. IEEE Press, 2005, p. 32.
- [33] Jim Karki. *Understanding Operational Amplifier Specifications (Rev. B)*. Tech. rep. Texas Instruments, 2018. URL: <https://www.ti.com/lit/an/sloa011b/sloa011b.pdf>.
- [34] Dr. George Vekinis. *ReWiG: A Resistive Wire Mesh TPS recession sensor*. Technical Report. ESA Contract 4000111843/14/NL/SC, ITI Phase A Study. European Space Agency (ESA), 2015. URL: [https://nebula.esa.int/sites/default/files/neb\\_tec\\_study/2335/public/23690\\_FP.pdf](https://nebula.esa.int/sites/default/files/neb_tec_study/2335/public/23690_FP.pdf).
- [35] Nondestructive Evaluation Techniques. *Electrical Conductivity and Resistivity for Nickel and Nickel Alloys*. 2025. URL: [https://www.nde-ed.org/NDETechniques/EddyCurrent/ET\\_Tables/ET\\_matlprop\\_Nickel.xhtml](https://www.nde-ed.org/NDETechniques/EddyCurrent/ET_Tables/ET_matlprop_Nickel.xhtml).
- [36] *CuSP Propulsion System — VACCO Industries*. URL: <https://cubesat-propulsion.com/cusp-propulsion-system/>.
- [37] *Ideal Rocket Equation — Glenn Research Center — NASA*. URL: <https://www1.grc.nasa.gov/beginners-guide-to-aeronautics/ideal-rocket-equation/>.
- [38] Gaoge Hu et al. "Robust Unscented Kalman Filtering with Measurement Error Detection for Tightly Coupled INS/GNSS Integration in Hypersonic Vehicle Navigation". In: *IEEE Access* 7 (2019), pp. 151409–151421. ISSN: 21693536. DOI: 10.1109/ACCESS.2019.2948317. URL: [https://www.researchgate.net/publication/336662296\\_Robust\\_Unscented\\_Kalman\\_Filtering\\_With\\_Measurement\\_Error\\_Detection\\_for\\_Tightly\\_Coupled\\_INSGNSS\\_Integration\\_in\\_Hypersonic\\_Vehicle\\_Navigation](https://www.researchgate.net/publication/336662296_Robust_Unscented_Kalman_Filtering_With_Measurement_Error_Detection_for_Tightly_Coupled_INSGNSS_Integration_in_Hypersonic_Vehicle_Navigation).
- [39] *What is Sensor Fusion? — Dewesoft*. URL: <https://dewesoft.com/blog/what-is-sensor-fusion>.
- [40] Richard F. Tinder. *Relativistic Flight Mechanics and Space Travel: A Primer for Students, Engineers and Scientists*. Extract of page 33. Morgan & Claypool Publishers, 2007, p. 33. ISBN: 978-1-59829-130-8.
- [41] *Gyroscope - SparkFun Learn*. URL: <https://learn.sparkfun.com/tutorials/gyroscope/all>.
- [42] Antonis Papachristodoulou. *B15 Optimal Control: Kalman Filtering*. Lecture notes. Accessed: 28 March 2025. 2024.

- [43] Vu Thi Bich Quyen et al. “Kalman Filter Based Sensor Fusion for Altitude Estimation of Aerial Vehicle You may also like A modified penalty function method for treating multi freedom constraints in finite element analysis of frames Kalman Filter Based Sensor Fusion for Altitude Estimation of Aerial Vehicle”. In: (). DOI: 10.1088/1757-899X/853/1/012034.
- [44] Håvard Fjaer Grip et al. “Attitude Estimation Using Biased Gyro and Vector Measurements With Time-Varying Reference Vectors”. In: () .
- [45] Mangal Kothari. “Attitude Representation and Transformation Matrices”. In: () .
- [46] *Using the Accelerometer – HUSSTECH*. URL: <http://husstechlabs.com/projects/atb1/using-the-accelerometer/>.
- [47] T. Ozyagcilar. *Implementing a Tilt-Compensated eCompass using Accelerometer and Magnetometer Sensors*. Tech. rep. Rev. 4.0. Freescale Semiconductor, 2015.
- [48] Wei Tech Ang et al. “Physical Model of a MEMS Accelerometer for Low-g Motion Tracking Applications”. In: (2004). URL: [www.analog.com](http://www.analog.com).
- [49] *AvaSpec-Mini2048CL - Avantes*. URL: <https://www.avantes.com/products/spectrometers/compactline/avantes-spectrometer-mini-2048cl/>.
- [50] *Multi-Furcated Fiber-Optic Cables - Avantes*. URL: <https://www.avantes.com/products/fiber-optics/optical-fibers/multi-furcated-fiber-optic-cables/>.
- [51] *LED and Solid State Lighting Measurement*. URL: <https://www.azom.com/article.aspx?ArticleID=11889>.
- [52] *Cosine Correctors - Avantes*. URL: <https://www.avantes.com/products/fiber-optics/fiber-optic-accessories/cosine-correctors/>.
- [53] Ger Loop Avantes. “INTENSITY CALIBRATIONS IN SPECTROSCOPY AND RADIOMETRY Content”. In: () .
- [54] “Integrating Sphere Measurement Part I: Basics”. In: (2014).
- [55] S. Shukla et al. “Inverse-catalyst-effect observed for nanocrystalline-doped tin oxide sensor at lower operating temperatures”. In: *Sensors and Actuators B: Chemical* 104 (2 Jan. 2005), pp. 223–231. ISSN: 0925-4005. DOI: 10.1016/J.SNB.2004.05.008.
- [56] “Atomic Spectra Database — NIST”. In: (). DOI: 10.18434/T4W30F. URL: <https://www.nist.gov/pml/atomic-spectra-database>.
- [57] York University. “Boltzmann distribution in a nutshell”. In: () .
- [58] A. M. Howatson, P. G. Lund, and J. D. Todd. *Engineering Tables and Data*. University of Oxford, 2009.
- [59] Robert C. Hilborn. “Einstein coefficients, cross sections, f values, dipole moments, and all that”. In: *American Journal of Physics* 50 (11 Nov. 1982), pp. 982–986. ISSN: 0002-9505. DOI: 10.1119/1.12937.

- [60] Jonathan M. Burt and Iain D. Boyd. “High Altitude Plume Simulations for a Solid Propellant Rocket”. In: <https://doi.org/10.2514/1.30129> 45 (12 May 2012), pp. 2872–2884. ISSN: 00011452. DOI: 10.2514/1.30129. URL: <https://arc.aiaa.org/doi/10.2514/1.30129>.
- [61] NanoAvionics. *How Many Satellites are in Space?* Accessed: 2025-04-20. 2023. URL: <https://nanoavionics.com/blog/how-many-satellites-are-in-space/>.
- [62] J.-J. Dordain. *ESA/ADMIN/IPOL(2014)2 - Space Debris Mitigation for Agency Projects*. Tech. rep. ESA/ADMIN/IPOL(2014)2. Administrative Instruction of the ESA Director General, entered into force on 28 March 2014. Paris, France: European Space Agency, 2014.
- [63] AA. VV. *ESA Space Debris Mitigation Requirements*. Tech. rep. ESSB-ST-U-007. European Space Agency, 2023.
- [64] AA. VV. *IADC Space Debris Mitigation Guidelines*. 2020.
- [65] AA. VV. *ESA's Annual Space Environment Report*. Darmstadt, Germany, 2022.
- [66] Donald J. Kessler and Burton G. Cour-Palais. “COLLISION FREQUENCY OF ARTIFICIAL SATELLITES: THE CREATION OF A DEBRIS BELT.” In: *J Geophys Res* 83 (A6 1978), pp. 2637–2646. ISSN: 0148-0227. DOI: 10.1029/JA083iA06p02637.
- [67] J. Dobarco-Otero et al. “The Object Reentry Survival Analysis Tool (ORSAT) Version 6.0 and Its Application to Spacecraft Entry”. In: *56th International Astronautical Congress*. Fukuoka, Japan, 2005.
- [68] C. Martin et al. *DRAMA Final Report*. Tech. rep. European Space Agency, 2005.
- [69] G. Koppenwallner et al. “SCARAB - A Multidisciplinary Code for Destruction Analysis of Spacecraft During Re-Entry”. In: *5th European Symposium on Aerothermodynamics for Space Vehicles*. Cologne, Germany, 2005.
- [70] P. M. Mehta et al. “An Open-Source Hypersonic Aerodynamic and Aerothermodynamic Modeling Tool”. In: *8th European Symposium on Aerothermodynamics for Space Vehicles*. 2015.
- [71] J. Annaloro et al. “Elaboration of a New Spacecraft-Oriented Tool: Pampero”. In: *8th European Symposium on Aerothermodynamics for Space Vehicles*. 2015.
- [72] J.D. Anderson. *Hypersonic and High-temperature Gas Dynamics*. AIAA education series. American Institute of Aeronautics and Astronautics, 2006. ISBN: 9781563477805. URL: <https://books.google.com.sg/books?id=UgWmQgAACAAJ>.
- [73] Augustin-Louis Cauchy. “Note sur divers théorèmes relatifs à la rectification des courbes et à la quadrature des surfaces”. French. In: *Comptes Rendus de l'Académie des Sciences* 13 (1841), pp. 1060–1065.
- [74] 3Blue1Brown. *A tale of two problem solvers — Average cube shadow area*. Accessed: 2025-03-24. 2021. URL: <https://www.youtube.com/watch?v=ltLUadnCyi0>.

- [75] Insoo Jun et al. “A review on radiation environment pathways to impacts: Radiation effects, relevant empirical environment models, and future needs”. In: *Advances in Space Research* (2024). ISSN: 0273-1177. DOI: 10.1016/j.asr.2024.03.029. URL: <https://www.sciencedirect.com/science/article/pii/S0273117724003296>.
- [76] National Aeronautics and Space Administration. *LEO Satellite Illumination Analysis Report*. Technical Report NAS-2024-LEO-001. 2024. URL: <https://ntrs.nasa.gov/citations/20240001234> (visited on 03/24/2024).
- [77] Gustav Kirchhoff. “Über den Zusammenhang zwischen Emission und Absorption von Licht und Wärme”. In: *Monatsberichte der Königlich Preussischen Akademie der Wissenschaften zu Berlin* (1860), pp. 783–787.
- [78] Luca Di Mare. “Notes on Discretisation Schemes for CFD”. Unpublished lecture notes. Course notes for Computational Fluid Dynamics (CFD) Coursework Module, University of Oxford. 2025.
- [79] Donald M. Kuehn. “Experimental and theoretical pressures on blunt cylinders for equilibrium and nonequilibrium air at hypersonic speeds”. In: *NASA Technical Report R-117* (1963).
- [80] Daniel F Potter. *Modelling of radiating shock layers for atmospheric entry at Earth and Mars*. 2011.
- [81] M. Knudsen. “Die Gesetze der Molekularströmung und der inneren Reibungsströmung der Gase durch Röhren”. In: *Annalen der Physik* 333.1 (1909), pp. 75–130. DOI: 10.1002/andp.19093330102.
- [82] Raphael Marschall et al. *Cometary Comae-Surface Links: The Physics of Gas and Dust from the Surface to a Spacecraft*. Dec. 2020. DOI: 10.1007/s11214-020-00744-0.
- [83] G. A. Bird. *Molecular Gas Dynamics and the Direct Simulation of Gas Flows*. Vol. 42. The Oxford Engineering Science Series. Oxford: Clarendon Press, 1994. ISBN: 978-0-19-856195-8.
- [84] Patrick M. Seltner, Sebastian Willems, and Ali Gülan. “Aerodynamic coefficients of free-flying cubes in hypersonic flowfield”. In: *Journal of Spacecraft and Rockets* 56 (6 2019), pp. 1725–1734. ISSN: 15336794. DOI: 10.2514/1.A34345.
- [85] Thomas W. Rees, Paul J.K. Bruce, and James A. Merrifield. “The effect of reynolds number on the hypersonic flow around faceted shapes”. In: *22nd AIAA International Space Planes and Hypersonics Systems and Technologies Conference*. American Institute of Aeronautics and Astronautics Inc, AIAA, 2018. ISBN: 9781624105777. DOI: 10.2514/6.2018-5197.
- [86] Thomas W. Rees et al. “Experimental characterization of the hypersonic flow around a cuboid”. In: *Experiments in Fluids* 61 (7 July 2020). ISSN: 14321114. DOI: 10.1007/s00348-020-02975-x.
- [87] Thomas W. Rees et al. “Numerical and experimental studies of the hypersonic flow around a cube at incidence”. In: *Acta Astronautica* 183 (June 2021), pp. 75–88. ISSN: 00945765. DOI: 10.1016/j.actaastro.2021.02.033.
- [88] David Bacci. *B19 Nozzle Flow Lab Notes: Introduction to CFD Best Practices*. Lab notes for B19 lab at the University of Oxford. 2025.

- [89] Farzad Ismail. *TOWARD A RELIABLE PREDICTION OF SHOCKS IN HYPERSONIC FLOW: RESOLVING CARBUNCLES WITH ENTROPY AND VORTICITY CONTROL*. 2006.
- [90] David I. Ketcheson and Manuel Quezada de Luna. “Numerical simulation and entropy dissipative cure of the carbuncle instability for the shallow water circular hydraulic jump”. In: *International Journal for Numerical Methods in Fluids* 93.7 (2021), pp. 2250–2267. DOI: 10.1002/fld.5070.
- [91] Simon Sangeeth and J. C. Mandal. “A cure for numerical shock instability in HLLC Riemann solver using antidiiffusion control”. In: *Computers & Fluids* 173 (2018), pp. 59–76. DOI: 10.1016/j.compfluid.2018.07.029.
- [92] J. M. Powers, J. Bruns, and A. Jemcov. “Physical Diffusion Cures the Carbuncle Phenomenon”. In: *53rd AIAA Aerospace Sciences Meeting*. American Institute of Aeronautics and Astronautics. Kissimmee, Florida, 2015.
- [93] David C. Wilcox. *Turbulence Modeling for CFD*. 2nd. La Cañada Flintridge, CA, USA: DCW Industries, 1994.
- [94] ANSYS Inc. *Reentry Capsule Analysis Using ANSYS Fluent*. Accessed: 2025-04-07. 2025. URL: [https://ansyshelp.ansys.com/Views/Secured/corp/v242/en/flu\\_tg/flu\\_tg\\_reentry\\_capsule.html](https://ansyshelp.ansys.com/Views/Secured/corp/v242/en/flu_tg/flu_tg_reentry_capsule.html).
- [95] Loretta Trevino. “SpaceX Dragon Re-Entry Vehicle: Aerodynamics and Aerothermodynamics with Application to Base Heat-Shield Design”. In: *6th International Planetary Probe Workshop*. Discusses computational aerothermal analysis of Dragon capsule at Mach 2-21, with altitude-specific heating profiles. Atlanta, Georgia, USA, 2008, pp. 1–8. URL: <https://repository.gatech.edu/bitstreams/39f02e86-13a2-4066-a79d-2a87df7d2ccd/download>.
- [96] P.A. Gnoffo. “CFD Validation Studies for Hypersonic Flow Prediction”. In: *Proceedings of the 39th Aerospace Sciences Conference*. Reno, NV, USA, 2001.
- [97] A. Finazzi et al. “Thermite-for-Demise Concept: from Material Selection to Test Campaign”. In: *ESA-TRP SPADEXO project* (2024). Preprint.
- [98] S. Dossi et al. “Enhancing micrometric aluminum re-activity by mechanical activation”. In: *Innovative Energetic Materials: Properties, Combustion Performance and Application*. Ed. by eds. Springer Nature, 2020, pp. 17–44. DOI: [https://doi.org/10.1007/978-3-030-36426-3\\_2](https://doi.org/10.1007/978-3-030-36426-3_2).
- [99] A. Finazzi et al. “Thermite-for-Demise (T4D): Experimental analysis of heat transfer principles and preliminary sizing of an application”. In: *International Journal of Heat and Mass Transfer* 220 (2024), p. 124957. DOI: <https://doi.org/10.1016/j.ijheatmasstransfer.2023.124957>.